#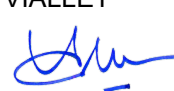 From a Regionalized Ground-Motion Model for Europe and Middle-East to Site-specific Seismic Hazard Assessments in Low-to-Moderate Seismicity Regions

WORK PACKAGE 3 - GROUND MOTION

AUTHORS		REVIEW		APPROVAL	
Name	Date	Name	Date	Name	Date
Sreeram Reddy Kotha	2019/11/15	John DOUGLAS Christophe MARTIN	2020/03/19 2020/04/16	Emmanuel VIALLET Public access ✓ SIGMA-2 restricted	2020/12/21 YYYY/MM/DD

Document history

DATE	VERSION	COMMENTS
2019/04/05	0	
2019/11/15	1	

Executive summary

Typical seismic hazard assessments focus on predicting the ground-motion exceedance probabilities at reference rock site conditions. Following which, soil response analyses are carried out to convolve the estimated hazard on reference rock into the actual hazard levels at a site accounting also its site-specific soil conditions. Although such simulation based site-specific hazard assessments have been in practice for several years, recent increase in site-specific ground-motion data has raised questions on its completeness. For instance, simulation based site-specific hazard assessment relies primarily on the 1D soil profile at a site, while ignoring the more complex 2D/3D topographic effects that may dominate the observed ground-motions at the site. Considering the computational expense (and epistemic uncertainties) of simulating realistic ground-motions accounting the various complexities, a feasible approach to site-specific hazard assessment seemed to be through collecting site-specific ground-motion data. With the site-specific ground-motion data, it is relatively straight-forward to estimate empirical site-specific adjustments for use in ground-motion prediction and thereby, seismic hazard assessment.

In regions of high seismicity, it is relatively convenient to collect site-specific ground-motion data from frequent tectonic events and develop site-specific ground-motion prediction models. The challenge however has been the development of such models in low-moderate seismicity regions, e.g. France, where the time required to collect sufficient site-specific data makes it impractical. To address this limitation, the idea of exporting site-specific ground-motion models developed in high seismicity regions to low-moderate seismicity regions has been pursued. However, the procedure proved to be more complex than anticipated due to the non-negligibly large regional differences in ground-motion observations. Therefore, a critical intermediate step has become the quantification of regional differences in observed ground-motions, prior to the quantification site-to-site differences within a region.

In this report, we discuss the progress towards site-specific ground-motion predictions in low-moderate seismicity regions. The analyses are performed on ground-motion observations reported as both response spectra and Fourier spectra. The process begins with developing new ground-motion prediction models for the high seismicity regions of Europe and Middle-Eastern regions. Given the tremendous differences in tectonics and geology across pan-Europe, it has become essential to quantify and evaluate the regional differences in the ground-motion. Quantification of regional differences is done via robust linear mixed-effects analyses of the ground-motion data. Evaluation involved asserting physical meaning to the quantified regional differences, and wherever possible, identifying new explanatory parameters capable of connecting high and low-moderate seismicity regions in terms of ground-motion characteristics. With this in hand, exporting region-specific ground-motion prediction models from high seismicity regions to low-moderate seismicity regions becomes conceivable. However, lack of suitable site-response proxies that can explain the observed site-to-site differences within a region has been impeding the process of exporting site-specific ground-motion prediction models to low-seismicity regions. In lieu of extensive site-response parametrization, we demonstrate

the procedure of estimating region- and site-specific adjustments to France, where fortunately a new ground-motion dataset has become recently available.

Based on the review of the scientific committee, this deliverable has been revised to be technically self-sufficient. All the comments from the review are considered, and the models presented here are revised accordingly. We note that some of the work cited in this document is in-preparation or submitted for peer-review. The work related to the regionalized ground-motion model (in Chapter 1) has benefitted substantially from the peer-review offered by the SERA consortium over the past one year.

S.R. KOTHA- From a Regionalized Ground-Motion Model for Europe and Middle-East to Site-specific
Seismic Hazard Assessments in Low-to-Moderate Seismicity Regions - SIGMA2-2019-D3-029/1

Chapter 1

A Regionalized Ground-Motion Model for Shallow Crustal Earthquakes in Europe and Middle-East

Introduction

Ground-Motion Models (GMMs) characterize the random distributions of ground-motions for a combination of earthquake source, wave travel-path, and the effected site's geological properties. Typically, GMMs are regressed over a compendium of strong ground-motion recordings collected from several earthquakes recorded at multiple sites scattered across a variety of geographical regions. The necessity of compiling such large datasets is to expand the range of magnitude, distance, and site-types; in order to regress a GMM capable of predicting realistic ground-motions for rare earthquake scenarios, e.g. large magnitudes at short distances from a reference rock site. NGA-West2 (Ancheta et al., 2014) is one such dataset compiled of ground-motion observations recorded around the globe – primarily from Western US, and in smaller fractions from Alaska, China, Italy, Japan, Taiwan, Turkey, etc. Several GMMs were derived from this dataset for various PSHA and risk applications. However, given the clear tectonic and geological diversity of the data, possible regional differences in observed ground-motions (Douglas, 2004) needed to be quantified. Four of the NGA-West2 GMMs (Abrahamson et al., 2014, Boore et al., 2014, Chiou and Youngs, 2014, Campbell and Bozorgnia, 2014) accounted for regional differences in ground-motions through region-specific regression coefficients. Through region-specific adjustments, these GMMs were able to capture and predict, for example, the faster attenuation of short-period ground-motions with distance in Japan compared to Western US, and the relatively slower attenuation in China. Earlier GMMs were not capable of such predictions simply from lack of sufficient data from individual regions to quantify the differences.

For Europe and Middle-East, RESORCE (Akkar et al., 2014b) is one such dataset compiled of data from Italy, Turkey, and other active seismic regions in pan-Europe. Using mixed-effects regression analyses (Abrahamson and Youngs, 1992, Bates et al., 2014), a few GMMs (Bindi et al., 2014, Akkar et al., 2014a) were derived and used in regional (Grünthal et al., 2018, Giardini et al., 2018) and continental (Woessner et al., 2015) Probabilistic Seismic Hazard Assessments (PSHA). However, these GMMs were not regionalized despite known geological differences between Italy and Turkey. In fact, even the regionalized GMMs (Kotha et al., 2016, Kuehn and Scherbaum, 2016, Kale et al., 2015, Bora et al., 2017) limited the distinction to geopolitical boundaries, while the geological diversity within these regions is far more complex. In essence, to quantify regional differences requires first, a regionalization scheme, and then, sufficient data from each region. With the arrival of the new European Strong-Motion (ESM) dataset (Lanzano et al., 2018, Bindi et al., 2018b) and regionalization models, and ongoing efforts to update the pan-European PSHA, a revision of the regionalized pan-European GMMs is proposed.

In the study, we present an upgrade of the RESORCE dataset based region-specific GMM for shallow crustal earthquakes (Kotha et al., 2016) using the ESM dataset. We often see GMMs evolve with progressively larger datasets, and supersede their older versions in terms of applicability (Bommer et al., 2010). However, with increasing data and complex parametrization, we have not achieved any reduction in the apparent aleatory variability (σ) of GMMs (Douglas, 2014).

Of course, increasing amount data implies increasing the spatio-temporal diversity of ground-motion observations, and thus an increasing σ. One approach would be to introduce new predictor variables into the GMM, but then, uncertainty or unavailability of predictor values is an issue (Kuehn and Abrahamson, 2017, Bindi et al., 2017). With this in mind, this revision of the Kotha et al. GMM (Kotha et al., 2016) will attempt to regionalize and refine the aleatory variability, while maintaining its original

1

1 parametrization. In addition, assuming a possible contamination of data and deviation from the
2 assumption of log-normality, instead of the usual ordinary least-square estimates of GMM median and
3 variances we compute their robust counterparts; while flagging outlier events, stations, and records in
4 the dataset. Table 1-1 summarizes the additional features we introduced in this new GMM (K19) with
5 respect to the recent pan-European GMMs: AK14 (Akkar et al., 2014a), B14 (Bindi et al., 2014), K16
6 (Kotha et al., 2016), L19 (Lanzano et al., 2019).

7 *Table 1-1: Comparison of features between the Europe and Middle East GMMs*

GMM feature	AK14	B14	K16	L19	K19
Event-to-event variability	■	■	■	■	■
Site-to-site variability			■	■	■
Depth-dependent attenuation				■	■
Regionalized anelastic attenuation			■		■
Event location-to-location variability					■
Measured V_{s30} based site-response	■	■	■	■	■
Topographic slope based site-response					■
Non-linear site-response	■				
Style-of-faulting terms	■	■		■	
Shear-wave radiation pattern					■
Median epistemic uncertainty				■	■
Heteroscedastic variances				■	■
Robust variance estimates					■
Outlier detection					■

Ground-Motion Data and Selection Criteria

9 Figure 1-1 compares the data distribution between RESORCE and ESM datasets. The increase in
10 amount of data between 2014 and 2018 for GMM development is dramatic. While the K16 GMM was
11 regressed over 1251 records, the proposed revision derives from 16344 records. One striking feature of
12 the ESM dataset is the number of stations with ≥ 3 ground-motion recordings. RESORCE dataset has
13 about 150 stations with ≥ 3 records, and ESM has 910. This increase is highly sought in empirical site-
14 specific GMM and PSHA applications (Kotha et al., 2017, Faccioli et al., 2015, Rodriguez-Marek et al.,
15 2013).

16 Another feature is the remarkable increase in the number of small earthquakes with $M_W \leq 4.5$.
17 This could imply an increase in σ of the revised GMM over K16, similar to the reported increase among
18 NGA-West2 GMMs with respect to their NGA-West counterparts. Nevertheless, ground-motions from
19 frequent small-moderate sized earthquakes drive the hazard in low-moderate seismicity regions of
20 Europe, such as France and Germany (Grünthal et al., 2018). Hence, it is necessary that the GMM is
21 well behaved in these small-moderate magnitude ranges. Moreover, if the site-specific terms $\delta S2S_s$ were
22 to be estimated with low uncertainty, data from several small-moderate sized earthquakes is
23 indispensable. The apparent decrease in data from moderate-large earthquakes $M_W \geq 5.5$ could be
24 from revision of M_W in ESM (Lanzano et al., 2018).

2

1   Finally, the distance (Joyner-Boore metric, R_{JB}) range and density of data is superior to
2   RESORCE. The region-specific anelastic attenuation terms of K16, NGA-West2 and other GMMs
3   (Sedaghati and Pezeshk, 2017) were estimated from records at $R_{JB} \geq 80km$. The revised GMM aims to
4   refine the regionalization of K16. In which case, such increase in data is quite welcome. In addition,
5   advanced studies on spatial and temporal variability of attenuation (Dawood and Rodriguez-Marek,
6   2013, Bindi et al., 2018a, Piña-Valdés et al., 2018, Kotha et al., 2019a, Landwehr et al., 2016, Sahakian
7   et al., 2019) are now possible.

8   The data visualized in Figure 1-1 is from shallow crustal earthquakes in the ESM dataset. The
9   full dataset contains ground-motions from other tectonic regimes as well, such as subduction interface,
10 subduction in-slab, Vrancea, etc. To filter out these and other records not suitable for a shallow crustal
11 GMM development, we modify and adopt the selection criteria suggested in the Bindi et al. (Bindi et al.,
12 2018b) preliminary sanity check:

13   1. Event depth (D) is the depth to top-of-rupture (z_{tor}), otherwise the hypocentral depth (D_{hypo}).
14   K16 selected only those events with hypocentral depth $\leq 35km$, which is a generic Moho depth
15   criteria to classify shallow crustal earthquakes at global scale (Garcia et al., 2012). However,
16   the Moho depth varies rapidly across active seismic regions of Europe and Middle East. To
17   keep only the shallow crustal earthquakes, we select only those events classified as non-
18   subduction events by Weatherill et al. (in-preparation), in their study towards selection of
19   appropriate subduction interface and inter-slab GMMs for the pan-European region. The
20   selection removes in-slab, interface, outer-rise, and upper-mantle events from the regression
21   dataset. The resulting 786 events with $0 < D \leq 35km$ are located in regions with $14 \leq$
22          $Moho\ depth \leq 49km$
23   2. Only those events with ≥ 3 records in the dataset, and with available EMEC M_W (Grünthal and
24   Wahlström, 2012) are used in regression
25   3. We keep all sites in the dataset irrespective of whether their V_{s30} measured from geotechnical
26   investigations is provided or not in ESM. This is to estimate δB_s at as many sites as possible,
27   and then examine possible site-response proxies to characterize the sites (Kotha et al., 2018,
28   Weatherill et al., 2019)
29   4. Choice of distance metric is R_{JB} where available, otherwise the epicentral distance R_{epi} – but
30   only for events with $M_W \leq 6.2$. The distance range is not truncated and extends up to $R_{JB} =$
31          $471km$
32   5. Sensor depth should be $< 10m$ and housing code ≠ "WEL" assuring the sensor is not in a
33   borehole, and installation code ≠ "BF" to remove those installed on building floors
34   6. Data from Iran had to be removed from regressions due to non-parametric evidence of triggering
35   at $1m/s^2$
36   7. Only those records with high-pass filter frequency $f_{hp} \leq 0.8/T$ for both horizontal components
37   are kept in the regression

38   Following the above criteria, the number of records available for GMM regression is 16344,
39 from 786 events ($3.1 \leq M_w \leq 7.4$) recorded at 1357 stations ($0 \leq R_{JB} < 471km$). These numbers
40 decrease to 8917, 451, and 1072 respectively with high-pass filter criteria (#7) at $T = 8s$.
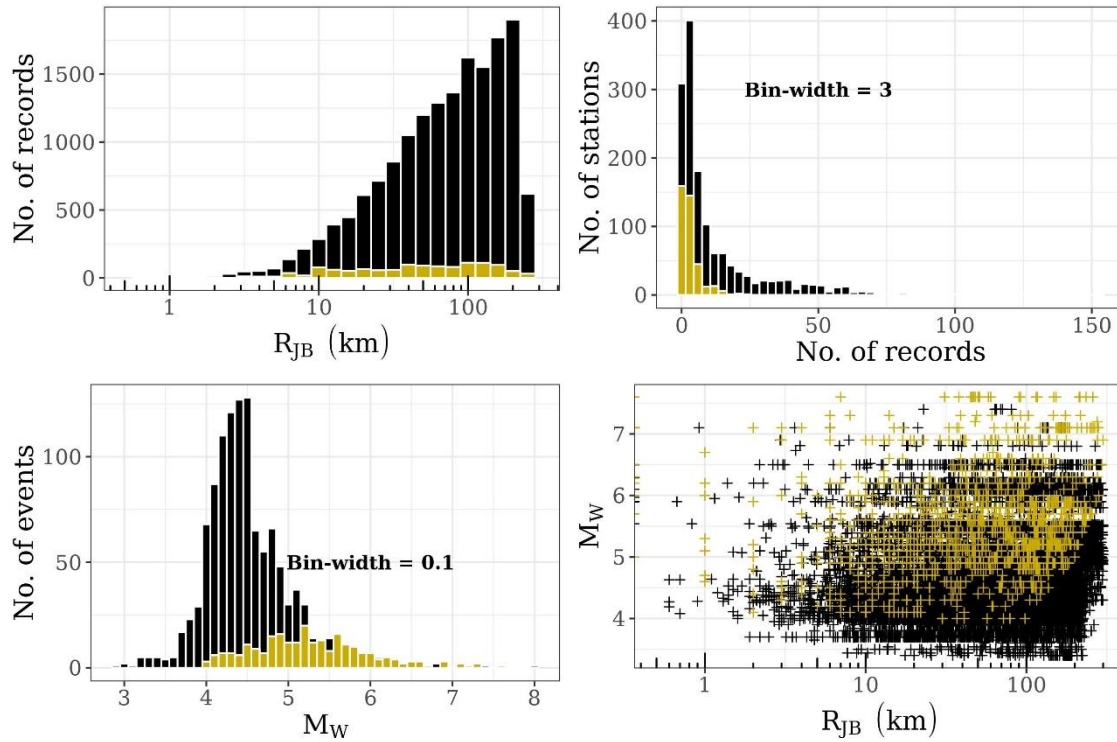
41

Figure 1-1: Data distribution comparing RESORCE (yellow) and ESM (black) datasets

Regionalization Datasets

In order to attempt GMM regionalization, we first need to define regions, classify the data into regions, and quantify the regional variabilities through regression. The mixed-effects regression estimates the *group* random-variances first, and then the random-effects for individual *levels* in the group (Bates et al., 2014). For instance, in estimating the well-known between-event term (δB_e), the preliminary step is to quantify observed event-to-event ground-motion variability as the between-event random-variance (τ^2). Following this, the between-event random-effects for each event are estimated from the total-residuals. Similar is the procedure for the between-site terms (δB_s), and other random-effects in a mixed-effects regression. Essentially, within the event group, individual events are the levels. It is important to note that, random-effect values for the levels (in a group) can be used: 1) in level-specific predictions with associated epistemic uncertainty, 2) investigated for any physical phenomena or 3) ignored – instead treating the group random-variance as an aleatory variability or epistemic uncertainty in a GMM logic-tree.

We emphasize that an *exploratory* analysis on random-effects (of levels in a group) is to evaluate if they make a physical sense or not. If yes, the random-effect group remains in the regression; otherwise the grouping needs revision. In this study, we aim to capture variabilities among events, event-locations (e.g. fault-zones), attenuation paths, and recording sites. Anticipating significant random-variances, we first describe the various regional datasets used to formulate the random-effect groups.

Attenuation regionalization

Recent GMMs have demonstrated a strong between-region variability of anelastic attenuation, which is partially attributed to spatial variability in crustal characteristics, e.g. the 1Hz Lg-coda Q values (Cong and Mitchell, 1998), shear-wave velocity (Lu et al., 2018), etc. The first generation of regionalized GMMs, however, relied on administrative boundaries for regionalization of anelastic attenuation (e.g. Italy, Turkey, Japan, California, etc.) – which could yield incongruous estimates of random-variances.

4

1 For example, attenuation characteristics within Italy, Turkey (Cong and Mitchell, 1998), France (Mayor
2 et al., 2018) are highly heterogeneous, which cannot be quantified with regionalization based on
3 administrative boundaries. Therefore, in this study, we adopt a more geological-geophysical
4 regionalization developed under the purview of the SERA project (Woessner et al., 2015) and modified
5 during this study .

6 Figure 1-2 shows the regionalization and the number of records within each region polygon, as decided
7 by the recording site location. Since the anelastic attenuation is a phenomenon dominant at far-source
8 distances and in near-surface crustal layers, we let the recording site location decide to which region a
9 particular record will be allotted. Alternatively, classing records based on event location would cause
10 some inconsistencies concerning event depth. Seismic waves from shallow and deep event sample
11 different depths of the crust (and upper mantle). SHARE tectonic regions (Woessner et al., 2015) and
12 the modified version used in this study, are surficial only, and cannot accommodate such depth
13 dependence of attenuation. Therefore, records are allotted to the regions based on the recording station
14 location.

15 There are 42 regions in this map (Figure 1-2), which is substantially larger than K16 with Italy, Turkey,
16 and rest of Europe as the three regions. This regionalization scheme splits Turkey into at least eight
17 regions, East and West Anatolia being the largest. Italy is highly fragmented as well. Figure 1-2 indicates
18 that there are regions with a few thousand records (e.g. Central and Northern Apennines), and a few
19 with less than a hundred records (e.g. Upper Rhine Graben). Thus, random-variance of the 'tectonic
20 regions' group will be a quantification of the observed region-to-region variability in anelastic attenuation
21 across these regions (the levels). Of course, a finer or coarser regionalization would yield a different
22 estimate of between-region variance. We note that, only if the random-variance for this group is
23 significant, it would mean the regionalization is appropriate and that there is a significant regional
24 variability in anelastic attenuation. Subsequently, we will need to evaluate whether the region-specific
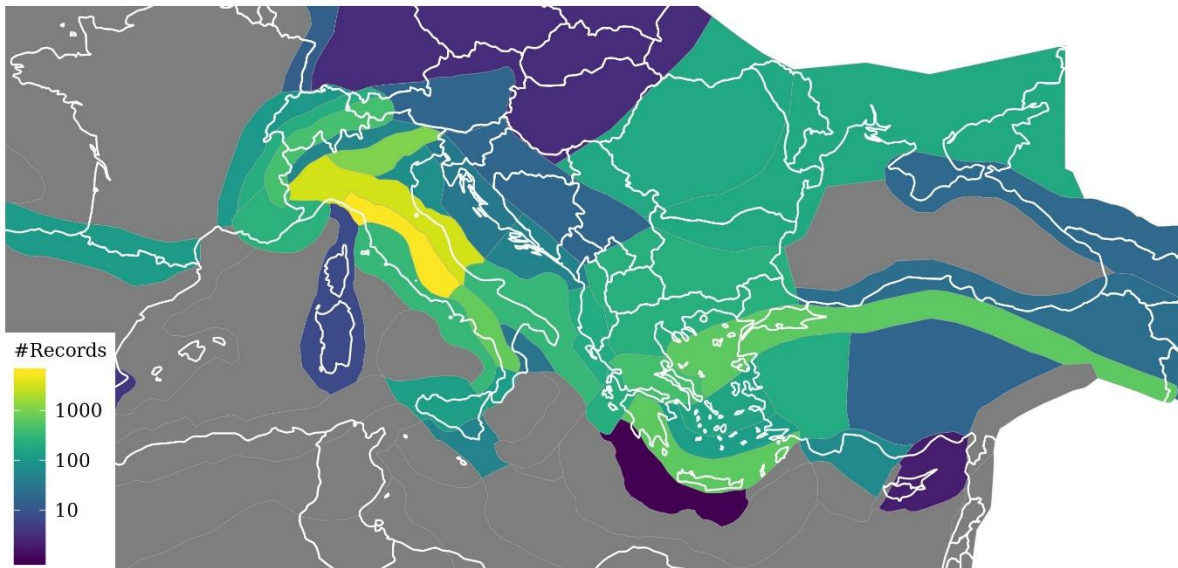25 random-effect values resemble any physical phenomenon.

Figure 1-2: Distribution of records in each of the attenuation regionalization polygons

26

Event regionalization

28 Traditionally, earthquake-to-earthquake variability is captured by the between-event random-variance
29 (τ^2), and the random-effect values (δB_e) are estimated for each event in this group. Based on earlier

1   works on fault-maturity (Manighetti et al., 2007, Radiguet et al., 2009, Bohnhoff et al., 2016), we
2   hypothesized that events associated to particular earthquake source (or a fault system) show
3   systematically stronger or weaker ground-motions, and that event-to-event ground-motion variability is
4   similar across various fault-systems.

5   In this study, we introduced an additional random-effect to quantify earthquake region-to-region
6   variability, similar to the location-to-location ($\delta L2L_l$) defined in (Al Atik et al., 2010), by allotting each
7   event to a documented fault-zone in the SERA area source model (ref). The random-effects group is
8   defined by area sources, but the group will be referred to as between-location ($\delta L2L_l$) for consistency,
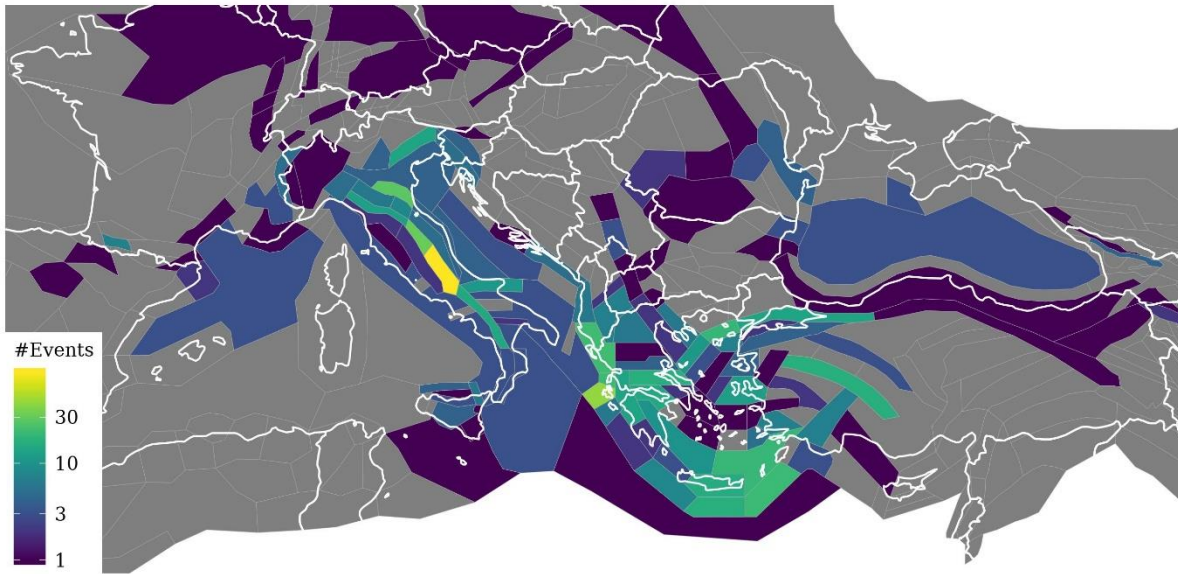9   wherein each level (location l) is an area source with associated shallow crustal events.

Figure 1-3: Number of shallow crustal events in each of the SERA area source polygons

10

11 Figure 1-3 shows the SERA area sources with at least one shallow crustal event associated to them.
12 Once again, this group is introduced to quantify the earthquake location-to-location variability of ground-
13 motion in the dataset through the between-fault variance (τ^2_{L2L}), which if close to zero indicates no
14 variability.

Functional Form

16 A mixed-effects GMM is composed of fixed-effects and random-effects. Fixed-effects part of the GMM
17 is the continuous function built as a combination of predictor variables, which in this case are event
18 magnitude M_W (ESM and EMEC values) and distance metric R_{JB} (in km). Various other finite distance
19 metrics (e.g. $R_{hypo}, R_{rup}, R_X, R_Y$) are provided in ESM, but only for a few $M_W \geq 5.5$ events with known
20 fault-geometry. While both (R_{hypo}, R_{rup}) can be approximated from (R_{epi}, R_{JB}) and D_{hypo} of point
21 sources, for finite-faults this approximation may lead to counter-intuitive GMM predictions. For instance,
22 in preliminary model iterations, ground-motion predictions for $M_W \geq 7.5$ events at $R_{rup} \leq 5km$ were
23 below those of $M_W = 6$. In a hazard perspective, this might imply lower hazard at shorter distances from
24 larger magnitude events. In this iteration of the GMM, we preferred to use R_{JB} (see criterion #4) to avoid
25 unexplainable GMM behavior. However, R_{JB} ignores the depth dependence of ground-motions entirely.
26 Following sections will illustrate how depth dependence, in complement with R_{JB}, is handled in our GMM.

27 The GMM is developed to predict the peak ground-motion measures: PGA (in gal) and PGV (cm/s), and
28 the 5% damped elastic response spectral ordinates in acceleration (SA, in gal) at 34 periods ranging

1 from 0.01 to 8s. Intensity measures (IMs) are provided for each record component (2 horizontal and 1
2 vertical) and in terms of orientation independent median values, RotD50 (Boore, 2010).

3 **Fixed-effects**

$$ln(\mu) = e_1 + f_{R,g}(M_W, R_{JB}) + f_{R,a}(R_{JB}) + f_M(M_W) + \delta L2L_l + \delta B_{e,l}^0 + \delta S2S_s + \varepsilon \tag{1}$$

$$f_{R,g} = (c_1 + c_2(M_W - M_{ref})) \ln \sqrt[2]{(R_{JB}^2 + h_D^2)/(R_{ref}^2 + h_D^2)} \tag{2}$$

$$f_{R,a} = \frac{c_{3,r}}{100} (\sqrt[2]{R_{JB}^2 + h_D^2} - \sqrt[2]{R_{ref}^2 + h_D^2}) \tag{3}$$

$$f_M = \begin{cases} b_1(M_W - M_h) + b_2(M_W - M_h)^2 & M_W \leq M_h \\ b_3(M_W - M_h) & M_h < M_W \end{cases} \tag{4}$$

4 The fixed-effects component of the GMM remains similar to that of K16 (eq. 1, 2, 3, 4), but with a few
5 minor changes based on non-parametric analyses. In Figure 1-4, the top row of plots show non-
6 parametric scaling of PGA with R_{JB}, where, for clarity, the data is split into magnitude bins and plotted
7 in separate panels. The bottom row of plots show non-parametric scaling of PGA with M_W, where again,
8 the data is split into distance bins and plotted in separate panels. The smooth (colored) curves are loess
9 fits (Jacoby, 2000) for the data illustrating scaling with magnitude and distance. However, given the
10 variety of hypocentral depths in the dataset, and that we are using the depth-insensitive R_{JB}, we
11 categorized the events into three depth bins ($D < 10km, 10km \leq D < 20km, 20km \leq D$), and plotted a
12 unique non-parametric attenuation curve for each bin. Based on such plots we introduced some changes
13 into the GMM with respect to K16:

14   1) In PGA vs R_{JB} panels, it is evident that deeper events ($20km \leq D$) have a longer near-source
15   saturation plateau – a feature controlled by the so-called h-parameter in GMMs. Shallower
16   events have a shorter near-source saturation plateau, and steeper decay with distance.
17   However, these differences are only prominent at $R_{JB} \leq 30km$
18   The marginally larger PGA values of $20km \leq D$ event at $R_{JB} > 30km$ are also reasonable
19   (Derras et al., 2012). Deeper events are closer to Moho, thereby producing weaker surface
20   ground-motions in the epicentral zone due to longer travel paths of direct arrivals, and relatively
21   stronger ground-motions at far-source distances due to the more efficiently propagating Moho
22   reflections, alongside the direct arrivals (Bindi et al., 2006).
23   Based on these observations, we allowed the h-parameter to vary with the depth bins, as
24   indicated by subscript in h_D^2 of eq. (2). In K16 GMM, this parameter was depth-independent, and
25   had no subscript. Instead of making this parameter a regression coefficient, we keep the
26   regression linear by assigning a priori values, independent of magnitude and period: $h_D = 12km$
27   for deeper $20km \leq D$ events, $h_D = 8km$ for events of intermediate depth $10km \leq D < 20km$,
28   and for shallow events with $D < 10km$ we assign $h_D = 4km$
29   2) In addition to the above, since ground-motions appear reasonably depth independent at $R_{JB} \geq$
30       $30km$ and vice-versa, we set $R_{ref} = 30km$ instead of 1km as in K16. M_{ref} in eq. (2) is the
31   reference magnitude, and remains the same as in K16 i.e., $M_{ref} = 4.5$
32   3) In PGA vs M_W panels, although the depth dependence of near-source attenuation is not evident,
33   we do observe saturation towards large magnitudes. In the panel showing non-parametric
34   ground-motion scaling with M_W, the evidence suggests that saturation begins at $M_W \geq 6.2$.
35   However, this is a feature most noticeable at $R_{JB} \leq 30km$ and at short periods (here, PGA).
36   Towards longer periods and longer distances, the saturation is less pronounced. Therefore,

1 unlike in K16 where the hinge-magnitude M_h was set at $M_W = 6.75$, in this GMM we set $M_h =$
2 6.2. M_h is period independent; saturation or otherwise beyond M_h is captured by b_3 in eq. (3).
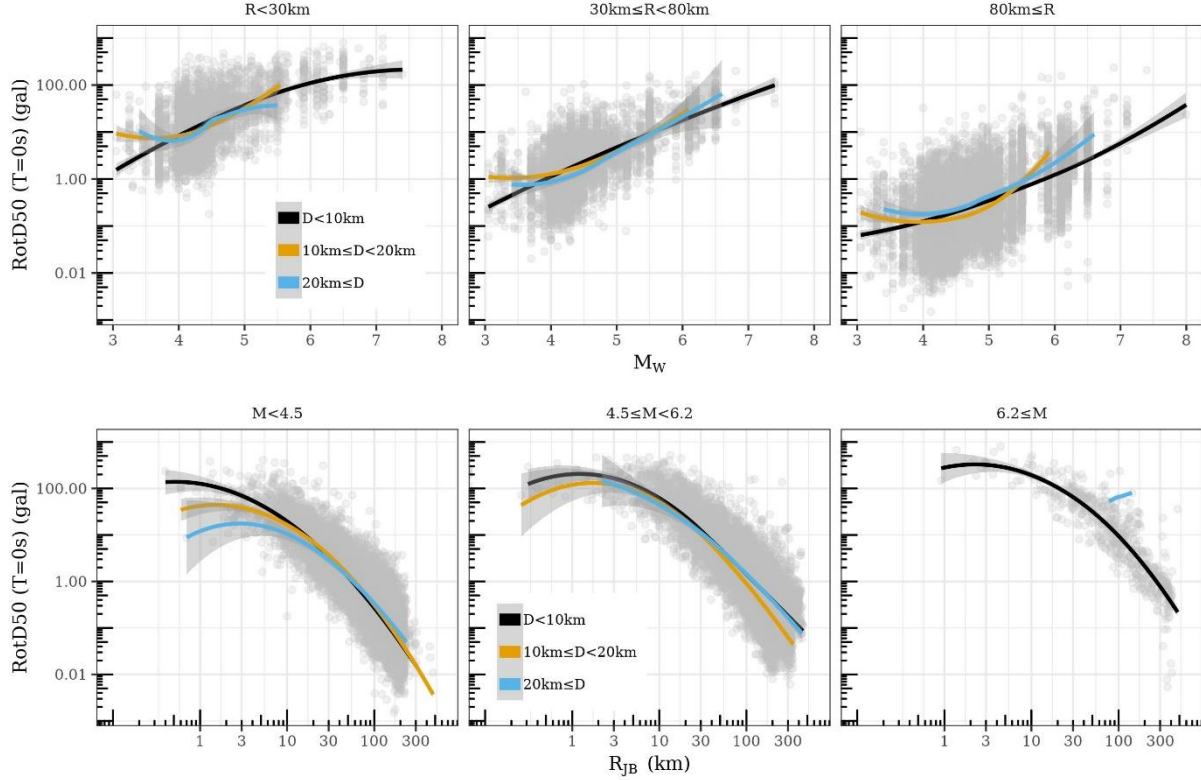

Figure 1-4: Non-parametric plots for PGA. (Top panels) PGA vs RJB, for various magnitude ranges. (Bottom panels) PGA vs magnitude for various distance ranges. The smoothed curves are the loess fits to the data, color-coded to distinguish scaling for events in three hypocentral depth bins.

3

Random-effects

4

5 In a mixed-effects formulation of equation (1), while f_R, f_M are the fixed-effects components, wherein the
6 regression coefficients $e_1, b_1, b_2, b_3, c_1, c_2, c_3$ are the fixed-effects regression coefficients (eq. 2 and 3):

7 1) τ_{c3} quantifies the between-region variability of anelastic attenuations across the attenuation
8   region group described earlier. This means, along with a (generic) region corrected c_3 and
9   random-variance τ_{c3}^2, region dependent adjustments $\delta c_{3,r}$ are estimated as random-effects.
10   These random-effects follow a Gaussian distribution $\Delta c_{3,r} = \mathbb{N}(0, \tau_{c3})$. $c_{3,r} = c_3 + \delta c_{3,r}$ is the
11   apparent anelastic attenuation term varying across regions (subscript r). In K16, r identified the
12   regions Italy, Turkey, and the rest of pan-European as Other. This grouping ensured that each
13   of the regions has sufficient data to estimate statistically significant $\delta c_{3,r}$. Accordingly, τ_{c3}^2
14   quantified the regional variability of anelastic attenuation when RESORCE dataset is grouped
15   into Italy, Turkey, and Other. ESM contains much more data from Italy and Turkey, and also
16   several other nations. Since the number of regions is ten-fold (37) that of K16 (three regions),
17   the quantified regional variability in anelastic attenuation, in terms of τ_{c3}, is also larger than that
18   of K16. Regions with sufficient data also benefit from a well-constrained region-specific
19   adjustment $\delta c_{3,r}$

20 2) Between-location variability of observed ground-motions are captured by the between-fault
21   random-effect $\Delta L2L = \mathbb{N}(0, \tau_{L2L})$, where the mixed-effects regression quantifies the variability
22   as τ_{L2L}, at each T, and earthquake location-specific terms as $\delta L2L_l$

3) Event-to-event variability, now filtered for between-location variability, is captured by the $\Delta B_{e,l}^0 = \mathbb{N}(0, \tau_0)$, where for an event e located in area source l, the event-specific term is $\delta B_{e,f}^0 = \delta B_e - \delta L2L_l$. τ_0 is the generic event-to-event variability corrected for location-to-location variability, and does not vary with location l.

4) Site-to-site variability is captured by the site-specific random-effects $\Delta S2S = \mathbb{N}(0, \Phi_{S2S})$. The potential of $\delta S2S_s$ in site-specific GMMs is well-known, and are useful in studying regional differences in site-response scaling with V_{s30} (time-averaged shear-wave velocity in 30m top-soil) as in K16 or other site-response proxies (Kotha et al., 2018, Weatherill et al., 2019)

In all, this GMM has four random-effect groups, i.e. one degree-of-freedom more than K16, to explain more than 10 times the data. Those common with K16 are refined with a more physical regionalization scheme, and greater geographical coverage of shallow crustal events and recording sites (with more than three records). With this configuration of mixed-effects GMM, we run a robust linear mixed-effects regression (Koller, 2016) independently for the 36 RotD50 IMs of 5% damped SA for $T = 0.01 - 8s$, PGA and PGV. Along with the regression coefficients, we estimate and provide also the fixed-effects variance-covariance matrices needed to estimate the GMM epistemic uncertainty (Atik and Youngs, 2014, Bindi et al., 2017) and to update the GMM coefficients in a Bayesian framework.

Regression Method

Unlike K16, where the GMM is regressed using an ordinary least-squares mixed-effects regression algorithm (Bates et al., 2014), in this study we employ a robust mixed-effects regression algorithm (Koller, 2016). As any other real-life data, ground-motion data may contain outliers and other contaminations. Even minor contamination may drive the classical ordinary least-square mixed-effect estimates away from those without contamination. Robust linear mixed-effects (rlmm) regression is quite useful in limiting the influence of outlier events, sites, and records, and to flag them for examination.

A feature of rlmm relevant to this study is that the random-effects (events, fault-zones, attenuation regions, sites) and residuals (records) with values beyond ±1.345 standard deviations of their respective normal random-distribution are assigned progressively lower weights (< 1); whereas, in ordinary least-squares all data is assigned unit weight. Any event, site, and record with non-unit weight are considered a possible outlier, and needs to be examined for its peculiarity.

Results and Discussion

The regression results comprise of fixed-effect coefficients and covariance matrices, random-effect values, weights and standard errors, residuals, and variances. It is customary to check the behavior of GMM fixed-effects component, and its epistemic uncertainty in various magnitude and distance ranges. Random-effects and residuals are checked for any noticeable biases or trends with predictor variables. We discuss them separately.

Fixed-effects

Figure 1-5 shows the GMM's median $SA(T = 0s)$, which is PGA (in gal), predictions over magnitude and distance ranges. Along with the median prediction (lines), the epistemic uncertainty, in terms of asymptotic standard deviation (σ_μ), is shown as well (ribbons).

First, we discuss the predicted PGA scaling with R_{JB} in the left panel of Figure 1-5. In this plot, we show 27 combinations:

    i. [M4, M5.5, M7] illustrating distance-scaling for $M_W = 4, 5.5, 7$

    ii. [Shallow, Intermediate, Deep] to illustrate the function of $h_D = 4, 8, 12 km$ for events with depth $D < 10km, 10km \leq D < 20km, 20km \leq D$, respectively

9

1   iii.   [Average, Faster, Slower] attenuating regions to illustrate the effect of $c_{3,r} = c_3 + \delta c_{3,r}$, with
2             $\delta c_{3,r} = 0, -\tau_{c3}, +\tau_{c3}$, respectively

3 Looking at the curves for M4, we notice the impact of depth-dependent h_D in rendering a shorter (plateau
4 ~ 0 - 2km) near-source saturation for shallower events, compared to the intermediate depth events
5 (plateau ~ 0 - 3km) and deeper events (plateau ~ 0 - 4km). The three curves merge at about 30km,
6 which is our R_{ref}. Beyond $R_{ref} = 30km$, the depth-dependence of distance scaling is non-existent. The
7 predictions show good agreement with the non-parametric trends in Figure 1-4.

8 Beyond the R_{ref}, we see the region-dependent anelastic adjustments coming into play. We show the
9 impact of adjusting c_3 with $\delta_{c3} = 0, -\tau_{c3}, +\tau_{c3}$. A region with faster than average attenuation will have a
10 c_3 more negative than generic average ($\delta_{c3} = -\tau_{c3}$), and vice-versa for slower attenuation ($\delta_{c3} = +\tau_{c3}$).
11 Which of the 37 regions in pan-Europe apparently attenuate faster or slower than pan-European average
12 ($\delta_{c3} = 0$) will be discussed in later sections. Effect of δ_{c3} at $R_{ref} < 30km$ is negligible, as it should be.
13 Therefore, the 27 curves appear as three on either side of $R_{ref} = 30km$, simply because near-source
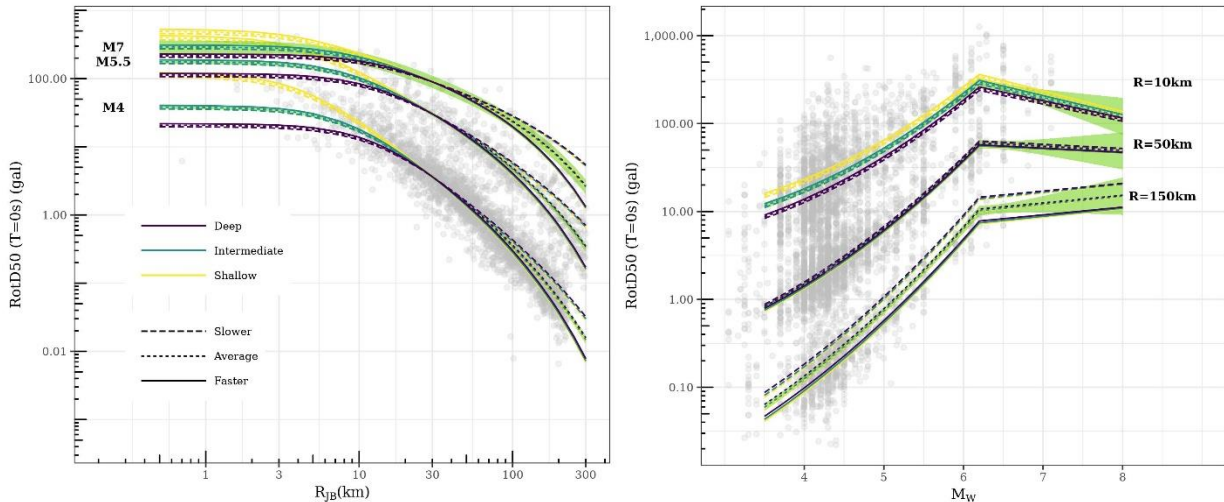14 (h_D) and far-source (δ_{c3}) adjustments have their exclusive domains of influence.

Figure 1-5: GMM median predictions of PGA. The left panel shows predicted scaling of PGA with distance, for shallow ($D < 10km$), intermediate ($10km \leq D < 20km$), and deep ($20km \leq D$) events in regions with average, slower and faster than average anelastic decay at long distances. The right panel shows scaling of PGA with magnitude for the same combinations. In both panels, the epistemic uncertainty on GMM median is shown by the green ribbon around prediction for intermediate depth events in averagely attenuating regions. Also shown are ground-motion observations corrected for between-fault, between-event and between-site random-effects as grey markers

15
16 In Figure 1-5, we also show the epistemic uncertainty on median predictions. The green ribbon is almost
17 too thin to be noticeable for M4 and M5.5 predictions. Only for M7 events, the ribbon is visibly wide
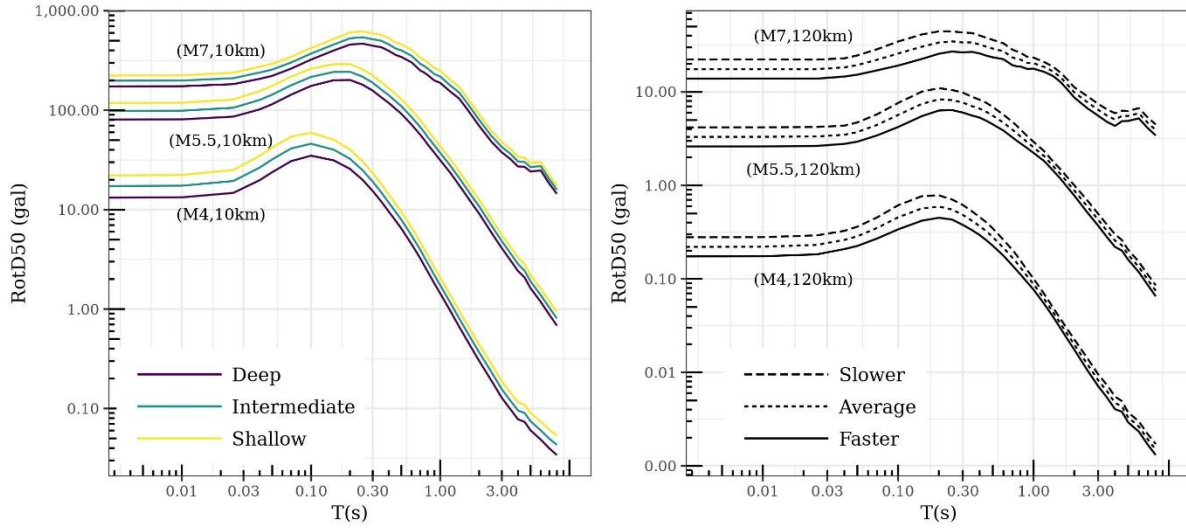18 because of the very limited data from large magnitude events in the ESM dataset.

10

Figure 1-6: Predicted Response spectra of the GMM for various scenarios, differentiated by color for shallow ($D < 10km$), intermediate ($10km \leq D < 20km$), and deep ($20km \leq D$) events in the left panel. In the right panel are the response spectra differentiated by regional anelastic attenuation (Slower, average, faster)

In the right panel of Figure 1-5, we show the PGA scaling with M_W. Here as well we show 27 curves, but this time for $R_{JB} = 10, 50, 150km$ instead of the three M_W values. The features in scaling with distance discussed in reference to the left-panel also prevail here; δ_{c3} is effective at $R_{JB} = 150km$, while h_D is effective at $R_{JB} = 5km$ and neither are at $R_{JB} = 50km$. More important in this context, is the difference in scaling with magnitude at $R_{JB} = 10km$ compared to $R_{JB} = 50, 150km$. Evidently, the scaling is more gradual (less steep) at near-source distance for $M_W < M_h$ and oversaturates for $M_W \geq M_h$. This is a known physical behavior wherein, near-source ground-motions, especially the short period SAs, are less sensitive to M_W (Campbell, 1981, Schmedes and Archuleta, 2008). Several previous GMMs observed the same with various datasets. Boore et al. (Boore et al., 2014) and K16 allowed oversaturation at large magnitudes ($M_W \geq 6.75$), but whether this is realistic or not needs to be verified with specially compiled near-source ground-motion datasets (Pacor et al., 2018).

Random-effects and Residuals

Figure 1-7 shows the random-effect and residual standard deviations of the GMM. The total ergodic standard deviation of the GMM is $\sigma = \sqrt{\tau_{L2L}^2 + \tau_0^2 + \phi_{S2S}^2 + \phi^2}$, when considering all source and site variabilities as aleatoric. The solid lines in this plot correspond to the variance estimates of the GMM from ESM dataset (this study), while the dashed lines indicate those of the K16 GMM from RESORCE dataset. Note that the K16 GMM does not group events into area sources, and thus between-location variability component τ_{L2L} is absent.

Research and Development Program on
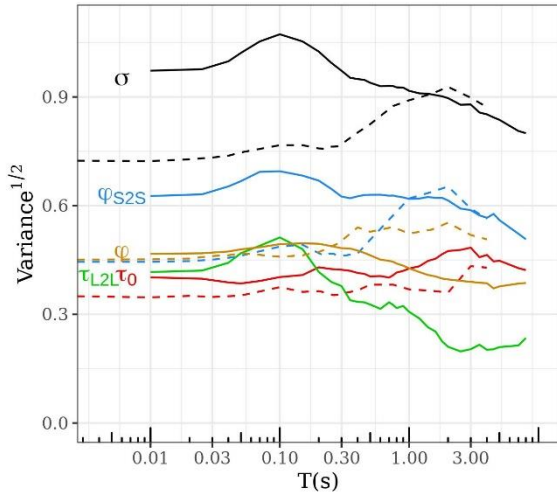Seismic Ground Motion

Figure 1-7: Residual and random-effect variance estimates of the GMM for $T = 0.01 - 8s$ (solid lines). The colors identify the various random-effect and residual components. For comparison, variance estimates for the K16 GMM from RESORCE dataset (Kotha et al. 2016) are overlain in dashed lines.

1

2   We show that the total standard deviation σ of the new GMM is considerably larger than that of K16
3   GMM. The largest increase in σ (at short-moderate periods) is from the increase in between-site
4   variability ϕ_{S2S}, possibly with the increase in number of stations from 384 in RESORCE to 1357 in ESM.
5   A notable increase in between-event variability can be seen, which can be attributed to the increased
6   regional diversity of earthquakes, the increase of number of $4 < M_W \leq 5.5$ events from 164 in RESORCE
7   to 676 in ESM, and an additional 70 events with $M_W < 4$ in ESM. The residual variability ϕ of the new
8   GMM, however, is equal or smaller than that of K16, despite the increase in regional diversity, the
9   sample size, and the recording distance range from 300km to 471km. In our view, this plot emphasizes
10 the need to move from ergodic to (partially non-ergodic) site-specific ground-motion predictions
11 (Anderson and Brune, 1999, Rodriguez-Marek et al., 2013, Kotha et al., 2017).

12 *Anelastic attenuation variability*

13 Figure 1-8 shows the region-specific $\delta c_{3,r}$ adjustments (colored lines and ribbons) of the 42 regions
14 for $T = 0.01 - 8s$. Most of these curves lie within the $\pm\tau_{c3}$ (red lines) bounds. As indicated by τ_{c3}, the
15 region-to-region variability of apparent anelastic attenuation is the highest at short periods, and
16 decreases gradually towards longer periods. High-frequency ground-motions are more susceptible to
17 strong anelastic decay in the crust, which could be related to the crustal properties. Long period SAs
18 are not effected as much by anelastic attenuation, therefore regional differences are relatively smaller
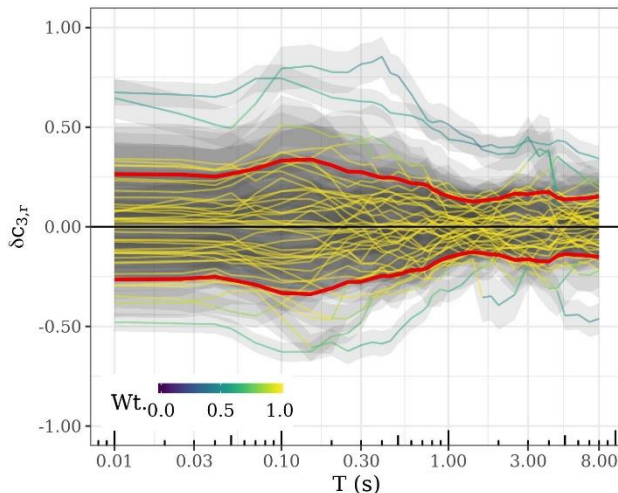19 i.e., τ_{c3} is smaller at $T \geq 1s$.

Figure 1-8: $\delta c_{3,r}$ for $T = 0.01 - 8s$. Each line corresponds to one of the 37 attenuation regions, with colors indicating their weight in robust regression. Overlain red curves mark the $\pm\tau_{c3}$ values. Regions with $\delta c_{3,r}(T)$ beyond $\pm 1.345\tau_{c3}(T)$ are given a lower than a unit weight

20

1 In RESORCE dataset, K16 observed that short period SAs attenuate faster in Italy than in Turkey, which
2 was observed earlier in NGA-West2 dataset by (Boore et al., 2014), and confirmed later in Fourier
3 domain (Bora et al., 2017). However, these observations were based on distinguishing regions by
4 administrative boundaries and not geological or geophysical features. Since τ_{c3} estimated for the new
5 regionalization is not zero, we can assert that regional variability of anelastic attenuation exists. Of
6 course, regions with fewer data have larger epistemic uncertainty (standard error) on their $\delta c_{3,r}$, but the
7 largest epistemic uncertainty is always lower than the aleatoric τ_{c3}, and decreases with increasing data.

8 *Source variability*

9 Earthquake source variability is split in two random-effect groups: between-event $\Delta B_{e,l}^0 = \mathcal{N}(0, \tau_0)$ and
10 between-location $\Delta L2L = \mathcal{N}(0, \tau_{L2L})$. Between-event terms can be estimated for the recorded
11 earthquakes, but are difficult to predict for prospective earthquakes because of their spatiotemporal
12 variability. Even when correlated with stress-drop or a source parameter that can explain the relative
13 differences in ground-motions, prediction of stress-drop for the next event is yet not possible.
14 Traditionally therefore, between-event variability is considered purely aleatoric. Between-location
15 random-effect is intended to quantify a portion of the between-event spatial variability into the SERA
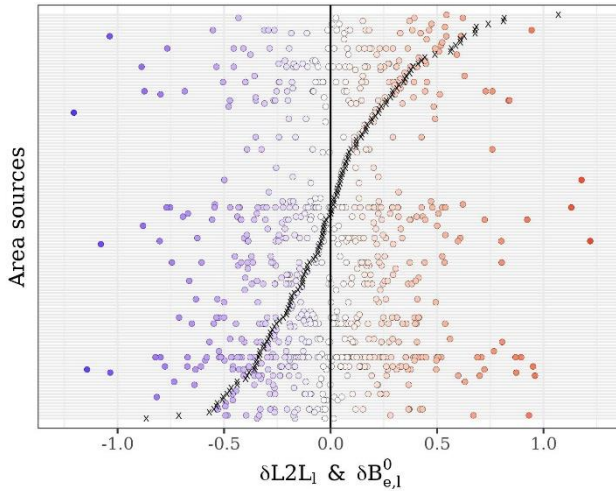16 area sources.

Figure 1-9: $\delta L2L_l$ & $\delta B_{e,l}^0$ random distributions for PGA. The black markers indicate the $\delta L2L_l$ of each area source, while the colored markers indicate the $\delta B_{e,l}^0$ of the events within each source.

17

18 Figure 1-9 shows the normal random-distribution $\Delta L2L = \mathcal{N}(0, \tau_{L2L})$, and the distribution of $\delta B_{e,l}^0$ within
19 each area source l. Since each event is exclusive to its area source, the between-event group is nested
20 in between-location group. As a result, $\delta L2L_l$ values are approximately the mean of between-event
21 variability δB_e within each area source l, and the $\delta B_{e,l}^0$ distributions are centered close to zero. $\delta L2L_l$
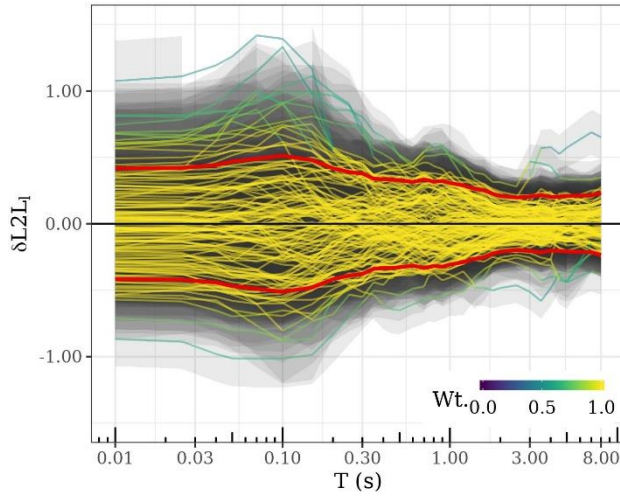22 values serve as the predictable part of event-to-event spatial variability.

13

Figure 1-10: $\delta L2L_l$ for $T = 0.01 - 8s$. Each line corresponds to one of the 133 area sources, with colors indicating their weight in robust regression. Overlain red curves mark the $\pm\tau_{L2L}$ values. Area sources with $\delta L2L_l(T)$ beyond $\pm 1.345\tau_{L2L}(T)$ are given a lower weight than one

Figure 1-10 shows the $\delta L2L_l(T = 0.01 - 8s)$ for 133 area sources. As always, the standard error (or epistemic uncertainty) of $\delta L2L_l$ values is smaller than the τ_{L2L}. τ_{L2L} values are non-negligible, and the GMM fit improves with introduction of between-location random-effect group. Therefore, we consider it an efficient random-effect. Although it is tempting to relate $\delta L2L_l$ to some source parameter, it is better done in the Fourier domain.

Between-event variability, now partially corrected for spatial variability through $\Delta L2L = \mathbb{N}(0, \tau_{L2L})$, is quantified in the distribution $\Delta B_e^0 = \mathbb{N}(0, \tau_0)$. Customary checks for $\delta B_{e,l}^0$ include dependencies on magnitude, depth, and style-of-faulting (SoF). A few points to note here:

1) EMEC estimates of M_W are used in the GMM regression. However, uncertainties in M_W are ignored despite their impact on the τ estimates (Kuehn and Abrahamson, 2017)
2) Depth in our case is hypocentral depth of the event, wherever the depth to top-of-rupture is not available. Buried ruptures are likely to produce stronger ground-motions than the exposed ruptures. This phenomenon is introduced in some of the NGA-West2 GMMs e.g., Abrahamson et al. (Abrahamson et al., 2014) modelled the events with $z_{tor} \geq 20km$ to have 0.75 - 3 times larger SAs, depending on the period, than exposed ruptures.
3) Centroid Moment Tensor (CMT) solutions are available for too few events to treat style-of-faulting in a sophisticated manner as in Kotha et al. (Kotha et al., 2019a). Even if available, the diversity of crustal structure across pan-Europe makes it difficult, without substantially more metadata (e.g. take-off angles) in the ESM dataset. In this study, we use the typical style-of-faulting classification provided in the ESM dataset: Normal (NF), Thrust (TF), Strike-slip (SS), and Unknown (U). However, instead of introducing a SoF random-effect in the GMM regression, we queried the ΔB_e^0 and $\Delta L2L$ distributions and found no systematic differences.
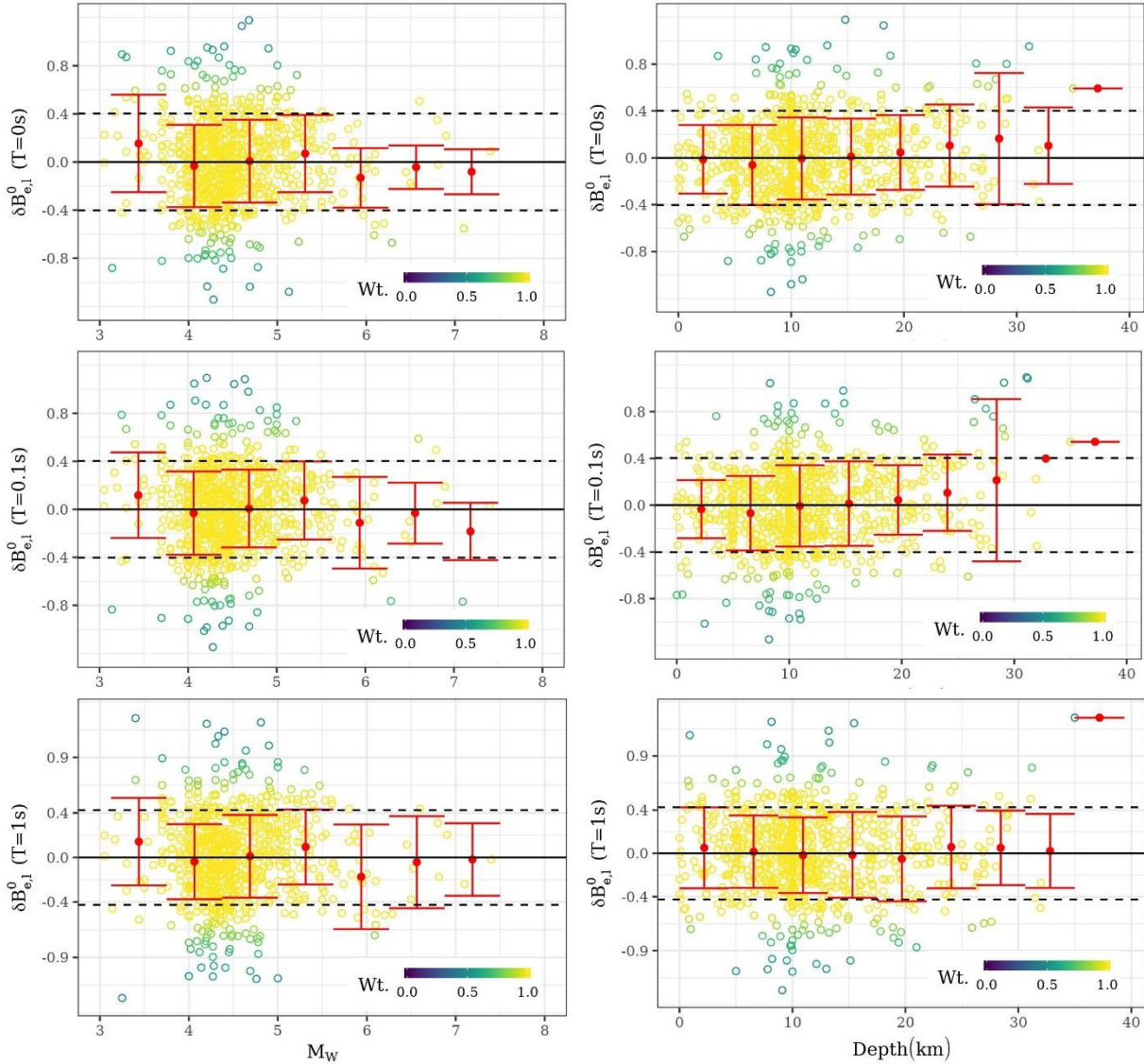
Figure 1-11: $\delta B_{e,l}^0$ versus M_W (left column) and depth (right column) for three periods $T = 0s, 0.1s, 1s$. The mean (red line) and median absolute deviance (red ribbon) of $\delta B_{e,l}^0$ within the bins of size $0.5 M_W$ and $5 km$. The two horizontal lines mark the $\pm \tau_0$ for the three periods change notation

1

2 The left column of Figure 1-11 shows $\delta B_{e,l}^0$ ($T = 0s, 0.1s, 1s$) trends with M_W. No significant offsets or
3 trends imply the magnitude scaling of the GMM sufficiently captures the magnitude dependence of SAs.
4 The error bars show the median absolute deviance (MAD) of $\delta B_{e,l}^0$ within bins of size $M_W = 0.5$. MAD is
5 a robust estimate of variance when normality of distribution is not satisfied within each bin. The MAD
6 estimates appear to be magnitude dependent, indicating heteroscedasticity of τ_0. However, now we do
7 not provide a heteroscedastic variance model without investigating first its significance, given the small
8 number of large magnitude events compared to small-moderate magnitude event sample (see Figure
9 1-1 for data distribution).

10 The right column of Figure 1-11 shows $\delta B_{e,l}^0$ ($T = 0.01s, 0.1s, 1s$) trends with depth. We see no significant
11 trend with depth except at $D \geq 20 km$ (Abrahamson et al., 2014), where an upward trend is apparent.
12 Deeper events appear to produce stronger ground-motions. Most of these events are from Greece and
13 Turkey, which we have discussed in the context of $\delta L2L_l$ as those being closing to the Moho, recorded

15

1   at predominantly at far-sources distances, and possibly, sub-crustal events with high stress-drop.
2   Although the trends are physically meaningful, we chose not to consider them until a more event-specific
3   investigation. Moreover, there are shallower events with similarly large $\delta B_{e,l}^0$, and correcting $\delta B_{e,l}^0$ for
4   depth shows no remarkable reduction in τ_0 – as indicated by the bin-wise τ_0 values (error bars in Figure
5   1-11)

6   *Site-response variability*

7   As in K16 GMM and KiK-net GMM (Kotha et al., 2018), we did not introduce a site-response scaling
8   parameter in the fixed-effects for two reasons: 1) Only 272 of the 1357 sites have measured V_{s30}
9   available in the ESM. Using data from only the sites with measured V_{s30} leads to a large reduction in
10   data for regression, 2) investigation of site-to-site variability can be performed in a subsequent step. For
11   instance, depending on the application, one can regress a relation between $\delta S2S_s \sim V_{s30}$ measured or
12   inferred from topographic slope and geology (Wald and Allen, 2007, Vilanova et al., 2018, Thompson et
13   al., 2014) or relate $\delta S2S_s$ directly to topographic slope and geology (Weatherill et al., 2019, Crowley et
14   al., 2019 - in-preparation, Kotha et al., 2019b).

15   Given the importance of site-response in hazard and risk assessments, the complexities in finding a
16   compromise between a site-response proxy, its availability at different regional scales, and the
17   propagation of uncertainties from GMMs to risk assessments, we intend to perform a separate
18   investigation, not presented here. Nevertheless, a database of $\delta S2S_s(T = 0.01 - 8s)$ for the 1357 ESM
19   sites along with the rlmm weights and standard errors is provided.

20   Early analyses of $\delta S2S_s(T = 0.0, 0.1, 1.0s)$ trends with V_{s30} and topographic slope are presented in
21   Figure 1-12. The left column of Figure 1-12 plots the mean and MAD (robust standard-deviation
22   estimate) of $\delta S2S_s(T = 0.0, 0.1, 1.0s)$ within ranges of V_{s30} (coinciding with Eurocode8 site classes A, B,
23   C, and D) and *slope* (9 bins of equal width between 0.001m/m and 1.000m/m). Trend with V_{s30} inferred
24   from a $V_{s30} \sim slope$ correlation model (Wald and Allen, 2007) is comparable to the trend with slope (from
25   which it is inferred) in the right column.

26   The correlation $\delta S2S_s \sim V_{s30}$ at short-periods $T = 0.0, 0.1s$ is rather poor, as indicated by similar mean
27   and MAD for $V_{s30} < 800m/s$ in the left column of Figure 1-12. It appears that short-period site-responses
28   of soft and still soils (EC8 class B, C, D) in this dataset are not adequately distinguishable. However, it
29   is interesting to see that the mean of EC8 class A 'rock' sites with $V_{s30} \geq 800m/s$ is much lower than the
30   rest, along with a considerably larger variability. Short-period linear soil-response of rock sites is known
31   to be highly variable compared to softer soils, whose non-linear soil-response may suppress the higher
32   variability from linear-only amplification. On the contrary, the long-period site-response of rock sites is
33   less variable than that of softer soils (e.g. $180m/s \leq V_{s30} < 800m/s$). Similar inferences can be drawn
34   from the $\delta S2S_s \sim slope$ plots in the right column of Figure 1-12, where higher slopes are (usually)
35   indicative of rock sites on steep hillsides, and lower slopes at softer sites located on flatter sediments.
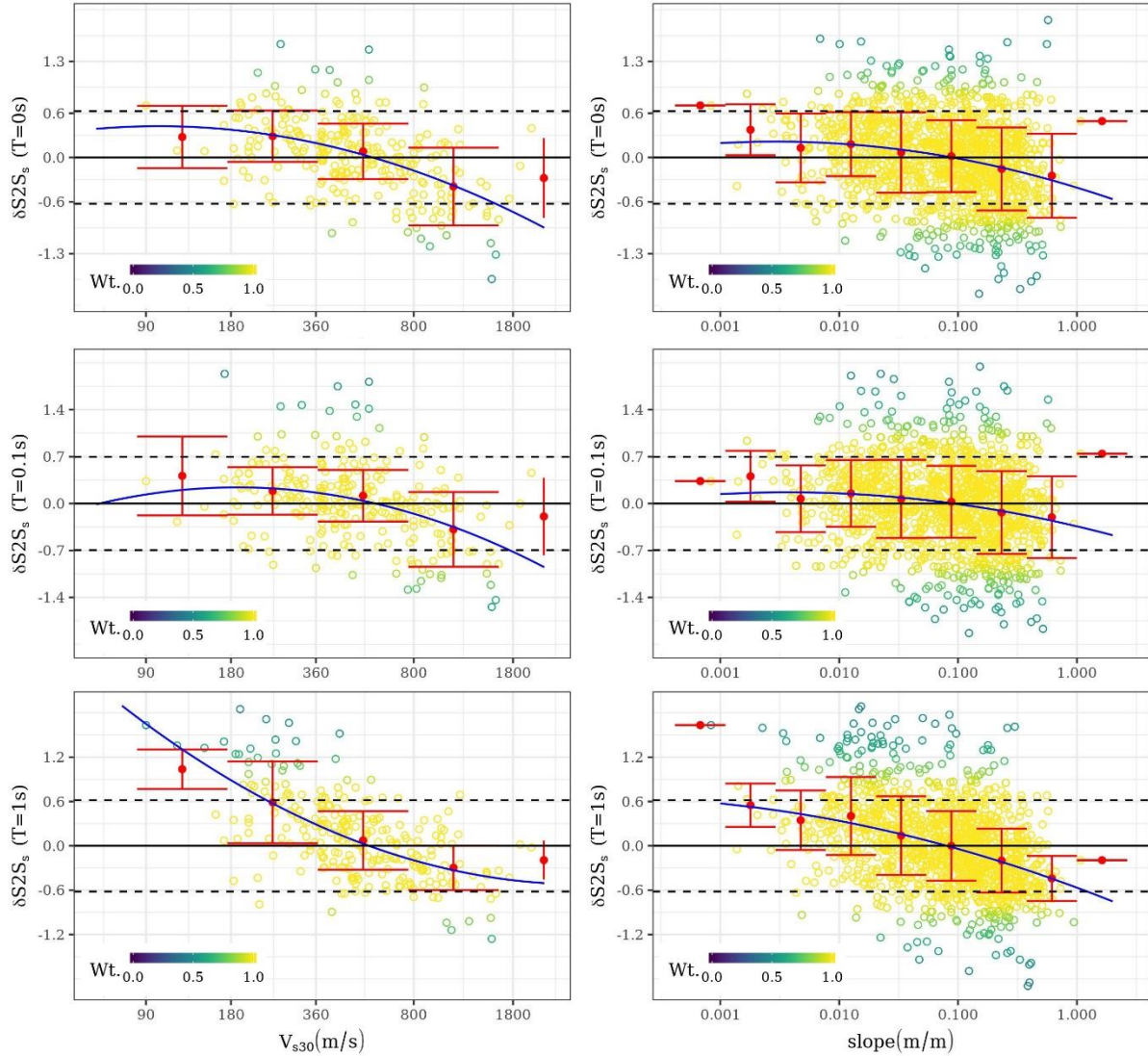
Figure 1-12: Plot showing the trend of $\delta S2S_s(T = 0, 0.1, 1s)$ (from top to bottom rows) with V_{s30} (left column) and topographic slope at site location (right column). Note that only 272 sites have measured V_{s30}, compared to 1357 sites with slope. At short-moderate periods (T = 0, 0.1s), the loess fit shows as poor non-paramtric trend, which improves at longer periods (T = 1s).

1

2 For completeness, along with a database of $\delta S2S_s(T = 0.0 - 8.0s)$ for the 1000+ ESM sites, we derive
3 a continuous empirical models for both $\delta S2S_s \sim V_{s30}$ and $\delta S2S_s \sim slope$ correlations. We chose a
4 quadratic functional form instead of the traditional piecewise linear function, shown in equations (5) and
5 (6). Where, V_{s30} is in m/s and $slope$ in m/m, the regression coefficients g_0, g_1, g_2 and robust standard
6 deviations $\phi_{S2S}^{V_{s30}}$ (of $\Delta S2S^{V_{s30}}$ residuals) of and ϕ_{S2S}^{slope} (of $\Delta S2S_s$ residuals) are different for $\delta B_s \sim V_{s30}$
7 and $\delta B_s \sim slope$ empirical models.

$$\delta S2S_s = g_0 + g_1 * \ln\left(\frac{V_{s30}}{800}\right) + g_2 * \left(\ln\left(\frac{V_{s30}}{800}\right)\right)^2 + \delta S2S_s^{V_{s30}} \qquad (5)$$

$$\delta S2S_s = g_0 + g_1 * \ln\left(\frac{slope}{0.1}\right) + g_2 * \left(\ln\left(\frac{slope}{0.1}\right)\right)^2 + \delta S2S_s^{slope} \qquad (6)$$

8 Robust linear fits using an M estimator (Venables and Ripley, 2002), at each of 34 periods between $T =$
9 $0.01s - 8s$, PGA $(T = 0s)$ and PGV, are derived for $\delta S2S_s \sim V_{s30}$ correlation of 272 sites with V_{s30}

17

1 available, and $\delta S2S_s \sim slope$ for the 1357 sites with $slope$ derived from digital elevation models. The site-
2 specific weights used in the robust regression of equation (5) and (6) are those obtained from the prior
3 robust linear mixed-effects regression of the GMM. The blue curves in Figure 1-12 represent the
4 regression fits of equation (5) and (6).

5 Although heteroscedastic models of $\phi_{S2S}^{V_{s30}}$ and ϕ_{S2S}^{slope} appear reasonable from Figure 1-12, we chose not
6 to propose one without testing its significance, given the uneven distribution of sites in different bins.
7 Figure 1-13 shows the reduction in between-site variance from using V_{s30} and $slope$ as site-response
8 proxies (equation 5 and 6) in the GMM. For comparison, the variances of K16 GMM are also shown in
9 this plot. Note that the K16 GMM comes in two variants: one without a site-response component, and
10 another with V_{s30} as a proxy for linear site-response. The K16 variances shown in Figure 1-7 are those
11 when not using V_{s30} as a parameter, while those in Figure 1-13 are when using V_{s30} as site-response
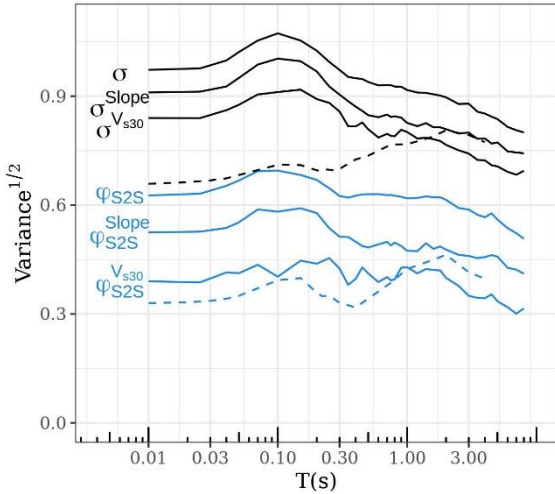12 proxy – hence, lower.

Figure 1-13: Between-site and total variance estimates (ϕ_{S2S}, σ) of the GMM for T = 0.01-8s (solid lines) compared with those of K16 GMM from RESORCE DATASET (dashed lines). Reduction of (ϕ_{S2S}, σ) to $(\phi_{S2S}^{V_{s30}}, \sigma^{V_{s30}})$ using V_{s30}, and to $(\phi_{S2S}^{slope}, \sigma^{slope})$ using Slope as site-response proxies. Note that the (ϕ_{S2S}, σ) of K16 GMM are those using V_{s30} as site-response proxy, and are smaller than those shown in Figure 1-7, which are from the K16 GMM version without a site-response parameter

13

14 A significant reduction in between-site standard deviation can be achieved using an efficient site-
15 response proxy or a combination of multiple proxies. Since only a few sites are provided with measured
16 V_{s30} values, $\phi_{S2S}^{V_{s30}}$ is substantially smaller than ϕ_{S2S}^{slope}. For a new site with V_{s30} or $slope$ available, equation
17 (5) or (6) can be appended, respectively, to the GMM in equation (1) while replacing the $\delta S2S_s$ term. For
18 site with neither site-response proxy available, but with sufficient strong ground-motion recordings, the
19 site-specific $\delta S2S_s$ term can be estimated and used for site-specific ground-motion predictions
20 (Rodriguez-Marek et al., 2013, Faccioli et al., 2015, Kotha et al., 2017).

21 *Aleatoric variability*

22 The last component of the GMM is the apparent aleatoric variability, quantifying the natural randomness
23 of the ground-motion data – that which is not captured by the fixed- and random-effects. The aleatoric
24 residuals (ε) are tested for event depth and recording site distance dependencies in Figure 1-14. For all
25 periods ($T = 0.0, 0.1, 1.0s$), we observe no significant trends in binned means and MAD, which implies
26 the $f_{R,g}(M_W, R_{JB})$ and $f_{R,a}(R_{JB})$ of the GMM (equation 2 and 3) explain the distance scaling of ground-
27 motion sufficiently well. Heteroscedasticity of ϕ is not evident either in these plots.

28 The moderate-long period residuals of this dataset show a clear evidence of anisotropic shear-wave
29 radiation pattern in the near and intermediate distance ranges of $R_{JB} \leq 80km$, similar to that reported
30 (Kotha et al., 2019a) with the KiK-net (Kotha et al., 2018, Dawood et al., 2016) and NGA-W2 (Boore et
31 al., 2014, Ancheta et al., 2014) GMMs and datasets. In addition, there is a strong evidence of SmS
32 phases from Moho reflection in the $60km < R_{JB} \leq 200km$ distance ranges (Bindi et al., 2006), especially
33 from events originating deeper than 10km and close to Moho boundary. However, we chose not to

1   discuss these features in the response spectral domain in which the GMM residuals are estimated, but
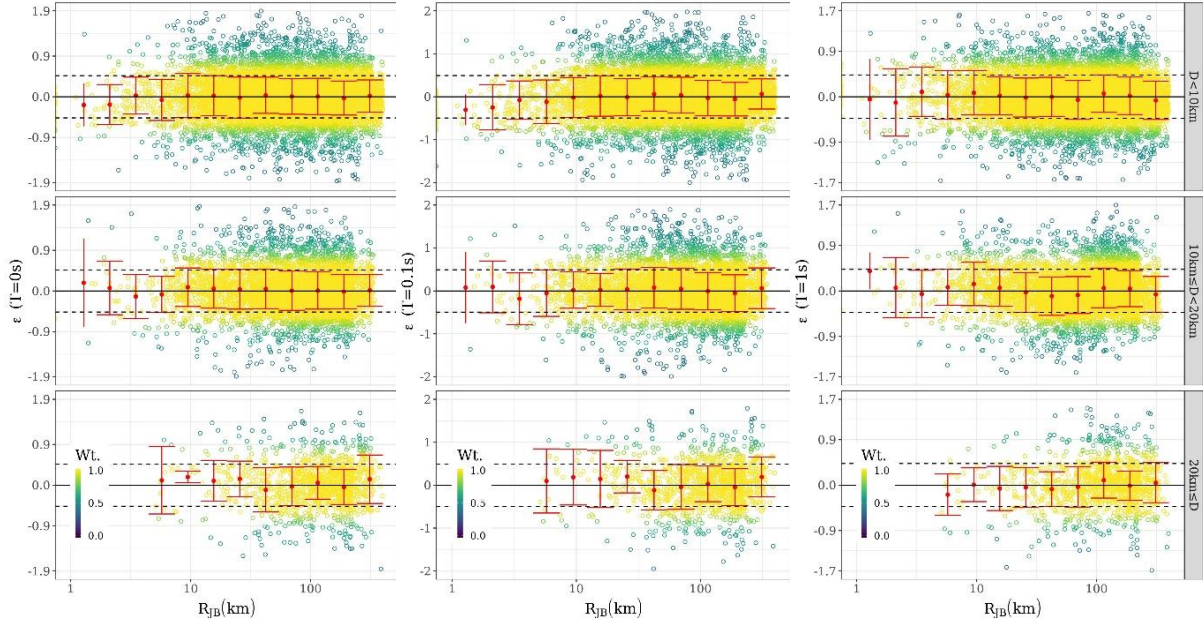2   instead with those in the Fourier domain.

Figure 1-14: Aleatoric residual trends with distance for different event depths $(D < 10km, 10km \leq D < 20km, 20km \leq D)$ *for* $T = 0.0, 0.1, 1.0 s.$

3

Application

5   The GMM presented in this study has no new explanatory parameters in its functional form compared
6   to previous pan-European GMMs. The median predictions rely only on the two generic parameters M_W
7   and R_{JB}, which constitute the fixed-effects. Of course, the standard-deviation estimates of the new model
8   are significantly larger than those of K16, but this is to be expected given the 10-fold increase in data:
9   from a greater variety of sites, tectonic regions, $M_W \leq 5.5$ events, etc. To explain the variability, without
10   introducing new parameters, we instead resolved the apparent aleatory variability into various possible
11   contributions. Therefore, the model can be used ignoring the region-to-region, source-to-source, and
12   site-to-site variabilities, but at the cost of increased aleatory variability. We provide two application
13   possibilities:

Ergodic application

15   The first approach is by ignoring all repeatable effects, i.e. the random-effects as region and site-specific
16   adjustments. The between-location, between-event, between-site, residual standard deviations can be
17   combined into an ergodic, total standard deviation $\sigma = \sqrt{\tau_{L2L}^2 + \tau_0^2 + \phi_{S2S}^2 + \phi^2}$, as shown in Figure 1-7.
18   In this case, the regional differences in anelastic attenuation, quantified by τ_{c3}, will be treated as an
19   epistemic uncertainty on far-source distance scaling. The epistemic uncertainty on the regionalized
20   anelastic attenuation coefficient $c_{3,r}$ in equation (2) is τ_{c3}. This uncertainty can be handled with a GMM
21   logic tree consisting of a slower $(c_{3,r} = c_3 + \tau_{c3})$, average $(c_{3,r} = c_3)$, and faster $(c_{3,r} = c_3 - \tau_{c3})$
22   attenuating branches with weights 0.2, 0.6, and 0.2, respectively. Consequently, the ground-motion
23   prediction is a weighted mixture of three Gaussian distributions $\mathbb{N}(ln(\mu), \sigma)$, where $ln(\mu)$ is estimated
24   from equation (1) for three values of $c_{3,r} \in (c_3, c_3 + \tau_{c3}, c_3 - \tau_{c3})$.

25   Within the context of an ergodic application, if a site has either the V_{s30} or $slope$ information available,
26   but no site-specific ground-motion recordings, then the ϕ_{S2S} in the above estimation of σ can be replaced

1   with $\phi_{S2S}^{V_{S30}}$ and ϕ_{S2S}^{slope}, whilst appending the fixed-effects of equation (1) with equation (5) and (6),

2   respectively. Figure 1-15 shows the consequent reduction of σ to $\sigma^{V_{S30}}$ and σ^{slope} values, when using

3   site-response proxies V_{s30} and $slope$, respectively. Consequently, the ground-motion predictions follow

4   the mixed Gaussian distribution $\mathbb{N}(ln(\mu) + SR, (\sigma^{V_{S30}}$ or $\sigma^{slope}))$, where $ln(\mu)$ is estimated from equation

5   (1) for three values of $c_{3,r} \in [c_3, c_3 + \tau_{c3}, c_3 - \tau_{c3}]$, and SR is estimated from equation (5) or (6).

6   The reduced aleatoric variability from using a site-response proxy is beneficial until when enough

7   ground-motion data can be collected at a site, and then $\delta S2S_s$ for the new site can be estimated using

8   equations provided in (Rodriguez-Marek et al., 2013, Villani and Abrahamson, 2015, Kotha et al., 2017,

9   Sahakian et al., 2018) etc.

10 **Region-specific application**

11 For region-specific applications, the predictions can be upgraded with the region-specific anelastic

12 attenuation and fault-zone specific adjustments. Anelastic attenuation is regionalized by adjusting the

13 generic coefficient c_3 with a region-specific value $\delta c_{3,r}$, as in $c_{3,r} = c_3 + \delta c_{3,r}$ in equation (3) , where

14 region r is decided by the location of the site. Since $\delta c_{3,r}$ are estimated from a smaller region-specific

15 sample of ground-motion recordings, it should be treated as epistemically uncertain. For this purpose,

16 standard error on $\delta c_{3,r}$ are provided as well, and these are always smaller than τ_{c3}. Treating the

17 $SE(\delta c_{3,r})$ as uncertainty on mean of a normally distributed sample, the 95% confidence interval of

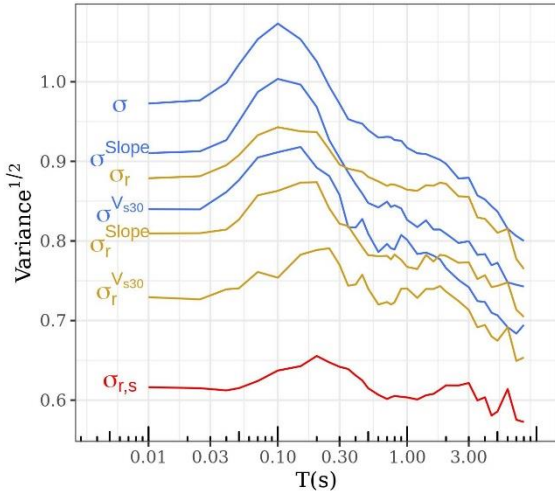18 $\delta c_{3,r}$ would be $\delta c_{3,r} \pm 1.6 SE(\delta c_{3,r})$.

Figure 1-15: Reduction in total variance estimates (σ) of the GMM for T = 0.01-8s (solid lines) from ergodic, ergodic with site-response proxy, region-specific, and region- and site-specific values. Variance estimates when using site-response proxies are indicated by the annotations with corresponding superscript, i.e. $(\sigma^{V_{S30}})$ with V_{s30}, and to (σ^{slope}) with $Slope$. Annotations with subscript r correspond to the variances for regionalized predictions, i.e. regionalized anelastic attenuation $c_{3,r} = c_3 + \delta c_{3,r}$ and earthquake source $e_{1,f} = e_1 + \delta B_f$. Values annotated with subscript r, s correspond to region- and site-specific predictions i.e. $e_{1,f,s} = e_1 + \delta B_f + \delta B_s$ along with $c_{3,r} = c_3 + \delta c_{3,r}$ in equation (1)

19

20 Similarly, depending on the location (area source) of the earthquake, the GMM predictions can be further

21 regionalized by adjusting e_1 in equation (1) to $e_{1,l} = e_1 + \delta L2L_l$, where l identifies earthquake location

22 or area source. Since $\delta L2L_l$ is estimated from a smaller area source specific ground-motion sample, the

23 95% confidence interval is bounded by $\delta L2L_l \pm 1.6 SE(\delta L2L_l)$. A reduction of up to 10% in σ is achieved

24 by dropping the τ_{L2L} from aleatoric variance, resulting in a smaller $\sigma_r = \sqrt{\tau_0^2 + \phi_{S2S}^2 + \phi^2}$, as shown in

25 Figure 1-15. Consequently, the region-specific ground-motion predictions follow the mixed Gaussian

26 distribution $\mathbb{N}(ln(\mu_r), \sigma_r)$, where $ln(\mu_r)$ is estimated from equation (1) for three values of $c_{3,r} \in [c_3 +$

27 $\delta c_{3,r}, c_3 + \delta c_{3,r} + 1.6 SE(\delta c_{3,r}), c_3 + \delta c_{3,r} - 1.6 SE(\delta c_{3,r})]$, and three values of $e_{1,l} \in [e_1 + \delta L2L_l, e_1 +$

28 $\delta L2L_l + 1.6 SE(\delta L2L_l), e_1 + \delta L2L_l - 1.6 SE(\delta L2L_l)]$ – a total of 9 combinations reflecting the increased

29 epistemic uncertainty following a reduction in apparent aleatory variability from σ to σ_r.

20

1 Region- and site-specific application

Partially non-ergodic region- and site-specific ground-motion predictions are possible for those sites with $\delta S2S_s$ provided with this GMM or for new sites with sufficient ground-motion data. $\delta S2S_s$ for the 1357 sites in the ESM dataset are provided, along with the $\delta c_{3,r}$ of their location, and $\delta L2L_l$ of nearby earthquake sources. Since between-site variability (and between-fault as well) does not apply for site-specific predictions, the reduction in apparent aleatory variability is enormous, i.e. $\sigma_{r,s} = \sqrt{\tau_0^2 + \phi^2}$ is about 40% smaller than $\sigma = \sqrt{\tau_{l2l}^2 + \tau_0^2 + \phi_{S2S}^2 + \phi^2}$, as shown in Figure 1-15. However, the reduction in aleatory variability will be accompanied by additional epistemic uncertainty. In addition to those in region-specific predictions, uncertainty on (the mean) $\delta S2S_s$ should be accounted with $\pm SE(\delta S2S_s)$. Region- and site-specific predictions therefore are a mixture of 27 Gaussian distributions $\mathcal{N}(ln(\mu_{r,s}), \sigma_{r,s})$, where $ln(\mu_{r,s})$ is estimated from equation (1) for three values of $c_{3,r} \in [c_3 + \delta c_{3,r}, c_3 + \delta c_{3,r} + 1.6SE(\delta c_{3,r}), c_3 + \delta c_{3,r} - 1.6SE(\delta c_{3,r})]$, three values of $e_{1,l,s} \in [e_{1,l} + \delta S2S_s, e_{1,l} + \delta S2S_s + 1.6SE(\delta S2S_s), e_{1,l} + \delta S2S_s - 1.6SE(\delta S2S_s)]$, wherein $e_{1,l} \in [e_1 + \delta L2L_l, e_1 + \delta L2L_l + 1.6SE(\delta L2L_l), e_1 + \delta L2L_l - 1.6SE(\delta L2L_l)]$.

Towards non-ergodic Ground-Motion Predictions

For fault-zones, attenuating regions, and sites with sufficient amount of recordings the epistemic uncertainty on the random-effect adjustments are negligible with respect to the random-effect and standard deviations. Collecting more ground-motion recordings is principal in moving towards non-ergodic predictions. The benefits in resolving the ergodic assumption and progressing towards region- and site-specific in ground-motion prediction is demonstrated Figure 1-16. In this plot, predictions for the M6.5 Norcia event of the central Italy sequence, occurred on 30th October, 2016, are compared to the response spectra recorded at three sites covered by the Italian strong motion network (Gorini et al., 2010). These sites are identified by the network code IT in the ESM dataset: 1) permanent, free-field station LSS (Leonessa) with $V_{s30} = 1091 m/s$ located 25km from the event epicenter, 2) permanent, free-field station MVB (Marsciano Monte Vibiano) with $V_{s30} = 1046 m/s$ located 65km from the event epicenter and, 3) permanent, free-field station PSC (Pescasserolis) with $V_{s30} = 1000 m/s$ located 110km from the event epicenter. The three columns in Figure 1-16 correspond to the three stations.

These event and stations are selected to demonstrate progressively (in Figure 1-16) the impact of moving from ergodic prediction relying on V_{s30} as site-response proxy (top row), through region-specific predictions (middle row) considering regional (Northern and central Apennines West) anelastic attenuation ($c_{3,r} = c_3 + \delta c_{3,r}$) and adjustment specific to the area source ($e_{1,l} = e_1 + \delta L2L_l$) containing the event (SERA ID: "ITAS308"), to region- and site-specific predictions (bottom row) from an additional site-specific adjustment ($e_{1,f,s} = e_1 + \delta L2L_l + \delta S2S_s$). Both the median prediction and standard deviation change in process, which is reflected by the colored ribbon in Figure 1-16. The $\delta S2S_s(T = 0.01 - 8s)$ of these sites are estimated from 29, 15, and 20 records from predominantly small-moderate earthquakes (details in the Figure 1-16 panels). A few comments on this figure:

1. The ergodic median predictions (central line) and one $\sigma^{V_{s30}}$ interval (ribbon) are systematically above the observed response spectra at the 3 *rock* sites, located at near (25km), intermediate (65km), and far (110km) source distances. This is likely because the M6.5 Norcia event produced relatively weaker ground-motions compared to other large magnitude events recorded in Greece and Turkey – quantified into their respective δB_e values. Since the ergodic predictions consider all event, region, site, and record variabilities as aleatoric, the $\sigma^{V_{s30}}$ (Figure 1-15) is large yet not large enough contain the M6.5 event observations within $\pm\sigma^{V_{s30}}$ boundaries.

Research and Development Program on
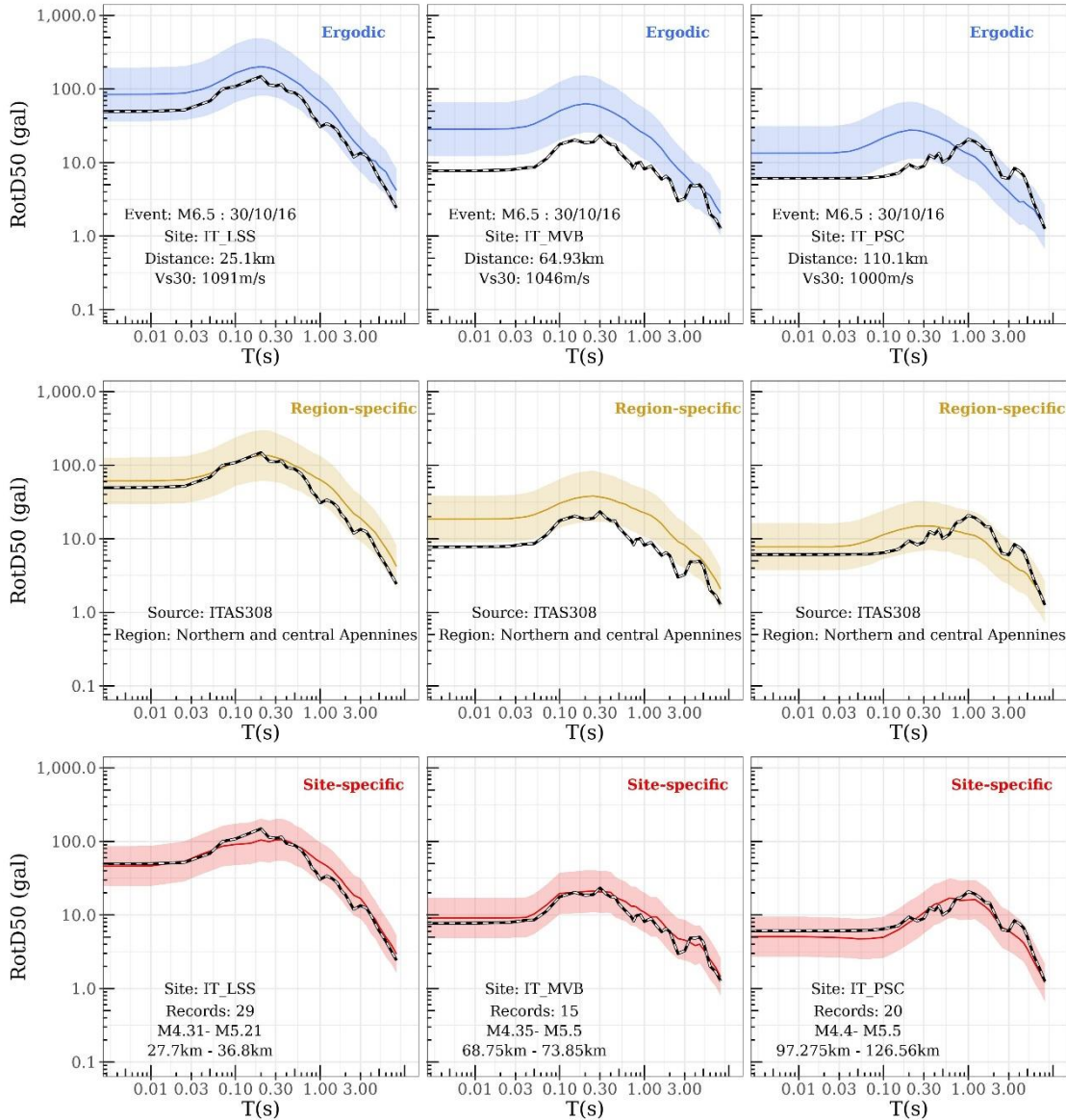Seismic Ground Motion

Figure 1-16: Comparison of ergodic (top row), region-specific (middle row), and sites-specific (bottom row) ground-motion median (solid colored line) and variability (colored ribbon) predictions for the M6.5 Norcia earthquake with the observed response spectra (solid dashed line) at three sites in Italy (column wise).

2. Region-specific ground-motion predictions for these sites are achieved by adjusting the GMM with the $\delta c_{3,r}$ of the Northern and central Apennines (West), in which the sites are located; and the δB_f of the SERA area source ITAS308, in which the M6.5 event occurred (along with a few other prominent events and aftershocks). The epistemic uncertainties of these adjustments are relatively very small given the large number of recordings. In the middle row of Figure 1-16, we notice the observed response spectra are closer to region-specific predictions than to the ergodic predictions. $\delta c_{3,r}$ and $\delta L2L_l$ of these regions are both lower than the pan-European average (which is zero), meaning the region attenuates short-period ground-motions faster and the events on average produce weaker ground-motions than elsewhere in pan-European region.

It is interesting to note that, at short distances (site IT_LSS) the $\delta c_{3,r}$ has no effect on region-specific predictions, and the shift is mostly from $\delta L2L_l$ – and so is at intermediate distance (site IT_MVB). At far-source distances (site IT_PSC), the combined effect of $\delta c_{3,r}$ and δB_f worked

1   well to capture the observed response spectra within the narrower $\pm\sigma_r^{V_{S30}}$ (Figure 1-15) range
2   about the region-specific median.

3   3. Region and site-specific predictions (site-specific in short) for the three sites are shown in the
4   bottom row of Figure 1-16. Along with the curves, details on the number of recordings,
5   magnitude and distance ranges (1st and 3rd quantile) of the recordings are provided. The
6   additional adjustment to the preceding region-specific predictions is through $e_{1,l,s} = e_1 + \delta L2L_l +$
7        $\delta S2S_s$. While most of the data in estimating the $\delta S2S_s$ of these sites is from small-moderate
8   sized earthquakes, the site-specific predictions fit quite well with the observations for the large
9   M6.5 event. Since $\delta S2S_s$ are used to adjust the region-specific ground-motions, the V_{s30}
10   becomes irrelevant, while $\phi_{S2S}^{V_{S30}}$ is dropped from $\sigma_r^{V_{S30}}$ resulting in a smaller $\sigma_{r,s}$.

11 In the above example, we demonstrated that applying region-specific adjustments noticeably improved
12 the match between observations and predictions. The best agreement was clearly from using site-
13 specific adjustments. To substantiate this claim, we performed a 10-fold cross-validation exercise to
14 verify if the introduction of the various random-effects into GMM functional form indeed improves its
15 prediction capabilities. In doing so, we re-run the regression with three functional forms:

16   • **Ergodic** model with no regionalization of anelastic attenuation, no regionalization of source
17   terms, and no random-effect to capture site-to-site variability
18   • **Regional** model with regionalization of anelastic attenuation and source terms, leaving out the
19   random-effect to capture site-to-site variability
20   • **Site-specific** model identical to the GMM presented here i.e. regionalization of anelastic
21   attenuation and source terms, and the site-to-site random-effect

22 To perform the cross-validation, the dataset is split into 10 parts with non-overlapping events. Meaning,
23 earthquakes (and records) are exclusive to their subsets and do not feature in any other subset. We
24 regress the three models on any nine subsets combined, and test the predictions on the tenth subset.
25 Root-mean-squared-errors are estimated for each trial and then averaged over the ten trials. This
26 exercise is repeated for IMs: $PGA, PGV, SA(T = 0.1, 0.2, 0.5, 1, 2, 4s)$.

27 Figure 1-17 shows a histogram of RMSE for each IM, from the three models. The reduction in RMSE
28 from ergodic to region-specific GMMs is clear and most prominent at short periods. Towards longer
29 periods, the improvement is less pronounced but is still substantial. This is because the regionalization
30 random-effects are focused on the capturing variabilities in high-frequency ground-motions. In Figure
31 1-7, we notice the overall variability σ peaks at short periods. In Figure 1-8 and Figure 1-9, the largest
32 regional variability of anelastic attenuation τ_{c3} and area sources τ_{L2L} is also at short periods $T \leq 0.2s$.
33 Without regionalization, along with the increased the short period ground-motion prediction variability
34 and reduced precision of an ergodic median, the predictive capability (measured as RMSE) of the GMM
35 is reduced as well.

36 Across all the periods, i.e. the entire response spectra, the best predictive capabilities are those of
37 region- and site-specific GMM. In Figure 1-15 the largest reduction in σ is achieved not from using V_{s30}
38 or $slope$ as the site-response proxy, but from using $\delta S2S_s$ as the site-specific adjustment. However, it is
39 unlikely that every site has sufficient ground-motion data to estimate its site-specific $\delta S2S_s$. In that case,
40 alternative site-response proxies are sought to predict the $\delta S2S_s$, as in (Kotha et al., 2018, Weatherill et
41 al., 2019). However, even in these studies, while the long period site-response could be partially
42 explained using some geotechnical parameters, short period site-response is much more variable –
43 even among the so-called reference rock sites (Bard et al., 2019)
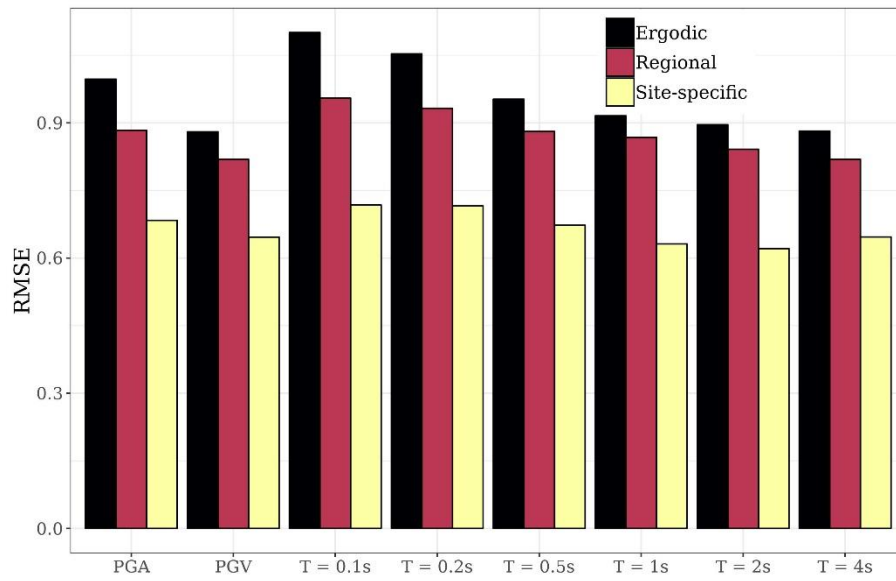
Figure 1-17: 10-fold cross validation statistics comparing the predictive capabilities of ergodic, regionalized, and site-specific GMM versions at various periods

1

1 # Chapter 2

2 # Ground-Motion Model in Fourier Domain

3 ## Introduction

4 Typical ground-motion models (GMMs) used in seismic hazard and risk assessments predict the random
5 distribution of ground-motion in terms of spectral amplitude (SA), i.e. damped response of an elastic
6 single-degree-of-freedom oscillator with fundamental resonance period T. In chapter 1, we elaborated
7 the regionalized GMM derived from the European Strong-Motion (ESM) dataset, developed specifically
8 to predict the 5% damped response spectra SA(T) of shallow crustal earthquakes in Europe and Middle-
9 Eastern regions. The GMM model is capable of predicting SA(T) (GMM-SA from hereon) accounting the
10 regional differences in distance decay through $\delta c_{3,r}(T)$ and average source effects through $\delta L2L_l(T)$,
11 and site-specific effects through $\delta S2S_s(T)$ random-effect adjustments to the generic GMM-SA median.

12 However, correlating the random-effects estimated in spectral domain to physical properties may not be
13 appropriate. For instance, the short-period SAs integrate features of moderate-high frequency Fourier
14 amplitudes (FAS), making it difficult to interpret physically the quantified regional random-effects at
15 (approximately) $T \leq 0.5s$. Therefore in this chapter, we introduce the GMM regressed over the Fourier
16 amplitude version of the ESM dataset (GMM-FAS from hereon), and attempt to explain the estimated
17 regional differences (also as random-effects) in terms of differences in physical properties across
18 regions and sites.

19 The ground-motion data selection, regionalization models, functional form, and regression methods are
20 identical, except for a few minor changes with respect to the GMM in spectral domain:

21 1. The data visualized in Figure 1-1 is from shallow crustal earthquakes in the ESM dataset. To filter
22   out records not suitable for a shallow crustal GMM development, we modified and adopted the
23   selection criteria suggested in the Bindi et al. (Bindi et al., 2018b) preliminary sanity check. The
24   only additional record selection criterion relevant to the GMM-FAS is the low-pass frequency filter
25   limit. For the GMM-SA regression of $SA(T)$, we chose only the records with a high-pass filter
26   frequency of both horizontal components $f_{hp} \leq 0.8/T$. While for the GMM-FAS regression
27   of $FAS(f)$, we chose the records with high-pass frequency $f_{hp} \leq 0.8f$ and low-pass frequency $f_{lp} \geq$
28   $f/0.8$, of both horizontal components. Following the above criteria, the number of records available
29   for GMM-FAS regression is 2918 at $f = 0.1Hz$, 16452 at $f = 1Hz$, and 4580 at $f = 28Hz$.
30 2. The GMM-FAS is developed to predict the geometric mean of the two horizontal FAS components,
31   for 27 values of f in the range $0.12Hz - 28.20Hz$.
32 3. The mixed-effects GMM-FAS has the same fixed and random-effects as in GMM-SA. The only
33   change in functional form (equations $1 - 4$) is in the geometric spreading component $f_{R,g}$. While
34   that of GMM-SA is a function of both magnitude and distance, as in $f_{R,g}(M_W, R_{JB})$, the magnitude
35   dependence is dropped from GMM-FAS, as in $f_{R,g}(R_{JB})$.

36 ## Activity Index Regionalization

37 (Chen et al., 2018) introduced a fully data-driven global tectonic regionalization model for selection of
38 ground-motion models in seismic hazard applications. Based on a fuzzy logic workflow, they have
39 rendered a regular grid with a spacing of 0.5°, wherein each cell is assigned a probability of being an
40 active tectonic region – the Activity Index (AI), as shown in Figure 2-1. Sparing details, AI in a grid cell
41 is calculated from the following fuzzy rules:

42 1. IF [seismic moment rate density] is 'High', AND [1Hz Lg coda Q] is 'Low', AND [S-wave velocity
43   variation at 175km] is 'Low', THEN the region is ['Active'] – High AI

2. IF [seismic moment rate density] is 'Low', AND [1Hz Lg coda Q] is 'High' AND [S-wave velocity
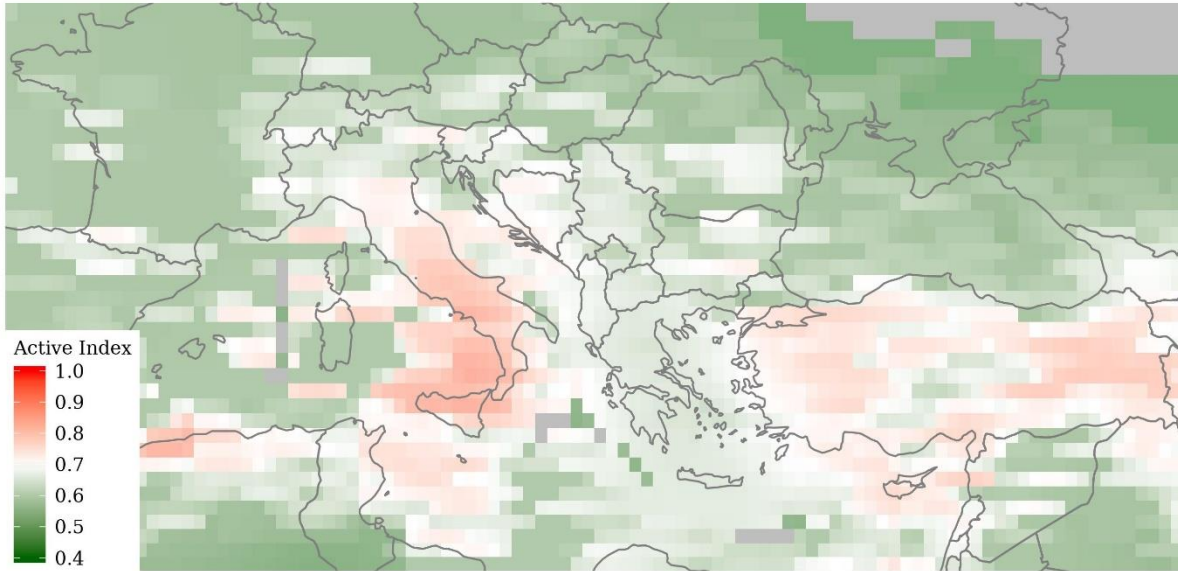   variation at 175km] is 'High', THEN the region is ['Stable'] – Low AI

Figure 2-1: Activity Index map of pan-European region

AI is derived as a of combination of seismic moment rate density (Weatherill et al., 2016), 1Hz Lg coda
Q (Mitchell et al., 2008), and shear-wave velocity variation at 175km (Ritsema et al., 2011). We use this
dataset to evaluate the various regional variabilities quantified as the GMM random-effects.

Results and Discussion

With the data selection and functional form set, we perform the robust linear mixed-effects regression.
The regression results comprise of fixed-effect coefficients and covariance matrices, random-effect
values, weights and standard errors, residuals, and variances. Similar to the GMM-SA, outlier events,
sources, regions, stations, and recordings are flagged as well.

Fixed-effects

Figure 2-2 presents the predicted Fourier spectra for various scenarios of interest. In this plot, we show
predicted FAS:

i.   For [M4, M5.5, M7] implying events with $M_W = 4, 5.5, 7$

ii. [Shallow, Intermediate, Deep] to illustrate the function of $h_D = 4, 8, 12 km$ for events with depth
     $D < 10 km, 10 km \leq D < 20 km, 20 km \leq D$, respectively

iii. [Average, Faster, Slower] attenuating regions to illustrate the effect of $c_{3,r} = c_3 + \delta c_{3,r}$, with
     $\delta c_{3,r} = 0, -\tau_{c3}, +\tau_{c3}$, respectively

In the left panel, showing the near-source predictions, we notice that the depth-dependence has little
effect on the amplitudes. However, at closer distances, e.g. $R \leq 5 km$, the differences become noticeably
large. For the $(M7, 10 km)$ scenario, the epistemic uncertainty (green ribbon) on the median is wide
enough to cover the variation with depth. A large part of this epistemic uncertainty is from the lack of
near-source data from large magnitude events, necessary to constrain the magnitude-scaling $f_M(M_W)$
component of the GMM at $M_W \geq M_h = 6.2$. Moreover, a substantial number of recordings do not qualify
the selection criteria on the usable frequency range for GMM-FAS regressions at $f \leq 0.5 Hz$. For
instance, out of ~16000 records only ~3000 qualify the low and high-pass filtering criterion.

1   In the right panel, FAS predictions at far-source distances are shown. Evidently, the $\delta c_{3,r} = 0, -\tau_{c3}, +\tau_{c3}$
2   adjustments become active at $f \geq 2Hz$ in far-source predictions. At lower frequencies (nearer
3   distances), the differences are much smaller – which is to be expected since c_3 coefficient is meant to
4   capture the (apparent) anelastic attenuation of high frequency ground-motions.
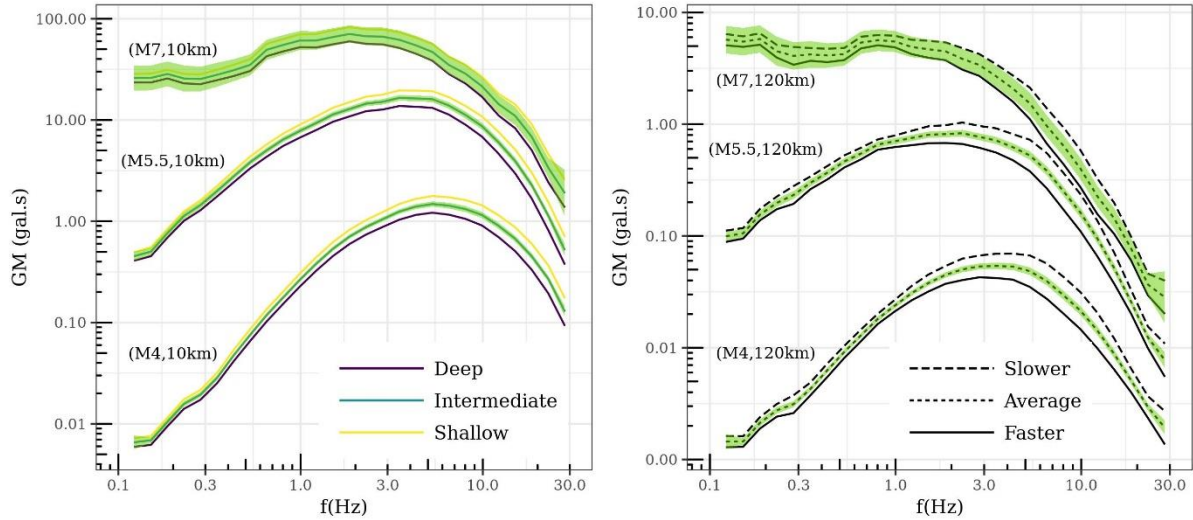

*Figure 2-2: Predicted Fourier spectra of the GMM for various scenarios, differentiated by color for shallow ($D <$
$10km$), intermediate ($10km \leq D < 20km$), and deep ($20km \leq D$) events in the left panel. In the right panel are
the response spectra differentiated by regional anelastic attenuation (Slower, average, faster)*

5

6   Along with the depth and anelastic attenuation dependencies, we notice that with increasing magnitude
7   the spectra become flatter in low-moderate frequency range, as the (apparent) corner-frequency shifts
8   towards lower frequencies for larger events. At near source distances (left panel), the spectra decay
9   rapidly beyond $f \geq 10Hz$, while at far source distances (right panel) this behavior is observed earlier
10   at $f \geq 5Hz$, most likely from the anelastic attenuation of high frequencies.

11   **Variances**
12   Before discussing the random-effects and residuals in following sections, there are few inferences
13   derived from the random-effect and residual variances in Figure 2-3. In this plot, $\phi_{S2S}, \tau_{L2L}, \tau_0, \tau_{c3}$ are the
14   random-effect standard deviations of between-site, between-location (area sources), between-event
15   (after between-location correction), and between-region (anelastic attenuation) random variables,
16   respectively. ϕ is the residual standard deviation. The total-sigma of the GMM-FAS $\sigma =$
17   $\sqrt{\phi_{S2S}^2 + \tau_{L2L}^2 + \tau_0^2 + \phi^2}$ does not include τ_{c3}, because the $\Delta c_3 = \mathbb{N}(0, \tau_{c3})$ values are intended for use
18   as epistemic uncertainty on anelastic attenuation of GMM, only at the far source distances $R \geq 80km$
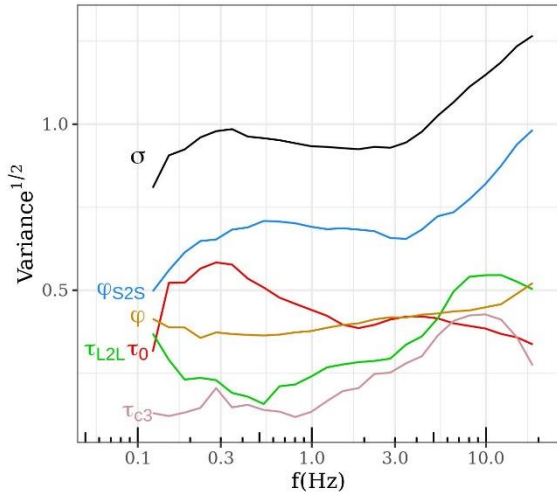19   (more discussion in later sections).

Figure 2-3: Random-effect, residual, and total variance estimates of the GMM for $f = 0.1 - 20Hz$ (solid lines)

2 Clearly, all the random-variances are comparable in size; which means the random-effect groups are
3 statistically significant. The largest variability is however the site-to-site response variability, captured by
4 the between-site standard deviation ϕ_{S2S}. Increasing monotonically at $f \geq 3Hz$, ϕ_{S2S} suggests that site-
5 response (in the dataset) is highly variable at moderate-high frequencies. For instance, ground-motion
6 amplification at a site with $\delta S2S_s(f = 10Hz) = 1.5 * \phi_{S2S}(f = 10Hz)$ is 20 times larger than that at a site
7 with $\delta S2S_s(f = 10Hz) = -1.5 * \phi_{S2S}(f = 10Hz)$. The large variability in site-response and the
8 consequently large ϕ_{S2S} (the largest contributor to σ) suggests site-specific ground-motion predictions
9 may soon become necessary.

10 The next largest random variance is that of between-event variability quantified into τ_0. We note that a
11 part of the spatial event-to-event variability is quantified in to the source location-to-location (area
12 sources containing local events) variability τ_{L2L}. Apparently, variability of event-specific properties is the
13 highest at $f \leq 0.5Hz$. Seismic moment and moment-magnitude are the event-specific parameters
14 estimated at these frequencies. For a GMM with M_W (from EMEC catalog) as an explanatory variable,
15 such large between-event variability at $f \leq 0.5Hz$ suggests large differences in observed ground-
16 motions between events of identical M_W. The most likely cause, to our understanding, is errors in M_W in
17 the dataset. A few studies (Kuehn and Abrahamson, 2017, Holmgren and Atkinson, 2018) demonstrated
18 that M_W uncertainty is contributor to the between-event variability at long period spectral accelerations,
19 which are analogues to low frequency Fourier amplitudes. Beyond $f \geq 1Hz$ the τ_0 values are almost
20 constant.

21 The counter-part of τ_0 is the between-location variability τ_{L2L}, which captures the average event-to-event
22 variability while events are localized into SERA area sources. τ_{L2L} values are much smaller than τ_0
23 at $f < 1Hz$, and increase monotonically above τ_0 at $f \geq 5Hz$. Assuming the M_W are now quantified
24 into τ_0, we discuss the physical meaning of τ_{L2L} in the subsequent sections.

25 Region-to-region variability of anelastic attenuation is quantified into τ_{c3}. Only the high frequency
26 ground-motions are attenuated exponentially with distance. Therefore, τ_{c3} increases towards high
27 frequencies in Figure 2-3. The residual standard deviation ϕ, corrected for all parametric, regional, and
28 site-specific effects, remains almost constant across the frequency range. More on random-effect and
29 residual analyses will be presented in the following sections.

30 **Random-effects Analyses**
31 Figure 2-3 illustrates the significance of the chosen random-effect groups, and the frequency
32 dependence of their random variances. Physical meaning of the frequency dependence of random-
33 variance and the random-effects, i.e. the values for each level in a random-effect group, will be

1   discussed below. It is necessary to validate the random-effects by correlating them to a physical
2   parameter or a phenomenon. Reason being, since random-effects are estimated only for the regions
3   and sites with ground-motion data available for the GMM regression, new regions and sites with no
4   ground-motion data do not benefit. However, correlating random-effects to a physical parameter may
5   allow, in a limited way, exporting region and site-specific adjustments to new locations with at least the
6   correlated physical parameter available.

7   *Anelastic attenuation variability*

8   Anelastic attenuation of high frequency ground-motions comes into play at intermediate-far source
9   distances (e.g. $R \geq 80km$). The coefficient c_3 in GMM median captures the average rate of exponential
10 decay of ground-motion, while c_1 captures the linear decay. Substantial correlation between c_3 and c_1
11 estimates are to be expected because they together model the decay of ground-motions with distance.
12 Therefore, it is more appropriate to refer to c_3 as a coefficient for *apparent* anelastic attenuation. $\delta c_{3,r}$ is
13 meant to capture regional variability of this exponential decay. Figure 2-4 shows the frequency
14 dependence of $\delta c_{3,r}$ for the 42 regions identified with subscript r. The region-to-region variability is
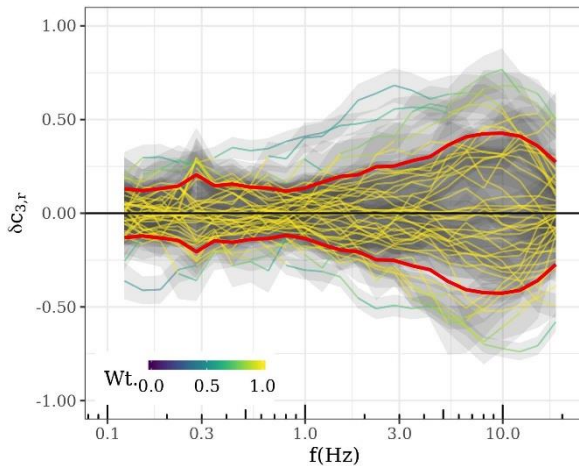15 largest at $f \geq 5Hz$, emphasizing the large τ_{c3} in the Figure 2-3.

Figure 2-4: $\delta c_{3,r}$ for $f = 0.1 - 20Hz$. Each line corresponds to one of the 42 attenuation regions, with colors indicating their weight in robust regression. Overlain red curves mark the $\pm\tau_{c3}$ values. Regions with $\delta c_{3,r}(T)$ beyond $\pm 1.345\tau_{c3}(T)$ are given a lower than a unit weight

16

17 Figure 2-5 maps the regional variability of $\delta c_{3,r}$ at $f = 0.3, 1, 3, 10Hz$ in the pan-European region. In this
18 figure, red polygons locate regions with slower than pan-European average of anelastic attenuation c_3
19 i.e. $\delta c_{3,r} > 0$; and vice versa with $\delta c_{3,r} < 0$ for the blue polygons. Regions with insufficient data and
20 thereby large epistemic uncertainty on their $\delta c_{3,r}$ are white in color, and given $\delta c_{3,r} = 0$. There are few
21 interesting features in these maps:

22 1. Regions with similar attenuation characteristics are spatial clustered, although this is frequency
23   dependent. In general, regions characterized with high seismic activity (e.g. Italy and Greece) show
24   strong attenuation compared to those with lower seismic activity (e.g. central Europe)
25 2. The best-sampled regions are in central Italy with 5505 records from Northern and central
26   Apennines W (West), 3199 records from Northern and central Apennines E (East). While
27   attenuating faster than the pan-European average, there appears a strong contrast between these
28   adjacent regions. The western region has already been reported to attenuate faster than the
29   eastern region. While the difference is negligible at low frequencies ($f = 0.348Hz$ top-left panel), at
30      $f = 9.903Hz$ (bottom-right panel) the difference between these two regions is 0.2 – which roughly
31   translates into 10% larger ground-motions at $R = 80km$ towards east.
32 3. The fastest attenuation in the Aegean Sea is observed in the Gulf of Corinth, where the sites record
33   highly attenuated ground-motions while travelling across the Aegean volcanic arc.
34 4. Contrast in high frequency attenuation is observed around the Alps regions. In addition, some
35   differences are noticeable between west, north, and central Anatolia. Although not conclusive,

1 rapidly changing crustal thickness (Grad et al., 2009) and associated crustal properties may
2 partially explain the rapid change in attenuation properties in these regions.
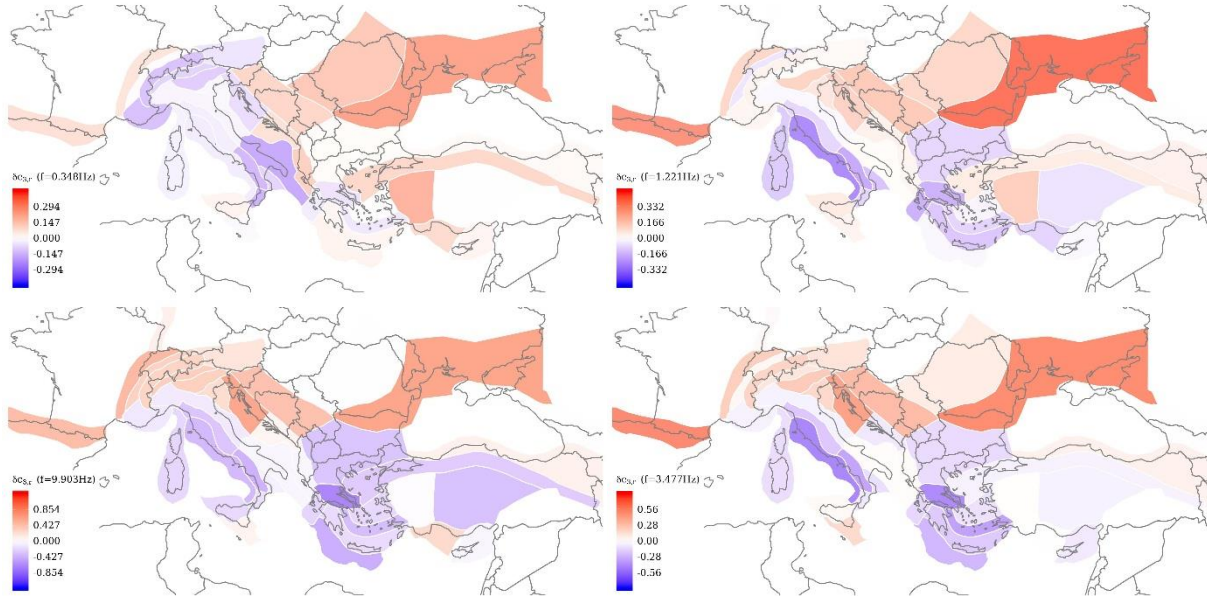

Figure 2-5: $\delta c_{3,r}$ variation across the 42 regions in ESM dataset for $f = 0.3, 1, 3, 10 Hz$ (clockwise from top-left to bottom-left panels). Blue polygons locate regions with anelastic attenuation faster than the pan-European average, red polygons locate regions with slower attenuation, and white polygons are regions close to the average. Regions with fewer ground-motion observations, thereby larger epistemic error on $c_{3,r}$, are more transparent and appear white. Note that the color scale is limited to vary between $\pm 3 * \tau_{c3}(f)$ for each frequency f

3

4   We note that changing the resolution or geometry of the regions may change the spatial variability and
5   values of $\delta c_{3,r}$ as well (e.g. (Landwehr et al., 2016, Kuehn et al., 2019)). However, for the current
6   configuration, we seek physical parameters that may correlate to $\delta c_{3,r}$ (at different frequencies). A recent
7   study (Sahakian et al., 2019) using a large data set of small-magnitude earthquakes in Southern
8   California suggested that heterogeneity in crustal velocity is only weakly correlated to anelastic
9   attenuation. Regional variability of anelastic attenuation may in fact be a combination of regional
10 variability of crustal shear-wave velocity, crustal quality factor (e.g. coda Q), mantle temperature
11 influencing the rigidity of the crust, and other parameters that may not be mappable across the pan-
12 European region. Activity Index is one such compound parameter that we test in this study.

13 Activity Index (AI) is a data-driven continuous parameter inferred from a fuzzy combination of shear-
14 wave velocity, seismic moment rate density, and crustal quality factors across the globe. A 0.5^0 gridded
15 map of AI was generated by (Chen et al., 2018) for the sole purpose of regionalizing GMMs or selecting
16 suitable GMMs for a region with no region-specific ground-motion data. In our exercise, we extracted
17 the AI for every site location in the ESM dataset. A region with n sites will therefore have n values of AI,
18 which can serve as an epistemic uncertainty on the region-specific AI. Figure 2-6 shows the loess fit
19 (local trends) between the $\delta c_{3,r}$ of the 42 regions and the AI of the sites located within each region. A
20 strong negative correlation is evident at moderate-high frequencies (bottom panels), where regional
21 variability τ_{c3} is the largest.

22

23

Research and Development Program on
Seismic Ground Motion

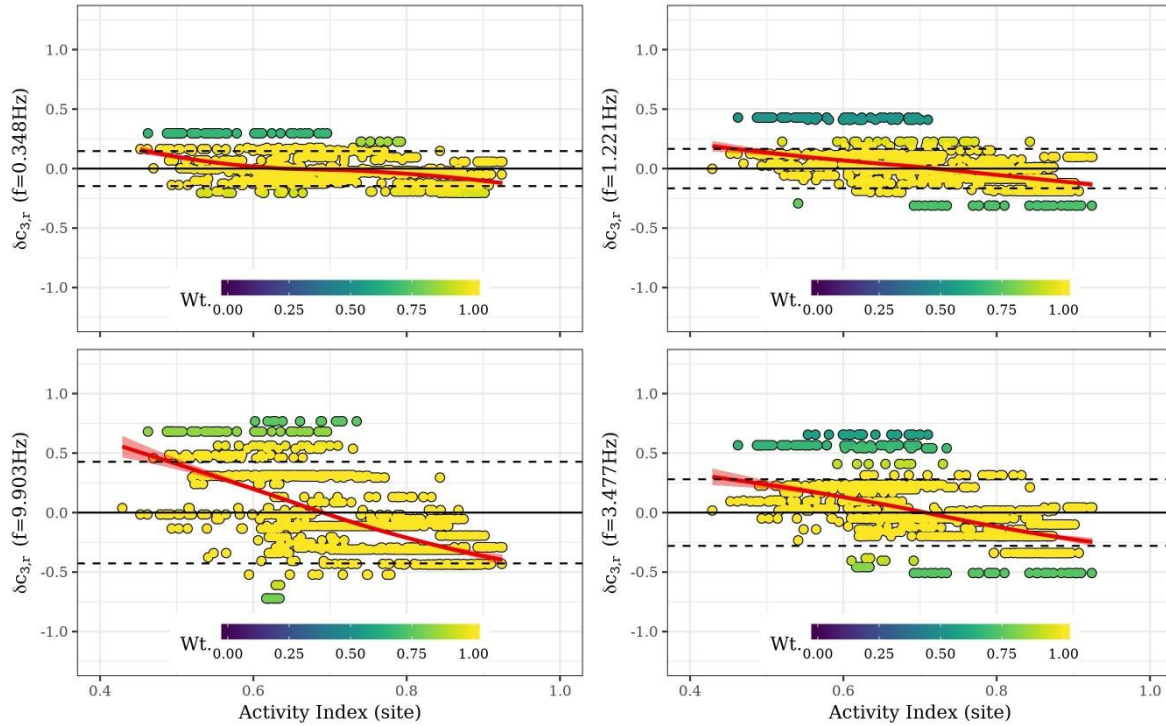*Figure 2-6: $\delta c_{3,r}$ of the 42 regions versus Activity Index at site locations within each region, for $f = 0.3, 1, 3, 10 Hz$ (clockwise from top-left to bottom-left). The red lines are loess fits between the two parameters. Marker colors indicate the weight assigned to $\delta c_{3,r}$ of each region in the rlmm regression*

1

2 The negative correlation between $\delta c_{3,r}$ and AI in Figure 2-6 suggests that regions with high seismic rate
3 density, low shear-wave velocity, and low 1Hz coda Q (therefore, high AI) attenuate significantly faster
4 than regions more likely to be cratonic (low AI). (Chen et al., 2018) indicate that the regional variability
5 of AI is dominated by regional variability of seismic moment rate density in active crustal regions ($AI \geq$
6 0.7), and to that of shear-wave velocity and 1Hz code Q in relatively stable regions ($AI < 0.7$). ESM
7 dataset contains sites located in regions with $0.4 \leq AI$ as seen in Figure 2-6. The smooth transition of
8 $\delta c_{3,r}$ between stable cratonic ($0.4 \leq AI < 0.7$) to the more seismically active regions ($0.7 \leq AI \leq 1$) is
9 indication that it is a physically meaningful random-effect. However, these regionalization models are
10 different in nature: Activity Index is fully data-driven and gridded, while the regionalization used in GMM
11 regression is based on expert elicitation and polygonised. In that sense, although there is a decent
12 agreement, neither of the models may sufficiently replace the other.

13 Figure 2-7 shows the distribution of AI within each of the attenuation region. The regions are ordered in
14 decreasing order of $\delta c_{3,r}(f = 10 Hz)$ from top to bottom. This figure is to illustrate the exclusivity of the
15 two GMM regionalization models. For instance, the two best-sampled regions, Northern and central
16 Apennines W (West) and Northern and central Apennines E (East), despite their $\delta c_{3,r}(f = 10 Hz)$ values
17 differing by 0.2 still have significant overlap of AI ranges i.e. $0.68 \leq AI \leq 0.88$ and $0.62 \leq AI \leq 0.84$,
18 respectively. Meaning, data-driven AI by itself may not resolve the differences between these two
19 adjacent regions with contrasting attenuation characteristics, as efficiently as the more subjective
20 regionalization model. In lieu of more refined and unified regionalization models, we foresee using both
21 the models in correspondence to explain and predict attenuation characteristics ($\delta c_{3,r}$) for regions
22 outside the ESM dataset.

23

Figure 2-7: Distribution of Activity Index within each region color-coded and plotted (from top to bottom) in decreasing order of $\delta c_{3,r}(f = 10Hz)$

1

2 *Source variability*

3 Source variability is divided into two components in this model: variability across localized earthquake
4 area sources $\Delta L2L = \aleph(0, \tau_{L2L})$, and the location corrected between-event variability $\Delta B_{e,l}^0 = \aleph(0, \tau_0)$.
5 Since events are exclusive (nested in) to their respective area sources, $\delta L2L_l$ quantifies the *average* of
6 the nested events' ground-motion characteristics i.e. $\delta B_{e,l}^0 = \delta B_e - \delta L2L_l$; all notations as in (Al Atik et
7 al., 2010). Figure 2-3 illustrates the frequency dependence of τ_{L2L} and τ_0. It appears the two random-
8 variances capture disjoint frequency dependent earthquake characteristics, where $\tau_0 > \tau_{L2L}$ at low-
9 moderate frequencies, and vice versa at high frequencies. Therefore, these two random-effects will be
10 analyzed in parallel.

11 Figure 2-8 shows the $\delta L2L_l(f = 0.1 - 20Hz)$ of the 134 area sources in ESM dataset. Reiterating Figure
12 2-3, the scatter of $\delta L2L_l$ is significantly increases at $f \geq 5Hz$ in Figure 2-8. The epistemic uncertainties
13 on $\delta L2L_l$ are generally smaller than τ_{L2L}. In this regard, dropping τ_{L2L} from the aleatoric variability and
14 using instead the $\delta L2L_l \pm SE(\delta L2L_l)$ adjustments to regionalize the GMM predictions can be
15 recommended. A database of $\delta L2L_l$, $SE(\delta L2L_l)$, and the rlmm weights indicating outliers is provided for
16 analyses and applications. For instance, Figure 2-8 suggests that the number of detected outliers, along
17 with τ_{L2L}, increases towards higher frequencies. A few of these outliers are also well-sampled regions
18 with a low $SE(\delta L2L_l)$; which means a more source specific study could be worthwhile.
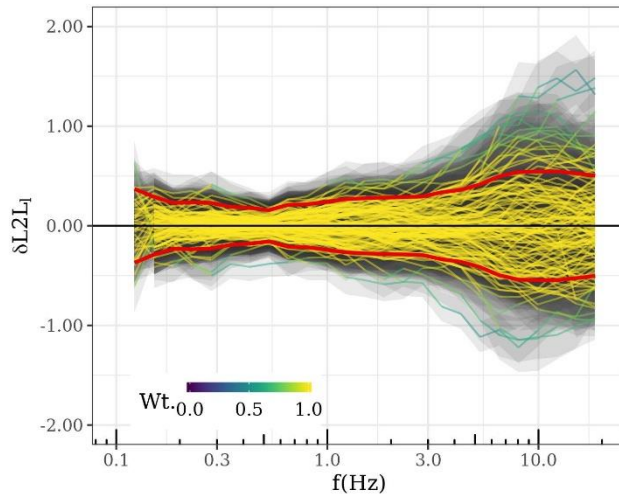
19

2-8

Figure 2-8: $\delta L2L_l$ for $f = 0.1 - 20 Hz$. Each line corresponds to one of the 134 area sources, with colors indicating their weight in robust regression. Overlain red curves mark the $\pm\tau_{L2L}$ values. Area sources with $\delta L2L_l(f)$ beyond $\pm 1.345\tau_{L2L}(f)$ are given a lower weight than one

1

2 Figure 2-9 maps the various areas sources (indexed l) color coded to their $\delta L2L_l(f = 0.3,1,3,10Hz)$
3 values. The colors in panel corresponding to $f = 0.3, 1Hz$ (in the top row) are fainter compared to those
4 of $f = 3, 10Hz$ (bottom right and left, respectively); indicating the greater diversity in ground-motion and
5 the larger τ_{L2L} in Figure 2-3. In the bottom-left panel, corresponding to $\delta L2L_l(f = 10Hz)$, a clear
6 difference between central Italy and western Anatolia can be seen. Apparently, earthquakes located in
7 central Apennine region produce substantially lower high frequency ground-motions than those in
8 northwestern Anatolia. Similarly, there is an apparent distinction between the central Apennines and Po-
9 plain earthquakes. The central Apennines area source (SERA ID: "ITAS308") contains the recent M6.5
10 Norcia earthquake and associated shocks (2016), and several well-known earthquakes in that region.
11 The Po-plain area source (SERA ID: "SIAS193") contains data from the substantially stronger M6.45
12 Friuli earthquake and a few recent earthquakes. At a first glance, Figure 2-9 it may appear as if the
13 spatial patterns are due to the predominant focal mechanisms in the regions, but the diversity of focal
14 mechanisms within each region (especially among smaller events) dissuades this hypothesis.
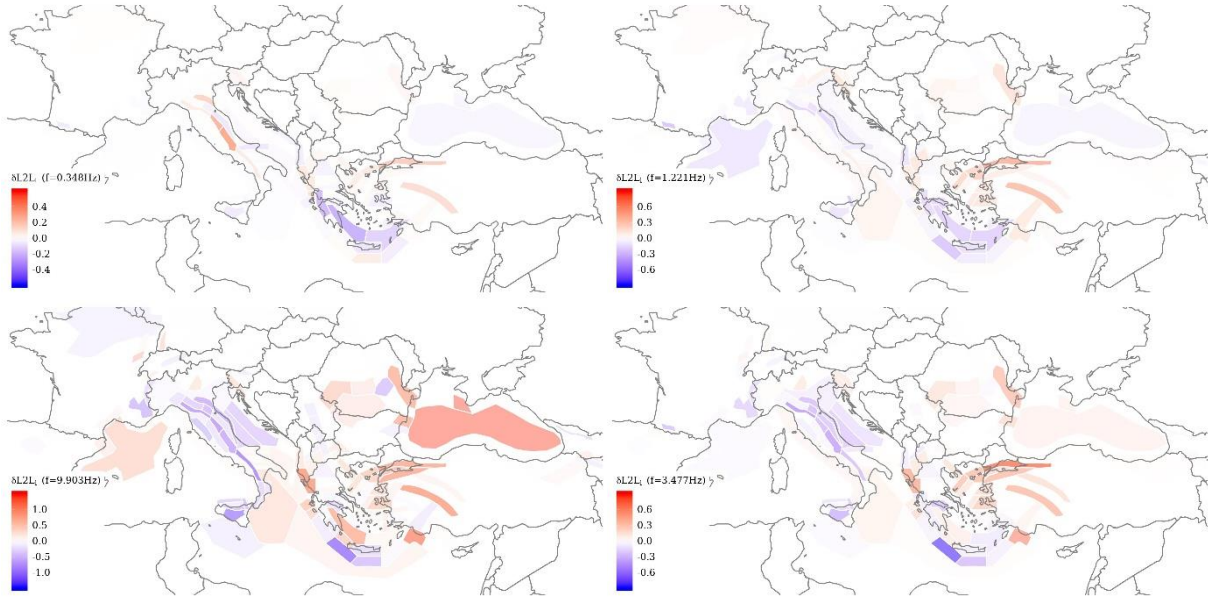
1

Figure 2-9: SERA area sources and the $\delta L2L_l$ for these region polygons, where red colored regions produced events capable of higher $GM(f = 0.3,1,3,10Hz)$ than the GMM median predictions, and blue colored regions produced earthquakes weaker than dataset average. Note that the color scale ranges are frequency dependent.

2 It is important to note that the color scale ranges in Figure 2-9 are frequency dependent. The $f = 0.3Hz$
3 map spans colors over a small range of $\delta L2L_l \in [0.6, -0.6]$, while the $f = 10Hz$ map colors span a larger
4 range of $\delta L2L_l \in [1.5, -1.5]$. Despite, an interesting feature in Figure 2-9, while comparing the maps
5 for $f = 0.3Hz$ and $f = 10Hz$, is the inversion of $\delta L2L_l$ in the central Apennines from positive to negative
6 values (red to blue). It is however inconclusive, if the events in this region produced low frequency
7 ground-motions stronger than pan-European average or if it is the inhomogeneity of M_W estimates
8 across the pan-European region.

9 ***Stress-Drop***

10 A spectral decomposition of ESM dataset into source, propagation, and site-effects, accounting as well
11 the regional differences in attenuation was performed in parallel to the GMM development (Bindi and
12 Kotha, 2020). The propagation and source components of the model were parametrized in terms of
13 geometrical spreading, quality factor, seismic moment, and corner frequency, assuming an ω^2 source
14 model (Brune, 1970). By constraining seismic moment with provided EMEC magnitudes in the dataset,
15 we estimated the Brune stress-drop for 1372 events in the dataset. It is interesting to notice that the
16 ESM event stress-drops vary from $0.2 - 20MPa$, which is a factor of 100. In order to evaluate the
17 physical meaning of source variability random-effects, we compare the $\delta B_{e,l}^0$ and $\delta L2L_l$ to the static
18 stress-drop estimates of the events in the dataset.

19 Figure 2-10 shows the relationship of $\delta B_{e,l}^0$ (left column) and $\delta L2L_l$ (right column) at $f = 0.3,1,3,10Hz$
20 (top to bottom rows) with the Brune stress-drop. The weighted loess fits (red curves) use the rlmm
21 weights assigned to the events and area sources during the GMM regression. In the right column,
22 showing $\delta L2L_l$ versus stress-drop, each marker corresponds to an event. In doing so, the variability of
23 stress-drop within an area source (l) is visualized as an array of markers (along horizontal axis) for its
24 $\delta L2L_l$ value (on the vertical axis); and the area sources with more data control the loess fits. At
25 frequencies below the corner frequency of earthquake source spectra, such as the $f = 0.3Hz$, stress-
26 drop has limited influence on the observed ground-motions. Therefore, the correlation between $\delta L2L_l$

and stress-drop is rather poor. Moving towards $f = 1,3Hz$, we notice an improvement in loess relationship, which is reasonable because stress-drop becomes relevant and τ_{L2L} is larger than at lower frequencies (Figure 2-3). At higher frequencies, where τ_{L2L} and $\delta L2L_l$ scatter is the highest, although the loess fit shows some trend, the uncertainty (red ribbon) of the fit is large enough to disregard $\delta L2L_l$ as capturing stress-drop effect. Moreover, stress-drop has very limited impact on ground-motions at $f \geq 10Hz$. The large τ_{L2L} at $f \geq 10Hz$ is clearly not from the stress-drop variability across the regions.

The left column of Figure 2-10 shows the relationship between $\delta B_{e,l}^0$ and stress-drop of the ESM events. While at $f = 0.3Hz$ we see no clearly correlation, at moderate and high frequencies, the relationship is significantly stronger. Stress-drop is an event specific property, and has been shown to correlate quite well with $\delta B_e = \delta B_{e,l}^0 + \delta L2L_l$, using various ground-motion datasets (e.g. (Bindi et al., 2018c, Bindi et al., 2019)). Introducing stress-drop as an explanatory parameter (in the fixed-effects) improves the GMM performance, but predictability of stress-drop is yet to be studied. The motivation to introduce $\delta L2L_l$ is to capture, at least partially, the spatial variability of source properties. Although $\delta B_{e,l}^0$ retains most of the stress-drop characteristics, $\delta L2L_l$ appears to capture a weaker, average stress-drop variability across the regions.
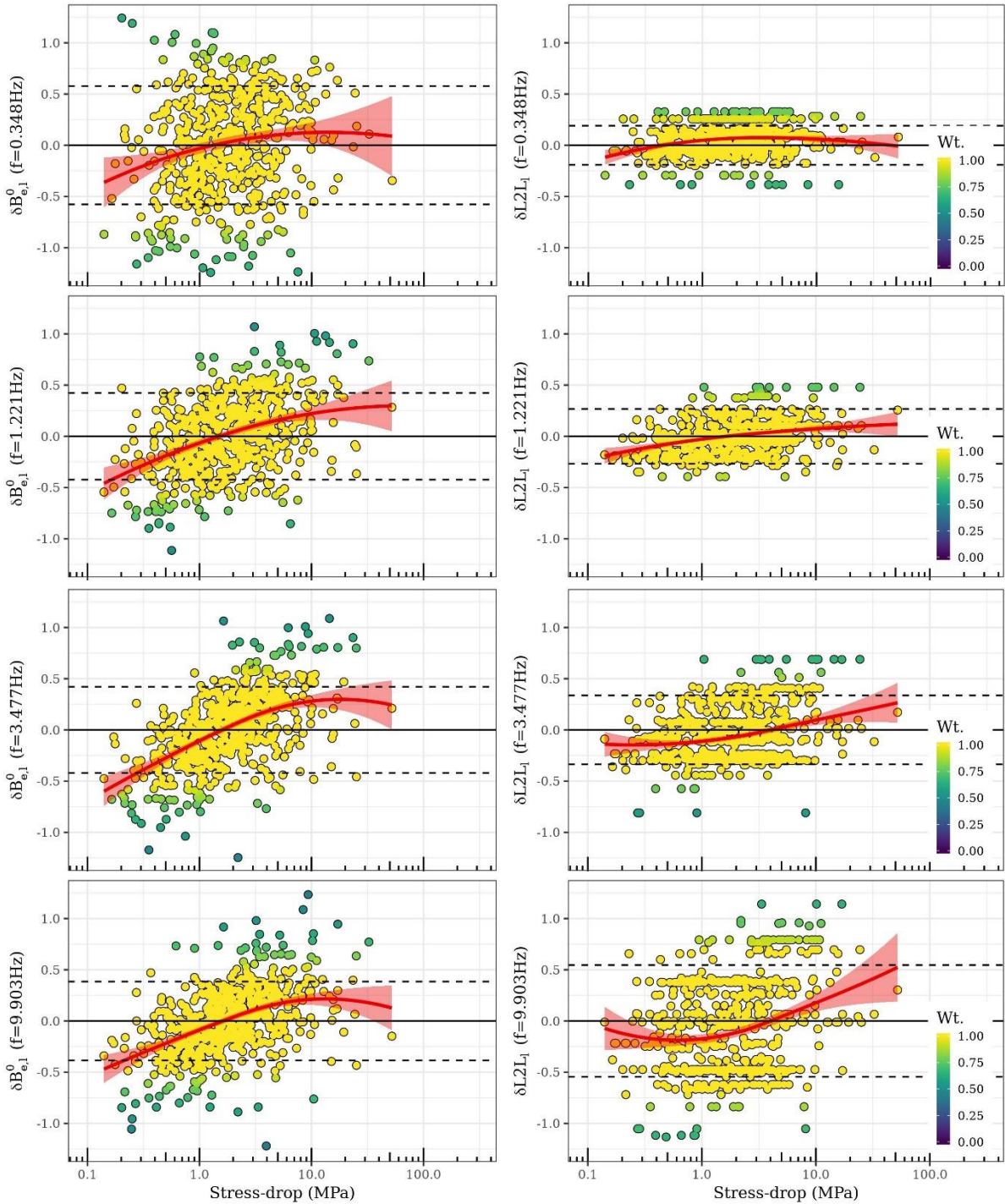
Figure 2-10: $\delta B_{e,l}^0$ and $\delta L2L_l$ relation with stress-drop for $FAS(f = 0.3, 1, 3, 10Hz)$ (top-bottom rows). The marker color indicates the weight of each event, and the two horizontal dashed lines mark $\pm\tau_0$ and $\pm\tau_{L2L}$ limits, in left and right columns respectively. The red curves are the loess fits illustrating the correlation between the quantities

1

2 ***Activity Index***

3 Following the evaluation of source random-effects with stress-drop, we check their relationship with
4 Activity Index (AI). AI is a fuzzy combination of crustal shear-wave velocity variations, 1Hz code Q, and
5 seismic moment rate density. We have already seen in Figure 2-6 the clear correlation between $\delta c_{3,r}$ and

1   the AI values at station locations. Figure 2-11 is similar in description to Figure 2-10, but instead of

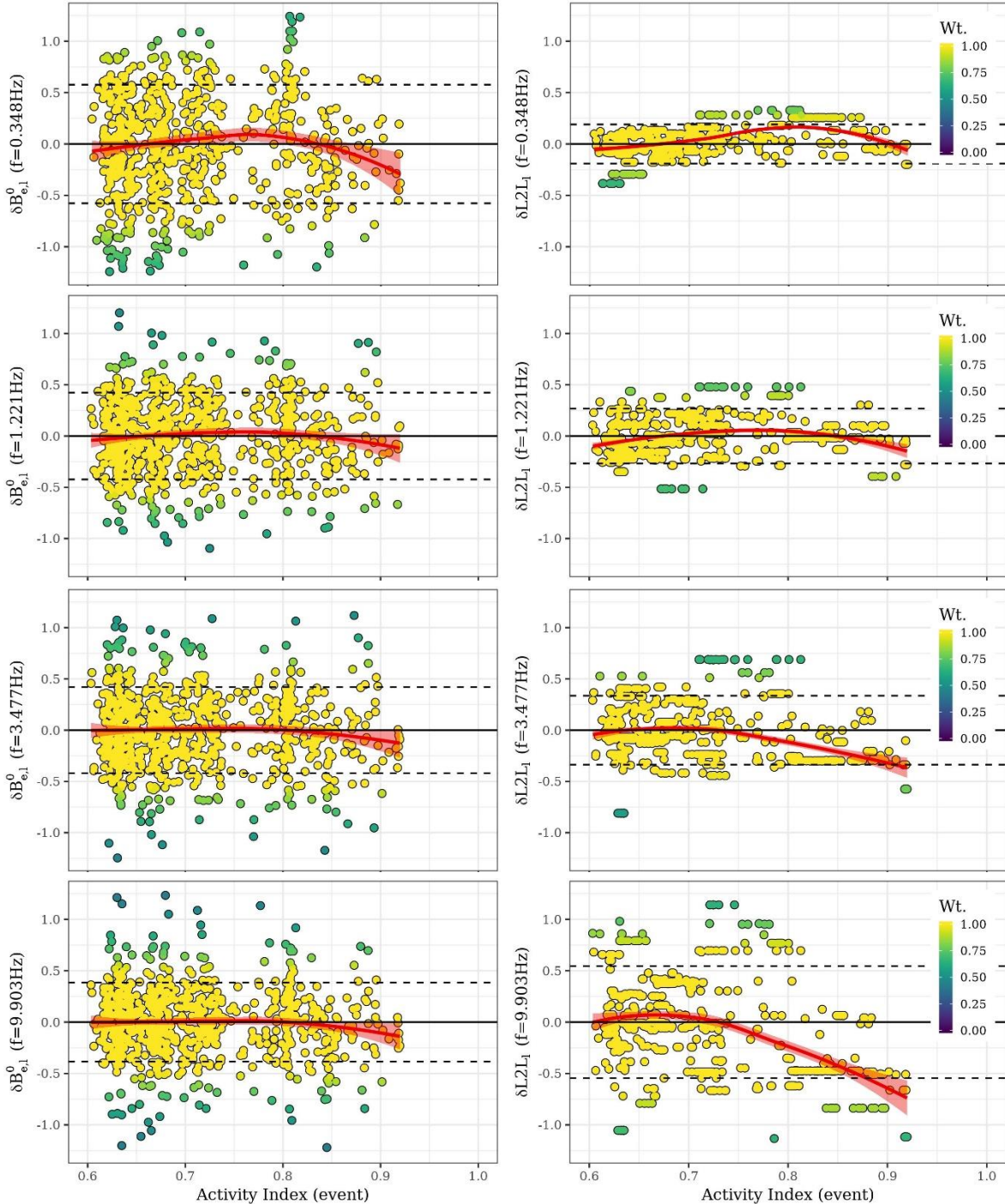2   stress-drop, we use AI at each event location.

Figure 2-11: $\delta B^0_{e,l}$ and $\delta L2L_l$ at $f = 0.3, 1, 3, 10 Hz$ (top-bottom rows) versus activity index at event location. The marker color indicates the weight of each event, and the two horizontal dashed lines mark $\pm\tau_0$ and $\pm\tau_{L2L}$ limits, in left and right columns respectively. The red curves are the loess fits illustrating the correlation between the quantities

3

4   In the right column of Figure 2-11, we see no relationship between $\delta B^0_{e,l}$ vs AI at any frequency. It means

5   to say that when $\delta B^0_{e,l}$ variability is large within an area source, the much larger areas (composed of 0.5^0

6   grid cells) with similar AI values are unlikely to resolve event-specific differences. On the other hand,

2-13

1   the size of area sources is comparable to regions with distinguishable AI values (Figure 2-1). As a result,
2   the left column of Figure 2-11 shows an interestingly strong relationship between $\delta L2L_l$ and AI (at event
3   locations).

4   Up to $f = 1Hz$, we observed no resolvable trends between $\delta L2L_l$ and AI. Moving towards higher
5   frequencies, as τ_{L2L} gains relevance, a statistically significant negative correlation is observed.
6   Essentially, the loess fits for $f \geq 2Hz$ suggest that the area sources coinciding with regions with $AI \geq$
7   0.7 are more likely to produce, on average, weaker high frequency ground-motions than those with $AI <$
8   0.7. However, since AI is a fuzzy combination of three physical parameters, it is not clear which one is
9   responsible for the negative correlation with $\delta L2L_l$.

10   A running hypothesis has been that events in stable continental regions produce stronger high frequency
11   ground-motions than those in active crustal regions, by virtue of their larger stress-drops. However, the
12   large number of $M \leq 5$ events, controlling the $\delta L2L_l$ of a region, have corner-frequencies close to $10Hz$.
13   At such high frequencies, stress-drop has limited influence on small event ground-motions. Alternatively,
14   the large τ_{L2L} value at high frequencies could be from regional variability of a high frequency source
15   parameter, e.g. the κ_{source}; which is the high frequency decay parameter of Brune's ω^2 source model
16   (Bindi et al., 2019). From a preliminary analyses, we deduce a third hypothesis from comparing the three
17   best-sampled area sources in central Italy ("ITAS308" with $\delta L2L_l = -0.6$), north Anatolia ("TRAS407"
18   with $\delta L2L_l = 0.1$), and the Aegean Sea ("GRAS369" with $\delta L2L_l = 0.8$). These three regions have similar
19   seismic moment rate density, while 1 Hz coda Q estimates are absent for the offshore Aegean Sea
20   sources. The largest differences between these three regions is the Moho depth (Grad et al., 2009) and
21   shear-wave velocity variations at 175km. These two parameters may be interconnected, and a
22   preliminary exercise did show a positive correlation between $\delta L2L_l$ and Moho depth. However, the large
23   uncertainties in Moho depths at event locations, extracted from a global model (Grad et al., 2009), are
24   not quite encouraging.

25   In summary, $\delta L2L_l$ is introduced to capture partially, in a predictable way, the spatial variability of source
26   dependent ground-motion variability. While the location corrected event-specific $\delta B_{e,l}^0$ retains a large
27   party of event-to-event stress-drop variability, $\delta L2L_l$ captures only the average regional trends. At high
28   frequencies however, $\delta L2L_l$ is more variable than $\delta B_{e,l}^0$. Given its strong correlation with Activity Index,
29   we hypothesis this parameter to be reflecting the regional differences in Moho depth or the correlated
30   crustal shear-wave velocity at depths comparable to earthquakes hypocentral depths. A further
31   exploration is therefore warranted.

32   *Site-response variability*

33   The next, and by far the largest, random variability is the site-response component $\Delta S2S_s = \mathbb{N}(0, \phi_{S2S})$.
34   Figure 2-3 shows that ϕ_{S2S} is consistently the largest random-variance at all frequencies, measured as
35   site-to-site ground-motion variability across the 1357 sites in ESM dataset. Site-specific ground-motion
36   predictions are more accurate and precise (smaller aleatory variability) than ergodic or region-specific
37   predictions, but are only possible when site-specific ground-motion data are available. In absence of
38   site-specific observations, site-response proxies are necessary to extrapolate spatially the site-specific
39   terms $\delta S2S_s$ (Kotha et al., 2018, Weatherill et al., 2019). For such studies, we disseminate a database
40   of $\delta S2S_s (f = 0.1 - 20Hz)$ derived from the ESM dataset.

41   Figure 2-12 shows the relation of $\delta S2S_s(f = 0.3, 1, 3, 10Hz)$ with measured V_{s30} (left column), and
42   topographic slope (right column). While only 281 sites are provided with measured V_{s30} in the ESM
43   dataset, topographic slope is available at all site locations. In Figure 2-12, each marker corresponds to
44   a site with an estimated $\delta S2S_s$ (irrespective of number of records), color coded to their rlmm weight. The
45   error-bars (red) illustrate the mean and MAD (median absolute deviance) within each Eurocode 8 site-
46   class. The blue curve represents the proposed linear site-response model, derived as a quadratic
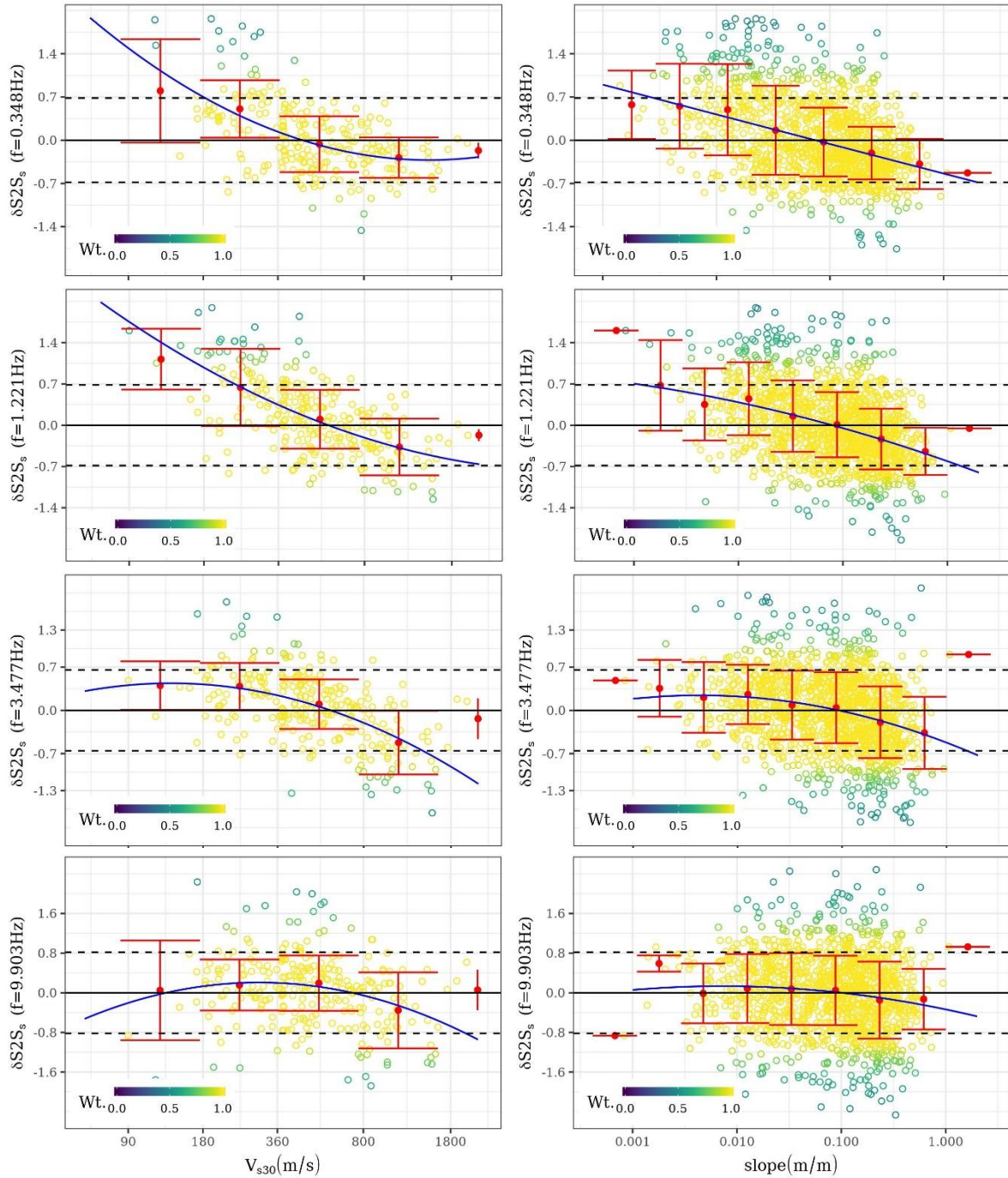47   function of V_{s30} or slope.

Figure 2-12: Plot showing the trend of $\delta S2S_s$ ($f = 0.3, 1, 3, 10 Hz$) (from top to bottom rows) with V_{s30} (left column) and topographic slope at site location (right column). Note that only 281 sites have measured V_{s30} in the ESM dataset, while all 1357 sites have topographic slope values.

1

2 Looking at the $\delta S2S_s$ trends with V_{s30}, it is evident that sites in EC8 class D ($V_{s30} \leq 180 m/s$) and class
3 C ($180 < V_{s30} \leq 360 m/s$) significantly amplify low frequency ground-motions compared to the average
4 of the dataset. In addition, the within class site-to-site variability (error-bar) is apparently larger than that
5 of EC8 class B ($360 < V_{s30} < 800 m/s$) and A ($800 m/s < V_{s30}$). The site-response of class A sites does
6 not appear to scale with V_{s30} at low frequencies. The converse is observed at high frequencies, wherein,
7 class A and B sites exhibit higher site-to-site variability, and scale steeply with V_{s30}. Interestingly, the
8 flattening of $f = 3, 10 Hz$ site-response function (blue curve) towards lower V_{s30} suggests that class C

1   and D sites exhibit high frequency amplifications lower than that a linear V_{s30} scaling would predict.
2   Although this is likely from nonlinear behavior of soft soils when subjected to strong input ground-motion,
3   a further record-to-record investigation is necessary. For now, we only provide the site-response as a
4   quadratic function of V_{s30} and slope, along with the database of site-response terms.

5   Slope is a poorer explanatory parameter of site-response than measured V_{s30}, but is relatively easier to
6   obtain at any site location. Figure 2-13 shows the reduction in ϕ_{S2S} from using V_{s30} and slope as the site-
7   response proxy. Although the reduction at lower frequencies is substantial, high frequency site-response
8   is still evasive. Given the practical importance of high frequency site-response, the most efficient solution
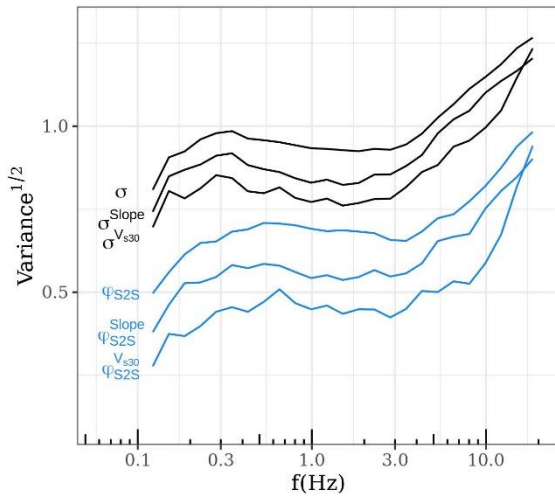9   yet is to collect more site-specific data (Bard et al., 2019).

Figure 2-13: Between-site and total variance estimates (ϕ_{S2S}, σ) of the GMM fOR T = 0.01-8s (solid lines) compared with those of K16 GMM from RESORCE DATASET (dashed lines). Reduction of (ϕ_{S2S}, σ) to $(\phi_{S2S}^{V_{s30}}, \sigma^{V_{s30}})$ using V_{s30}, and to $(\phi_{S2S}^{slope}, \sigma^{slope})$ using Slope as site-response proxies. Note that the (ϕ_{S2S}, σ) of K16 GMM are those using V_{s30} as site-response proxy, and are smaller than those shown in Figure 1-7, which are from the K16 GMM version without a site-response parameter

10

Residual analyses

12   Apart from the random-effects analyses presented in the previous section, customary checks for
13   magnitude and distance dependencies showed no peculiarities. In this section, we present the analyses
14   of the last part of the GMM: the residuals $\varepsilon = \aleph(0, \phi)$. These residuals are considered aleatoric, but may
15   contain evidences of some secondary phenomenon. Based on the residual analysis the next generation
16   of GMMs can be improved with better parametrization.

Anisotropic attenuation

18   Recent studies have shown that near-source ground-motion observations are anisotropic, as opposed
19   to the isotropic predictions of a GMM. Numerical simulations have often shown that the shear-wave
20   radiation pattern dominates the anisotropy of near-source ground-motions (Dujardin et al., 2018). In
21   accordance, ground-motion residuals of an isotropic GMM also contain the shear-wave radiation pattern
22   (Kotha et al., 2019a). An empirical shear-wave radiation pattern model developed from these residuals
23   can be used to enhance the isotropic GMM to make anisotropic ground-motion predictions. We first
24   explore the azimuthal dependence of residuals.

25   In Figure 2-14, we plot the GMM residuals against azimuth, where the azimuth is the bearing of recording
26   site with respect to rupture's striking direction. The residuals are grouped based on the style-of-faulting
27   of the event rupture and distance from epicenter. Consequently, the observed are trends are the
28   averages over the ESM's wide magnitude and distance ranges. In lieu of a more thorough frequency
29   and distance dependence analyses (Takemura et al., 2016, Kotha et al., 2019a), we present only the
30   empirical azimuth dependent trends in the GMM residuals. Figure 2-14 shows the residual trends with
31   azimuth at $f = 0.1, 1Hz$ at $R < 80km$ and $R \geq 80km$ for the strike-slip, normal-fault, and thrust-fault
32   ruptures. The trends are visualized by the loess fits between azimuth and the residuals, ignoring the
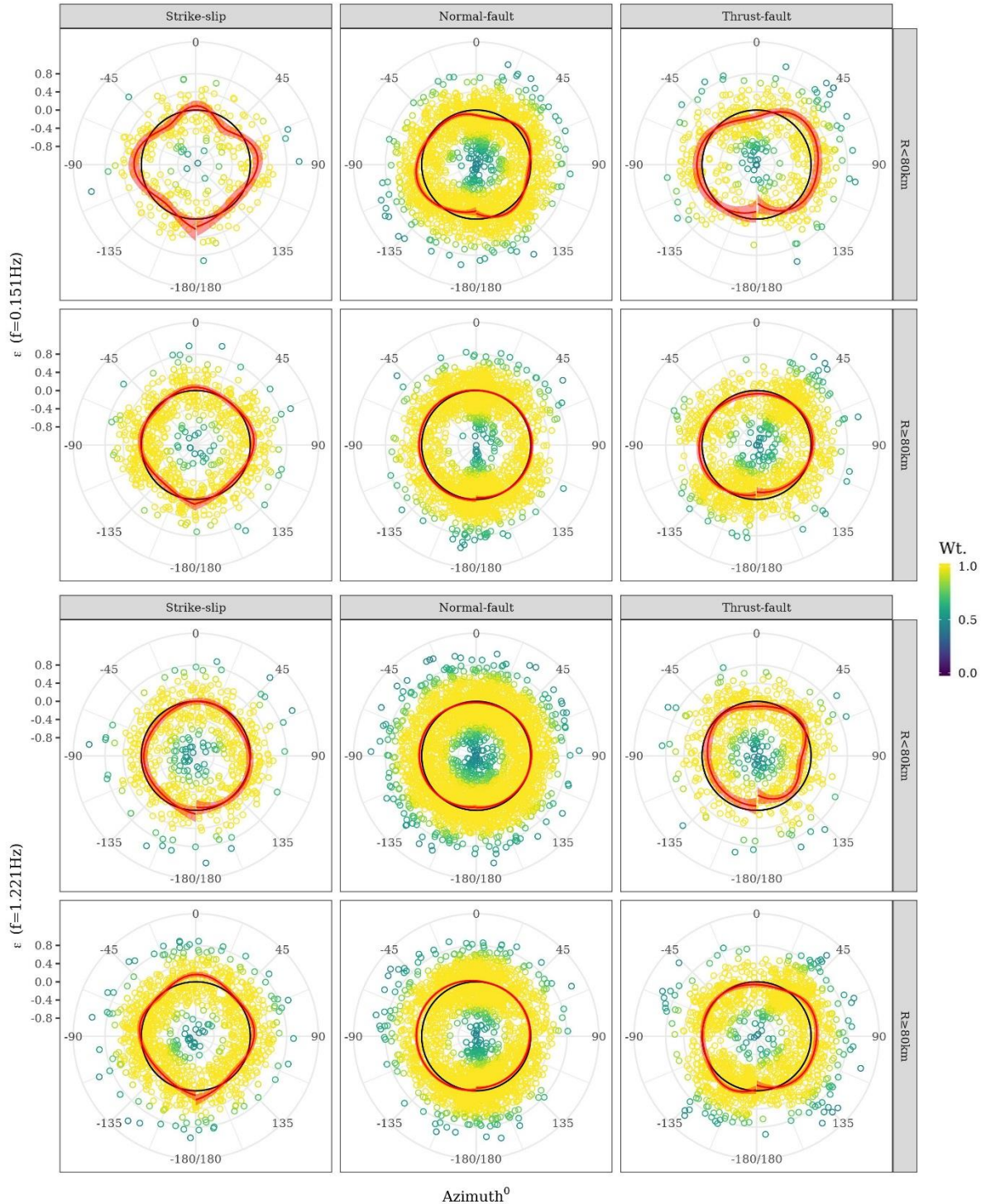33   rlmm weights.

Figure 2-14: Azimuthal dependence of residuals showing anisotropy of ground-motion observations. Red curve is the loess fit between azimuth and the residuals.

1

2   The lowest frequency at which we could regress the GMM was $f = 0.151Hz$ (top rows of Figure 2-14).
3   At this frequency, the 435 residuals from records at $R < 80km$ of the 73 strike-slip event show a clear
4   anisotropy, the four-lobbed pattern of which resembles the theoretical shear-wave radiation pattern. For
5   a vertical strike-slip rupture the theorized anisotropy (at surface) is primarily from SH body waves, and
6   partly from the SV body waves. The positive deviations of the loess fit from the zero-baseline (black
7   circle) suggests that the ground-motions along the strike ($0^0, \pm180^0$) and strike perpendicular directions

2-17

1   ($\pm 90^0$) are approx. 20% larger than the isotropic GMM predictions. Similarly, at the intermediate
2   azimuths ($\pm 45^0, \pm 135^0$) the observed ground-motions are ~20% lower than isotropic predictions. This
3   indicates the anisotropy is more likely from the SH body wave radiation pattern. In a previous study with
4   Japanese data (Kotha et al., 2019a), similar deviations were reported at $R < 80km$. But at larger
5   distances of $R \geq 80km$, the Japanese KiK-net data (Dawood et al., 2016, Kotha et al., 2018) showed
6   stronger anisotropy than the ESM data. A better quantitative evaluation would be to estimate the
7   frequency and distance dependent cross-correlation (Takemura et al., 2016) of theoretical SH and SV
8   body wave radiation coefficients (Aki and Richards, 2002) and the empirical residuals. However, this will
9   require a reliable hypocentral depth and a regionally varying crustal velocity model to estimate the take-
10 off angles. Nevertheless, it appears that the anisotropy of strike-slip residuals, resembling SH body wave
11 radiation pattern, vanishes at higher frequencies, e.g. at $f \geq 1Hz$.

12 Dip-slip events (normal and thrust mechanisms) are shown separately because the shear-wave
13 radiation pattern manifests differently on the surface compared to that from strike-slip ruptures. For
14 instance, unlike the clear four-lobed SH body wave radiation pattern of strike-slip events, dip-slip events'
15 anisotropy is a combination of predominantly the SV and less clearly the SH body waves. The variety of
16 dip and rake angle combinations of the ESM events further complicates our qualitative (visual only)
17 inspection. At low frequencies, both the normal and thrust-fault residuals have similar anisotropic
18 pattern at $R < 80km$. The pattern appears to be a combination from SV and SH body waves; according
19 to which, large ground-motions from SH body waves are to be expected at azimuths $\pm 45^0$ and $\pm 135^0$,
20 and even larger from SV body waves at azimuths $\pm 90^0$. In conjunction, ground-motions weaker than
21 isotropic predictions i.e. negative residuals, appear at azimuths 0^0 and $\pm 180^0$.

22 Our preliminary analyses suggest that shear-wave radiation pattern persists in the residuals. We
23 hypothesis that the SH body waves are responsible for the anisotropy strike-slip residuals. While a
24 combination of SV and SH body waves, dominated by the former, is likely controlling the anisotropy dip-
25 slip residuals. A more convincing evaluation would be to estimate frequency and distance dependent
26 cross-correlation of residuals with SV and SH radiation coefficients. Meanwhile, we provide the azimuth
27 dependent correction factors estimated from the loess fits.

28 *SmS reflections*

29 In the previous section, near-source residuals ($R < 80km$) were found to contain azimuthal anisotropy
30 resembling the theoretical shear-wave radiation pattern. Customary checks plotting all residuals
31 against R_{JB} showed no biases or trends. However, non-parametric analyses showed that deeper events
32 produced lower epicentral ground-motions, which decay very gradually up to 30kms; while shallower
33 events had higher epicentral ground-motions, which decayed more rapidly in the near-source distance
34 (Derras et al., 2012). Based on this we introduced event depth dependent near-source attenuation in
35 our GMM through a depth dependent h-parameter h_D. Therefore, we present the depth dependent
36 trends of ε with R_{JB} in Figure 2-15, wherein the residuals ε are classified by their event depth-bins $D <$
37 $10km, 10 \leq D < 20km,$ and $20km \leq D$, at $f = 0.3, 2, 10Hz$. Local trends between ε and R_{JB} are
38 visualized with the loess (unweighted) fits.

39 The depth dependent ε trends with R_{JB} vary with frequency. In frequency range $2 \leq f \leq 5Hz$, we
40 observe no significant trends with R_{JB}. Meaning, although the loess fit is slightly *wiggly*, the uncertainties
41 are large enough for them to be ignored. At lower frequencies such as $f < 2Hz$ however, the undulations
42 become much stronger. In the panel $f = 0.3Hz$ of Figure 2-15, while shallow $D < 10km$ residuals are
43 perfectly aligned with the zero-baseline, the $10 \leq D < 20km$ residuals tend upwards at epicentral
44 distances. There are residuals from 24 recordings that pull the trend upwards: all from 13 small-
45 moderate magnitude dip-slip events, originating in Italy, recorded in the azimuth where strong radiation
46 pattern effects can be expected. However, the centroid-moment-tensor solutions are available only for
47 six of these events. It is likely that the anisotropy of SV body waves is contributing to the bias in near-

1   source distances. The same explanation may not hold for the strong negative trends observed in the
2   high frequency $f > 5Hz$ residuals of shallow $D < 10km$ events. Upon inspection, the majority of the
3   largely negative residuals are from the $M \geq 5.5$ events, especially the M6.5 Norcia earthquake (2016),
4   whose R_{JB} is much smaller than the epicentral distance. The downward trend could be attributed to our
5   consideration of R_{JB} as the preferred distance metric (instead of R_{epi} or R_{hypo}), and depth to top-of-
6   rupture (z_{tor}) as the event depth (D) for large magnitude events, wherever available.
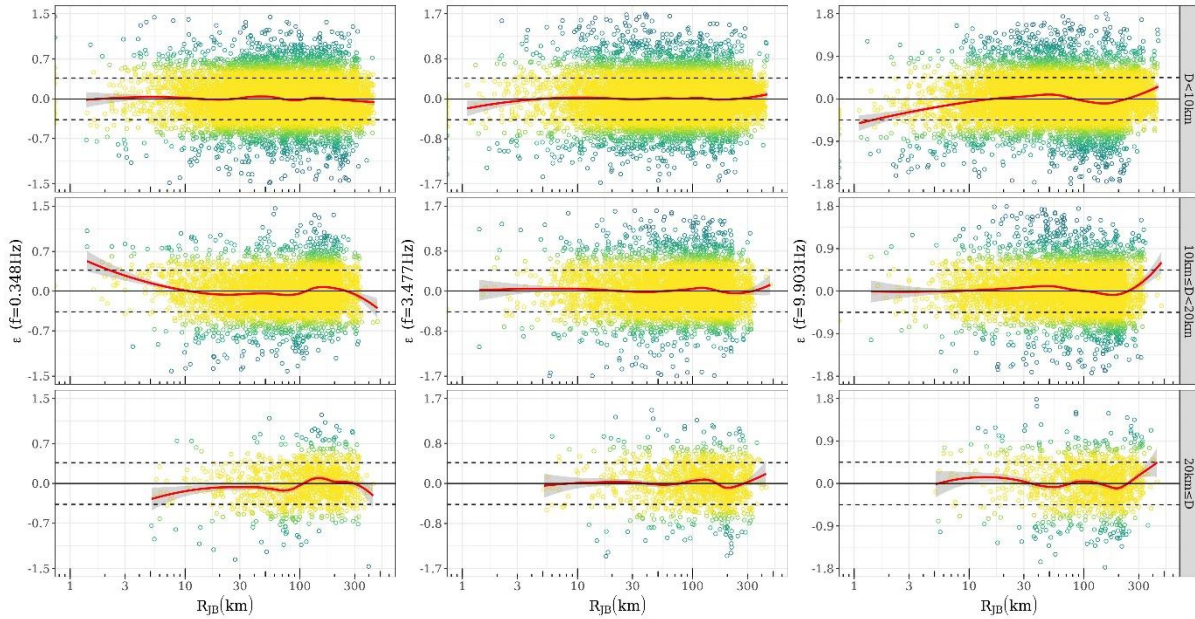
Figure 2-15: Aleatoric residual trends with distance for different event depths ($D < 10km, 10km \leq D < 20km, 20km \leq D$) for $f = 0.3, 2, 10Hz$.

7

8   In almost all panels of Figure 2-15, in the $60km < R \leq 200km$ range we observe a *bump* in the residual
9   trends, characteristic of Moho reflections (Bindi et al., 2006). These bumps become more pronounced
10   at lower frequencies and deeper earthquakes. The GMM functional form we chose is not formulated to
11   accommodate these complex secondary arrivals for two reasons. Firstly, the estimates of event
12   hypocentral depth and the depth to Moho interface at event location, which together control the
13   appearance of secondary arrivals, are both highly uncertain. Second, the inclination or declination of
14   Moho interface towards the receiving site causes dispersion or convergence of Moho reflections, leading
15   to higher or lower than expected ground-motions, respectively.

16   A few studies have emphasized the importance of SmS reflections in ground-motion prediction, hazard,
17   and risk assessments. A few examples of strong ground-motion amplifications of up to 10 times
18   observed at 100km distance at: 1) along the San Francisco Peninsula during the 1989 Loma Prieta
19   earthquake (Somerville and Yoshimura, 1990, Catchings and Kohler, 1996), 2) in the Mojave desert
20   from 28th June 1992, $M_W = 7.3$ Landers earthquake (Campbell and Bozorgnia, 1994, Mori and
21   Helmberger, 1996), 3) in the Sea of Marmara from 17th August 1999, $Mw = 7.4$, Kocaeli earthquake
22   (Boztepe-Güney and Horasan, 2002), 4) in the Taipei basin from the March 31st 2002, $M_W = 7.0$
23   Hualien offshore earthquake. Given the steep gradient of Moho in parts of the pan-European region and
24   the populated sedimentary basins (e.g. the Po-plain basin in North Italy), we consider modelling Moho
25   reflections into prospective GMMs quite important.

26   **Application**
27   For area sources, attenuating regions, and sites with sufficient amount of recordings the epistemic
28   uncertainty on the random-effect adjustments are negligible with respect to the random-effect and

standard deviations. Collecting more ground-motion recordings is principal in moving towards non-ergodic predictions. The benefits of resolving the ergodic assumption and progressing towards region- and site-specific in ground-motion prediction are demonstrated in Figure 2-16. In this plot, predictions for the M6.5 Norcia event of the central Italy sequence, occurred on 30th October, 2016, are compared to the response spectra recorded at three sites covered by the Italian strong motion network (Gorini et al., 2010). These sites are identified by the network code IT in the ESM dataset: 1) permanent, free-field station LSS (Leonessa) with $V_{s30} = 1091 m/s$ located 25km from the event epicenter, 2) permanent, free-field station MVB (Marsciano Monte Vibiano) with $V_{s30} = 1046 m/s$ located 65km from the event epicenter and, 3) permanent, free-field station PSC (Pescasserolis) with $V_{s30} = 1000 m/s$ located 110km from the event epicenter. The three columns in Figure 2-16 correspond to the three stations.

The event and stations are selected in order to demonstrate (Figure 2-16) the effect of moving from ergodic prediction to region- and site-specific predictions. The ergodic predictions rely on V_{s30} as site-response proxy (top row). The region-specific predictions (middle row) consider regional (Northern and central Apennines West) anelastic attenuation ($c_{3,r} = c_3 + \delta c_{3,r}$) and adjustment specific to the area source ($e_{1,f} = e_1 + \delta L2L_l$) containing the event (SERA ID: "ITAS308"). The region- and site-specific predictions (bottom row) use the site-specific adjustments $\delta S2S_s$, in addition to region-specific predictions ($e_{1,f,s} = e_1 + \delta L2L_l + \delta S2S_s$). Both the median prediction and total standard deviation (Figure 2-17) change in process, which is reflected by the colored ribbon in Figure 2-16. $\delta S2S_s$ of the three sites are estimated from 56, 36, and 44 records predominantly from small-moderate earthquakes (details in the Figure 2-16 panels). A few comments on this figure:

1. The ergodic median predictions (central line) and one $\sigma^{V_{s30}}$ interval (ribbon) are systematically above the observed response spectra at the three *rock* sites, located at near (25km), intermediate (65km), and far (110km) source distances. This is likely because the M6.5 Norcia event produced relatively weaker ground-motions compared to other large magnitude events recorded in Greece and Turkey – quantified into their respective $\delta B_{e,l}^0$ values. Since the ergodic predictions consider all event, region, site, and record variabilities as aleatoric, the $\sigma^{V_{s30}}$ (Figure 2-17) is large yet not large enough contain the M6.5 event observations within $\pm \sigma^{V_{s30}}$ boundaries.

2. Region-specific ground-motion predictions for these sites are achieved by adjusting the GMM with the $\delta c_{3,r}$ of the Northern and central Apennines (West), in which the sites are located; and the $\delta L2L_l$ of the SERA area source "ITAS308" in which the M6.5 event occurred (along with a few other prominent events and aftershocks). The epistemic uncertainties of these adjustments are relatively very small given the large number of recordings. In the middle row of Figure 2-16, we notice the observed Fourier spectra are closer to region-specific predictions than to the ergodic predictions. $\delta c_{3,r}$ and $\delta L2L_l$ of these regions are both lower than the pan-European average (which is zero), meaning the region attenuates high frequency ground-motions faster and the events on average produce weaker ground-motions than elsewhere in pan-European region.

It is interesting to note that, at short distances (site IT_LSS) the $\delta c_{3,r}$ has no effect on region-specific predictions, and the shift is mostly from $\delta L2L_l$ – and so is at intermediate distance (site IT_MVB). At far-source distances (site IT_PSC), the combined effect of $\delta c_{3,r}$ and $\delta L2L_l$ worked well to capture the observed Fourier spectra within the narrower $\pm \sigma_r^{V_{s30}}$ (Figure 2-17) range about the region-specific median.

Research and Development Program on
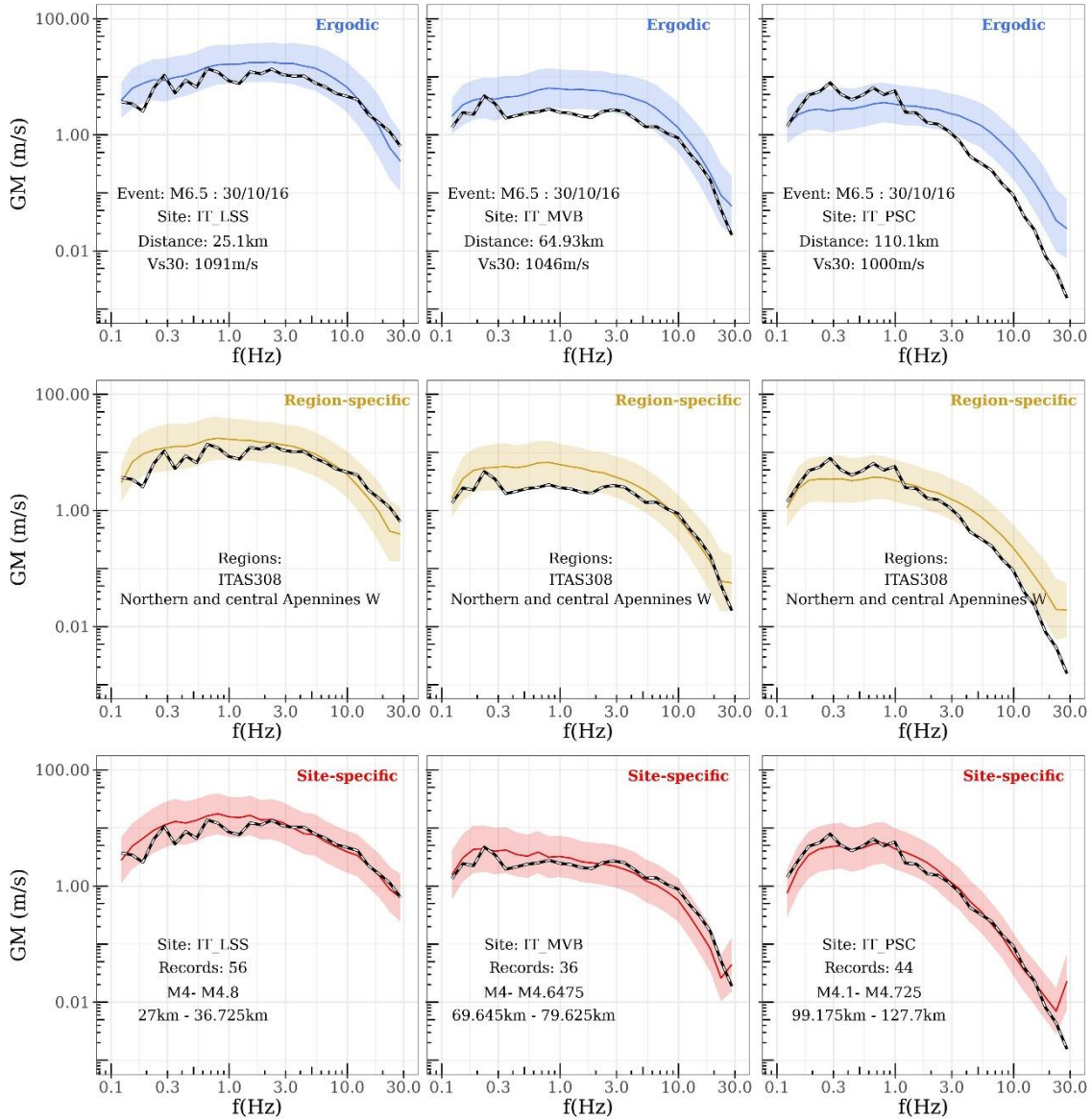Seismic Ground Motion

Figure 2-16: Comparison of ergodic (top row), region-specific (middle row), and sites-specific (bottom row) ground-motion median (solid colored line) and variability (colored ribbon) predictions for the M6.5 Norcia earthquake with the observed response spectra (solid dashed line) at three sites in Italy (column wise).

3. Region and site-specific predictions (site-specific in short) for the three sites are shown in the bottom row of Figure 2-16. Along with the curves, details on the number of recordings, magnitude and distance ranges (1st and 3rd quantile) of the recordings are provided. The additional adjustment to the preceding region-specific predictions is through $e_{1,l,s} = e_1 + \delta L2L_l + \delta S2S_s$. While most of the data in estimating the $\delta S2S_s$ of these sites is from small-moderate sized earthquakes, the site-specific predictions fit quite well with the observations for the large M6.5 event. Since $\delta S2S_s$ are used to adjust the region-specific ground-motions, the V_{s30} becomes irrelevant, while $\phi_{S2S}^{V_{s30}}$ is dropped from $\sigma_r^{V_{s30}}$ resulting in a smaller $\sigma_{r,s}$.
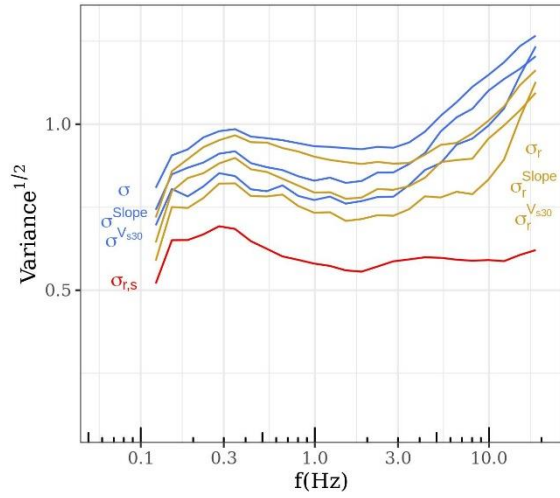
Figure 2-17: Reduction in total variance estimates (σ) of the GMM for T = 0.01-8s (solid lines) from ergodic, ergodic with site-response proxy, region-specific, and region- and site-specific values. Variance estimates when using site-response proxies are indicated by the annotations with corresponding superscript, i.e. ($\sigma^{V_{s30}}$) with V_{s30}, and to (σ^{slope}) with $Slope$. Annotations with subscript r correspond to the variances for regionalized predictions, i.e. regionalized anelastic attenuation $c_{3,r} = c_3 + \delta c_{3,r}$ and earthquake source $e_{1,f} = e_1 + \delta B_f$. Values annotated with subscript r,s correspond to region- and site-specific predictions i.e. $e_{1,f,s} = e_1 + \delta B_f + \delta B_s$ along with $c_{3,r} = c_3 + \delta c_{3,r}$ in equation (1)

1

2

Chapter 3
Region and Site-specific Adjustments for France

Introduction

The GMM models introduced in the previous chapters are those developed from relatively high seismicity regions. In order to export the GMMs to low-moderate seismicity regions, we need to estimate the various region ($\delta L2L_l$, $\delta c_{3,r}$) and site-specific ($\delta S2S_s$) random-effects for the new region. During our analyses of attributing physical meaning to the random-effects of the FAS GMM, Activity Index appeared to be the best correlated parameter to both anelastic attenuation and area source regional adjustments. Such proxy parameters, along with other geological and geotechnical parameters (Kotha et al., 2018, Weatherill et al., 2019), may allow exporting the site-specific GMMs from high to low-moderate seismicity regions. However, relying on proxies poses two issues: 1) propagation of uncertainties introduced while correlating random-effects with proxies, and 2) availability of said proxy in the region of interest. In lieu of finding the most efficient and sufficient proxies to predict region- and site-specific adjustments, we provide an alternative approach to estimating these random-effects using the recently developed ground-motion dataset (RESIF) from the French accelerometric network (Traversa et al., in-preparation).
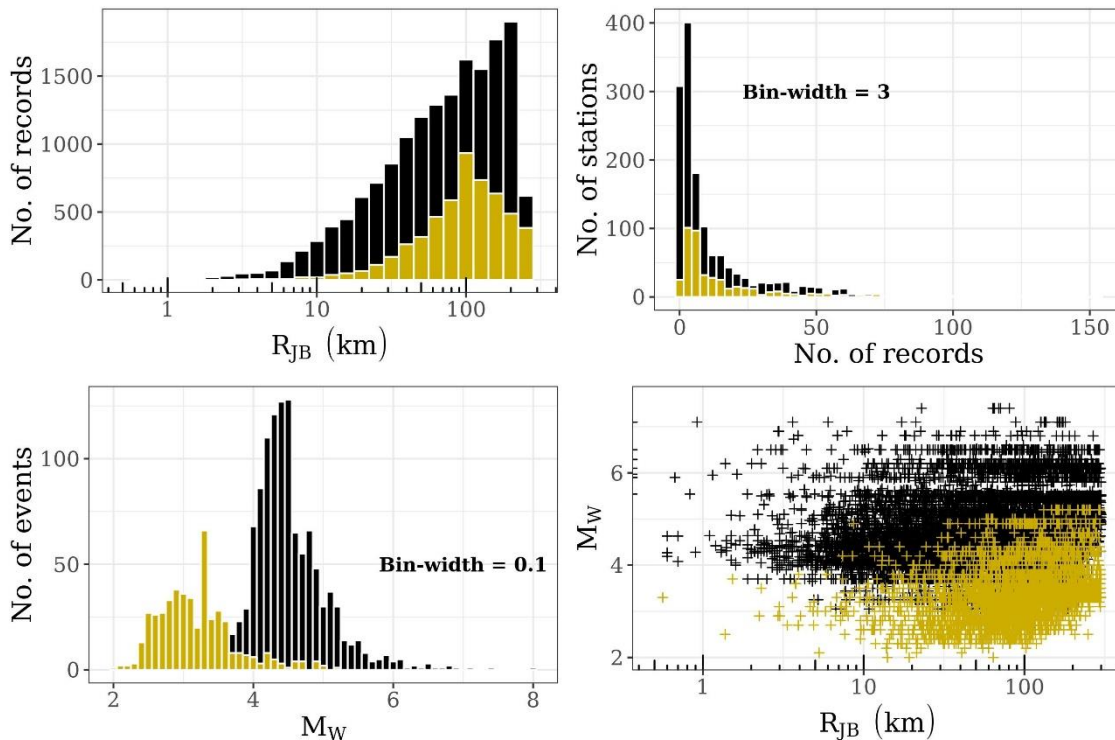

Figure 3-1: Data distribution comparing RESIF (yellow) and ESM (black) datasets

Data distribution

In moving from ergodic to region and site-specific ground-motion prediction, we require ground-motion observations at the sites in the new region, which in this case is from the RESIF dataset for France. Figure 3-1 compares the distribution of data between the ESM and RESIF datasets. The former is the dataset from which the GMMs (of previous chapters) are developed, and the latter is the dataset from

the low-moderate seismicity region. A clear difference is the distribution of event magnitudes between these two datasets. While the high seismicity region data is from relatively larger magnitude events $M3.4 - M7.1$, the RESIF dataset is constituted of smaller events with $M2 - M5.2$. Considering that small magnitude event characteristics vary strongly across fault systems, and that ground-motion scaling with M_W in the $M4.5 - M6.5$ may be different from that in $M2 - M4.5$, the magnitude scaling $f_M(M_W)$ component of the GMM (equation 4) may need to be recalibrated. In the subsequent sections, we show what and how these biases are being tackled in this exercise. Apart from the magnitude range, both datasets have comparable distance ranges and number of well-recorded sites. Using this dataset we aim to develop region and site-specific adjustments for the low-moderate seismicity region i.e. France. We note that this a preliminary analysis and will require a more thorough treatment before application to actual seismic hazard and risk assessments.

Non-parametric analyses

A preliminary non-parametric analysis performed to compare the ground-motion characteristics of the two datasets – especially in terms of scaling with M_W and R_{JB}. Such analyses provide a foresight on possible biases or trade-offs while estimating the random-effects for the regions and sites. Figure 3-2 plots the ground-motion observations from RESIF over those from ESM dataset. The RESIF data (blue) is overlain on ESM data (grey), along with the non-parametric loess fits for RESIF (orange) and ESM (black) data.
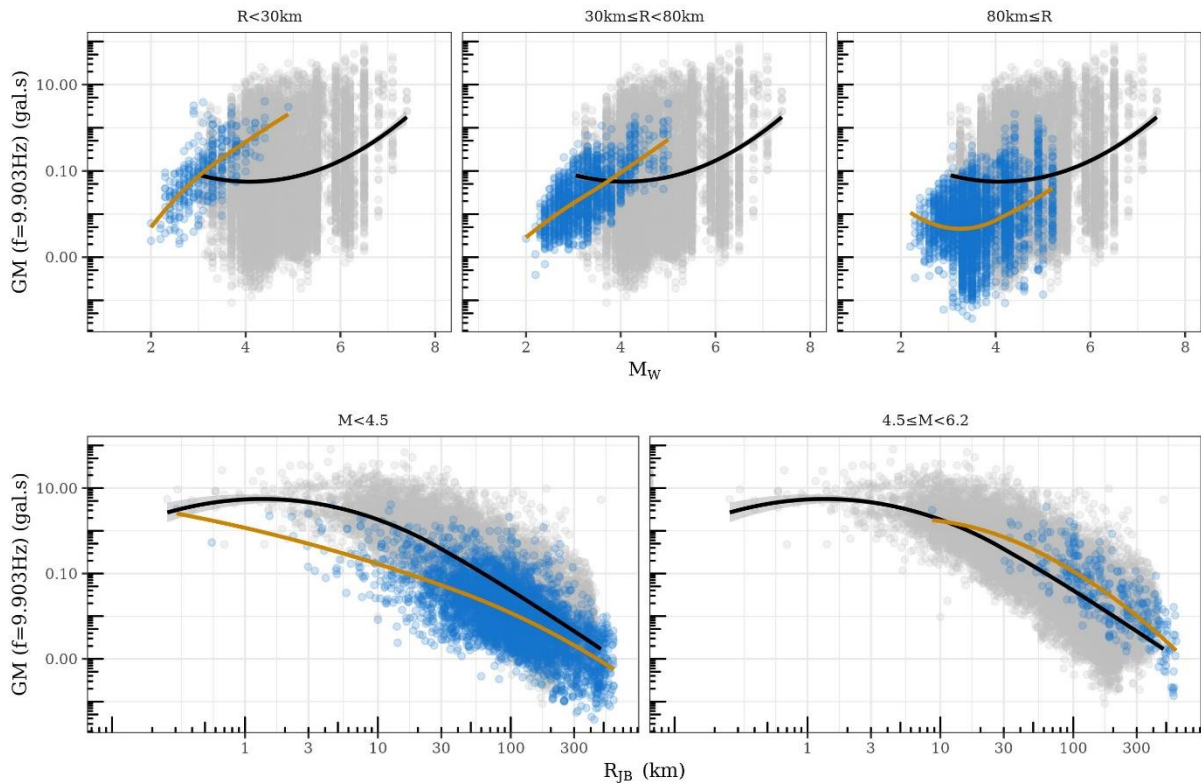

Figure 3-2: Non-parametric plots for Fourier amplitudes $GM(f = 10hz)$ vs M_W (top panels) for various distance ranges, and vs R_{JB} (Bottom panels) for various magnitude ranges. Grey markers along with black curves correspond to the ESM data and loess fits. Blue markers and orange curves correspond to those of RESIF data

The non-parametric trends indicate that there are clear differences in the ground-motion characteristics, part of which is from the difference in magnitude and distance ranges, and part from the regional

differences in earthquake source, path, and site characteristics. We note that the RESIF dataset is in preliminary stages, and the uniformity of data processing between the two datasets needs to be investigated. Therefore, the results shown here are at best preliminary.

Regionalization of RESIF data

The ESM and RESIF datasets are very likely to have several events and stations in common, especially those along the political/administrative borders of France, Italy, and Switzerland. Unlike in the RESORCE based regionalized ground-motion model (Kotha et al., 2016), where regionalization was based on national borders, the GMMs presented in this report rely on a geological and geophysical regionalization. The regionalization models used to regionalize attenuation ($\delta c_{3,r}$) and average event characteristics by location ($\delta L2L_l$) in the RESIF dataset are the same as those used in development of the ESM GMMs. In this preliminary report, we ignore the data overlaps and present only the intended approach to estimating region and site-specific adjustments from the new dataset.
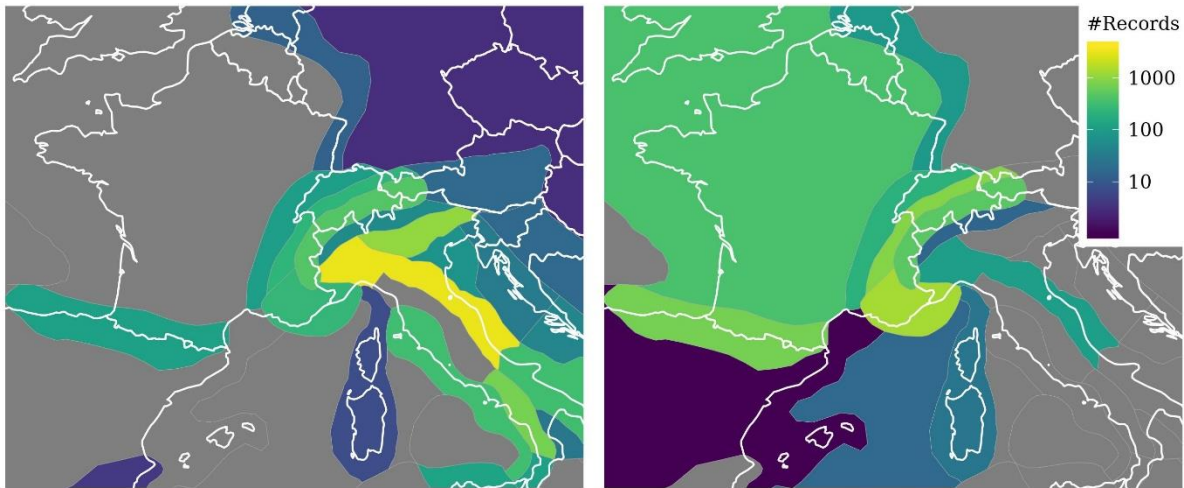

Figure 3-3: Distribution of records in each of the attenuation regionalization polygons. The left panel shows the number records in each region from ESM dataset, while the right panel corresponds to RESIF dataset

Figure 3-3 shows the distribution of number of records (based on the station location) in the attenuation region polygons, similar to Figure 1-2. The brighter colors in the left panel indicate that RESIF dataset adds several hundreds of records to the regions west of Italy's political boundaries. It is important to note that in this exercise we made no screening of common events, stations, and records between the dataset. We suspect that this could be crucial in interpreting the results, especially when comparing the estimated random-effects for regions common to both the datasets.

Mixed-effects analyses of RESIF data

We use the mixed-effects analyses to resolve the differences between the RESIF and ESM datasets that appear in the non-parametric analyses of Figure 3-2. We assume that the parametric fixed-effects of the FAS GMM (Chapter 2) is region and site independent, while the various random-effects contain the non-parametric event, region, and site-specifics. In doing so, we can first correct the RESIF observations ($\ln(Obs)_{RESIF}$) for the fixed-effects (equation 2, 3, 4), i.e. magnitude and distance scaling at each frequency, as in equation (7). The residuals (Res) contain all the differences between the RESIF data and the median predictions of the ESM GMM. Since the fixed-effects are now filtered out, the Res can be subject to random-effect analyses, as in equation (8).

$$Res = \ln(\text{Obs})_{\text{RESIF}} - \left[e_1 + f_{R,g}(M_W, R_{JB}) + f_{R,a}(R_{JB}) + f_M(M_W)\right]_{\text{ESM}} \qquad (7)$$

$$Res = offset + \delta c_{3,r}|R_{JB} + \delta L2L_l + \delta B_{e,l}^0 + \delta S2S_s + \varepsilon \qquad (8)$$

Equation (8) is the mixed-effects splitting of the residuals, and may need to be revised based on the outputs. At each frequency f, equation (8) uses the same robust linear mixed-effects regression to split the deviations Res into a bias estimate ($offset$), the event location-to-location (area source) random-effect ($\delta L2L_l$), the location corrected event random-effect ($\delta B_{e,l}^0$), the site-specific random-effect ($\delta S2S_s$), and the left-over residual (ε). While the above are scalar random-effects that do not depend on any of the explanatory parameters, $\delta c_{3,r}|R_{JB}$ is the anelastic attenuation random-effect that is R_{JB} dependent. In this sense, the effect of $offset + \delta L2L_l + \delta B_{e,l}^0 + \delta S2S_s$ is uniform over the entire distance range of predictions, whereas $\delta c_{3,r}|R_{JB}$ behaves much like the $f_{R,a}(R_{JB})$ of equation (3). Since the magnitude and distance distributions of the two datasets are quite different, this formulation of random-effect splitting may need revision. Nevertheless, in the following sections we present the outcomes of this exercise.

Results and Discussion

Following the mixed-effects analyses described above, we discuss the random-effects estimated from the two datasets in parallel. We reiterate that there are likely several common events, stations, and records between the two datasets. The random-effect estimates for levels common to both datasets may not match, and this will be investigated subsequently.

Anelastic attenuation

The regional variability of anelastic attenuation $\delta c_{3,r}$ estimated from the two datasets are shown in Figure 3-4. The regions covering the Rhine Graben, the North-Western Alps, and the Pyrenees are common to both the datasets. ESM dataset has only the events with $M_W \geq 3.5$, while the RESIF dataset is constituted mostly of $M_W \leq 3.5$. Despite the different set of records, the estimated $\delta c_{3,r}$ for the regions common to both datasets are quite similar.
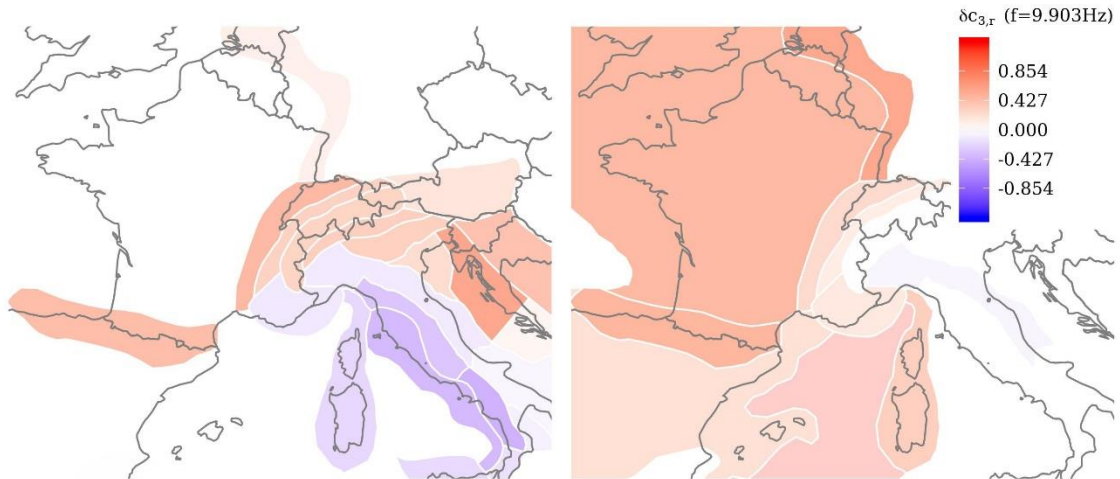

Figure 3-4: $\delta c_{3,r}$ variation across the regions estimated from RESIF (right panel) and ESM (left panel) dataset for $f = 10 Hz$. Blue polygons locate regions with anelastic attenuation faster than the pan-European average, red polygons locate regions with slower attenuation, and white polygons are regions close to the average. Regions with fewer ground-motion observations, thereby larger epistemic error on $\delta c_{3,r}$, are more transparent and appear white. Note that the color scale is limited to vary between $\pm 3 * \tau_{c3}(f)$ for each frequency f

At some frequencies, differences between the $\delta c_{3,r}$ estimated from the two datasets appear to be in Sardinia, South-Eastern France, and Central Alps, where the two datasets suggest very different characteristics. For instance, in Corsica and Sardinia, estimates from the ESM dataset suggest attenuation stronger than the pan-European average, and the contrary by RESIF dataset. However, this region is very poorly sampled in both datasets. The Central Alps region is another such mismatch; but upon inspection, ESM dataset contains recordings mostly from Swiss networks and RESIF contains only the data from stations located in France. Even though some regions are contributed equally to by both datasets, the events and stations are not the same. Based on this, we anticipate a refinement of the regionalization model and mixed-effect formulation.

Figure 3-5 shows the $\delta c_{3,r}(f = 0.1 - 20Hz)$ of the 12 regions into which the RESIF data was regionalized. The mixed-effects analyses suggests that most of these regions attenuate slower than the pan-European average, which is reasonable given that the most part of France is a low-moderate seismicity region. Even in absence of RESIF data, the relationship between AI and $\delta c_{3,r}$ shown in Figure 2-6, and the low Activity Index for France (in Figure 2-1) suggests that the predicted $\delta c_{3,r}$ would be strongly positive for these regions.
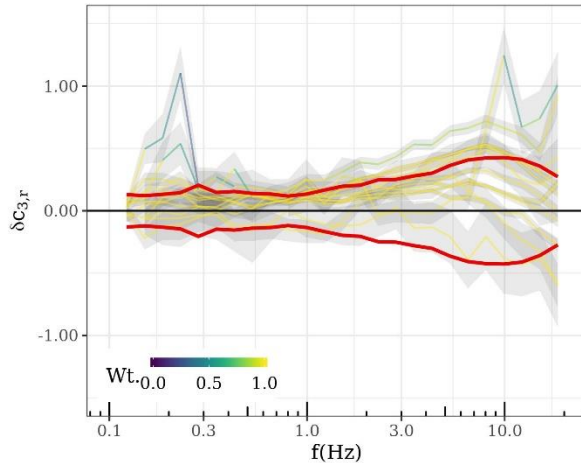

Figure 3-5: $\delta c_{3,r}$ for $f = 0.1 - 20Hz$ RESIF dataset. Each line corresponds to one of the 12 attenuation regions, with colors indicating their weight in robust regression. Overlain red curves mark the $\pm\tau_{c3}$ values. Regions with $\delta c_{3,r}(T)$ beyond $\pm1.345\tau_{c3}(T)$ are given a lower than a unit weight

Source variability

The earthquake source variability is captured by the random-effect $\delta L2L_l$. Regions, which in this case are the area sources localizing the earthquakes, with a positive $\delta L2L_l$ are those producing (on average) earthquakes stronger than the dataset median, and vice-versa for regions with negative $\delta L2L_l$. Since the two datasets have largely non-overlapping magnitude ranges, the area sources are also likely to be distinct compared to the attenuating regions (Figure 3-4).

Figure 3-6 shows the regional variability of $\delta L2L_l$ estimated from the two datasets. The left panel shows the area sources populated by earthquakes from ESM dataset, while the right panel shows those localizing the RESIF earthquakes. Of course there are regions common to both datasets; for instance, the western Mediterranean, North Western Alps (within French border), and a few area sources in the Pyrenees. The $\delta L2L_l$ estimated from RESIF and ESM datasets for these regions are similar in value, which encourages the confidence in the mixed-effect analyses.

The 28 area sources exclusive to RESIF dataset are those in the Metropolitan France, South of Pyrenees, and Rhone Alps. It appears that the earthquakes originating in the low seismicity region of Metropolitan France are on average stronger than those in the higher seismicity region of Rhone Alps. Interestingly, the relationship between $\delta L2L_l$ and Activity Index shown in Figure 2-11 would also suggest

stronger earthquakes in Western France. It is encouraging to see that Activity Index can serve a reasonable proxy to predict $\delta L2L_l$ in regions without ground-motion data.
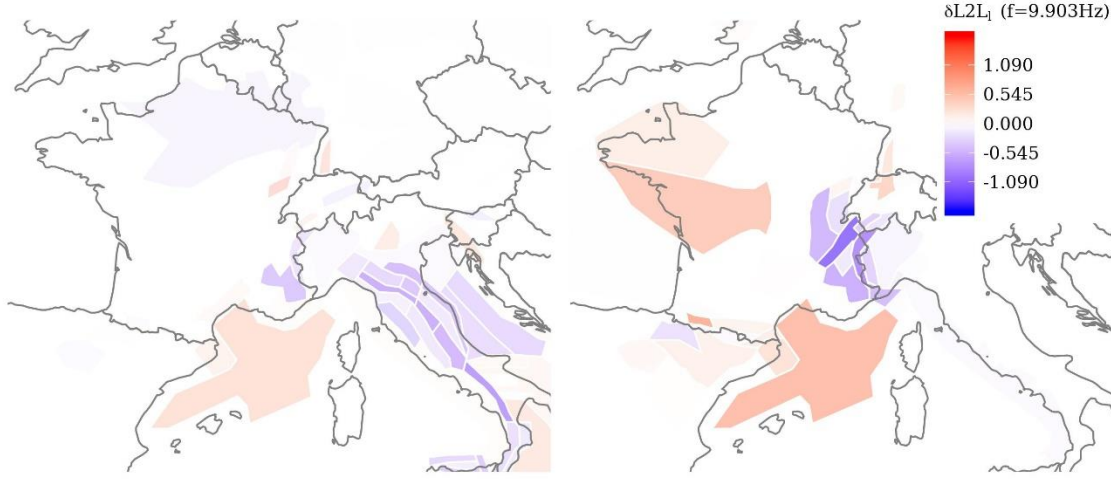

Figure 3-6: $\delta L2L_l$ variation across the regions estimated from RESIF (right panel) and ESM (left panel) dataset for $f = 10Hz$. Blue polygons locate regions producing earthquakes weaker than the pan-European average, red polygons locate regions producing on average stronger earthquakes, and white polygons are regions close to the average. Regions with fewer ground-motion observations, thereby larger epistemic error on $\delta L2L_l$, are more transparent and appear white. Note that the color scale is limited to vary between $\pm 3 * \tau_{L2L}(f)$ for each frequency f

Along with the regional variability of event characteristic captured by $\delta L2L_l$, customary checks on the region corrected event-specific random-effects $\delta B_{e,l}^0$ are shown in Figure 3-7. These plots show the trends of $\delta B_{e,l}^0$ of RESIF events (colored) with respect to M_W (left panels) and event depth D (right panels), overlain on data from ESM (grey). The bin-wise mean and MAD (center and error-bars) of the RESIF data (blue) are compared to ESM data (red). Such checks are necessary to assess if the fixed-effects part of the ESM GMM is compatible with RESIF data.

At frequencies $f = 1, 10Hz$,$\delta B_{e,l}^0$ shows no remarkable trends or biases with event depth D in either datasets. However, $\delta B_{e,l}^0$ vs M_W does reveal peculiarity of the RESIF events. At low-moderate frequencies these trends are not significant, but at high frequencies there is a clear dependence of $\delta B_{e,l}^0$ and M_W. For instance, the RESIF events with $M_W \leq 3$ have a $\delta B_{e,l}^0$ decreasing towards lower M_W, which is possible from 1) magnitude dependence of stress-drop and/or 2) the incompatibility of $f_M(M_W)$ of the ESM GMM with the RESIF events. Stress-drop estimates for the RESIF events are not yet available. Hence, it is not possible yet to distinguish the actual cause of misfit.

There are 18 RESIF earthquakes with $M_w \geq 4$ whose $\delta B_{e,l}^0$ is larger than the τ_0 at $f = 10Hz$. Meaning, these 18 earthquakes produced substantially larger high frequency ground-motions than the ESM events of similar magnitudes. However, it is too early to comment on these events without a detailed look at their source spectra.
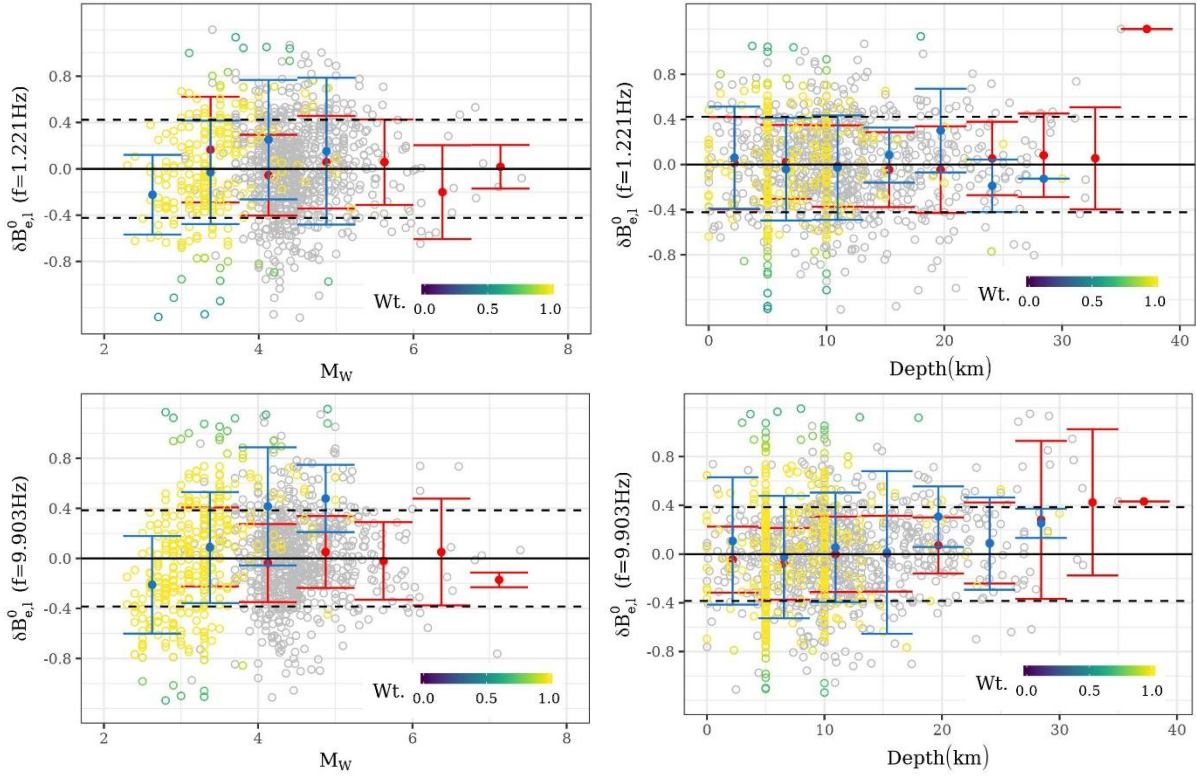
Research and Development Program on
Seismic Ground Motion

Figure 3-7: $\delta B_{e,l}^0$ versus M_W (left column) and depth (right column) for three periods $T = 0s, 0.1s, 1s$. Data from ESM is in grey, while that from RESIF is color coded according to their rlmm weights. The mean (red for ESM, blue for RESIF) and median absolute deviance (red error-bars for ESM and blue error-bars for RESIF) of $\delta B_{e,l}^0$ within the bins of size $0.5 M_W$ and $5km$. The two horizontal lines mark the $\pm \tau_0$ for the two frequencies

Site-response variability

Site-response variability is the biggest contributor to the overall ground-motion variability in both RESIF and the ESM datasets. We intended to estimate the site-specific random-effects $\delta S2S_s$ for as many sites as possible, so that site-specific predictions would be possible. Figure 1-16 and Figure 2-16 show that site-specific ground-motion predictions are the closest match to the observations at a site, in both response spectra and Fourier domain. A very interesting aspect of Figure 1-16 and Figure 2-16 is that, while the $\delta S2S_s$ for the three selected sites (in Italy) are estimated from recordings of $M4 - M5$ events, the predicted response and Fourier spectra of the large $M6.5$ earthquake are almost a perfect match with the observations. 10-fold cross-validation exercise presented in Figure 1-17 also confirms that the site-specific GMMs have the least RMSE, and hence, the best predictive performance. Therefore, we estimate the $\delta S2S_s$ for any site with a few ground-motion recordings. Fortunately, the RESIF dataset contains around 360 sites with at least three recordings, and 180 sites with 10 or more recordings. Figure 3-8 shows the numerous additional sites in the RESIF dataset at which the site-specific terms are now available.
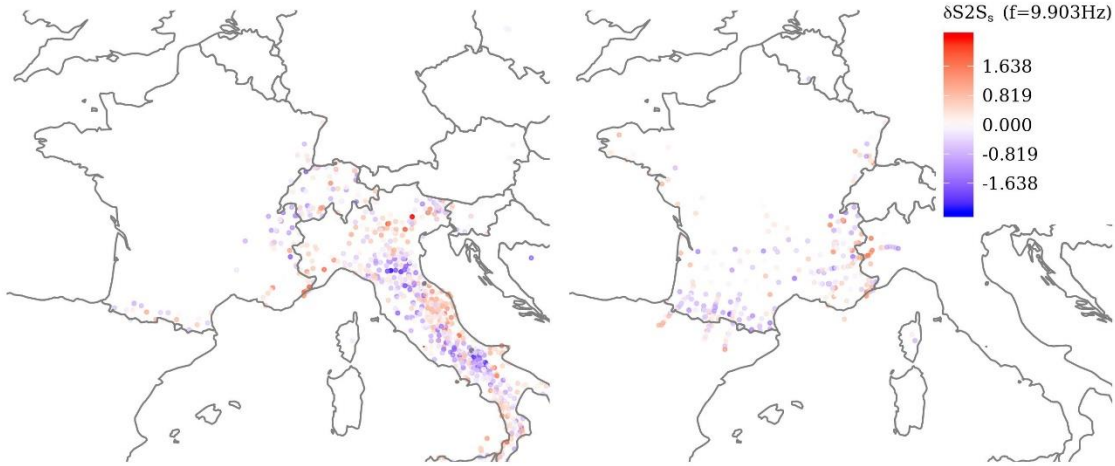
Figure 3-8: $\delta S2S_s$ of the sites in RESIF (right panel) and in ESM (left panel) datasets for $f = 10 Hz$. Blue markers locate sites attenuating the high frequency ground-motions with respect to the pan-European average, red markers locate sites amplifying the high frequency ground-motions, and white markers are sites with amplifications close to the pan-European average. Sites with fewer ground-motion observations, thereby larger epistemic error on $\delta S2S_s$, are more transparent and appear white. Note that the color scale is limited to vary between $\pm 3 * \phi_{S2S}(f)$ for each frequency f

133 out of the 360 sites in RESIF data are provided with V_{s30} measured values, as opposed to 281 out of 1340 sites in ESM. *Slope* estimates at the RESIF site locations are not available at the moment. Figure 3-9 shows the $\delta S2S_s$ versus V_{s30} of the sites. Sites from ESM are shown in grey, with mean (center) and MAD (error-bars) within each Eurocode8 soil class (based on V_{s30}) in red. Sites from RESIF are color coded with their rlmm weights, with soil class mean and MAD in blue. It is interesting that the RESIF dataset contains several sites with $V_{s30} \geq 1800 m/s$ compared to the ESM dataset.
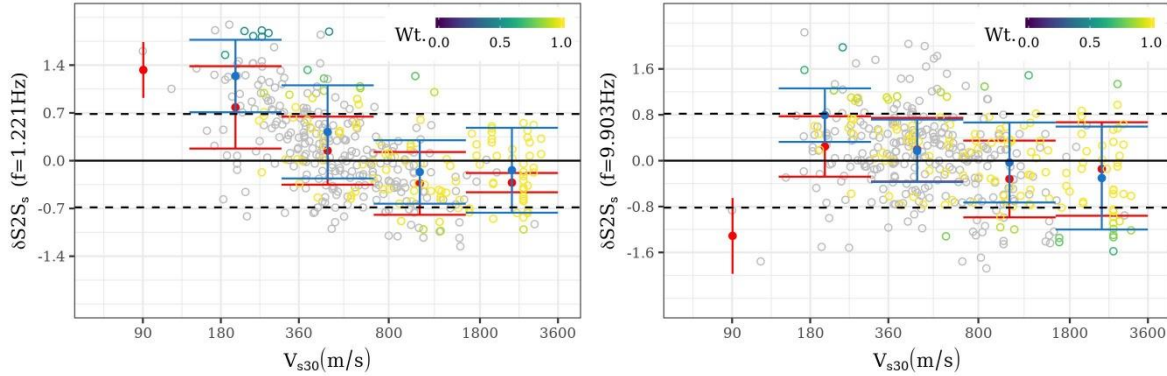

Figure 3-9: $\delta S2S_s$ versus V_{s30} at $f = 1 Hz$ (left column) and $f = 10 Hz$ (right column). Data from ESM is in grey, while that from RESIF is color coded according to their rlmm weights. The mean (red for ESM, blue for RESIF) and median absolute deviance (red error-bars for ESM and blue error-bars for RESIF) of $\delta B_{e,l}^0$ within the bins coinciding with Eurocode8 soil classification. The two horizontal lines mark the $\pm \phi_{S2S}$ for the two frequencies

In general, the trends of $\delta S2S_s$ with V_{s30} are almost identical between the two datasets. The softer soil sites with lower V_{s30} show remarkably higher amplification of low frequency ($f = 1 Hz$) ground-motions compared to the stiffer soils. Interestingly, the wide error-bars at very high $V_{s30} \geq 1800 m/s$, at both low and high frequencies, suggest that site-response of *hard-rock* sites is highly variable. In addition, the high frequency ($f = 10 Hz$) site-response shows a very poor relation with V_{s30}, for sites in both ESM and RESIF datasets.

Presence of a few negative $\delta S2S_s(f = 10Hz)$ at $V_{s30} \leq 360m/s$ may be an indication of non-linear soil response, wherein softer soils attenuate high frequency ground-motions more than stiffer soils. A site-to-site and record-to-record analysis could reveal the physics behind the negative $\delta S2S_s$ of the soft soils at high frequencies.

Residual analyses

It is of major interest to query the *left-over* residuals for azimuthal anisotropy, as with the ESM data in Figure 2-14. Since the current (preliminary) version of RESIF dataset does not provide the focal mechanisms of its events, such analysis can only be anticipated. Another interesting feature found in ESM residuals is the presence of SmS reflections, which manifest in the distance range $60 - 120km$. Figure 3-10 shows the residual ε trends with R_{JB} for the data from three depth ranges $(D < 10km, 10 \leq D < 20km, 20km \leq D)$.

The most important aspect of these plots is that at far-source distances, $R \geq 80km$, residuals from both datasets are on average close to zero-baseline, which means the regional differences in anelastic attenuation are effectively removed from the data through $\delta c_{3,r}$ – pending further refinements of course. Other than that, it is worth noting that the RESIF dataset extends up to $R = 662km$, while ESM dataset ends at $R = 471km$. We suspect ground-motion data from $M2 - M4$ events would be reliable at such long distances. Hence, we intend to review the RESIF dataset more thoroughly before finalizing the mixed-effects analysis.
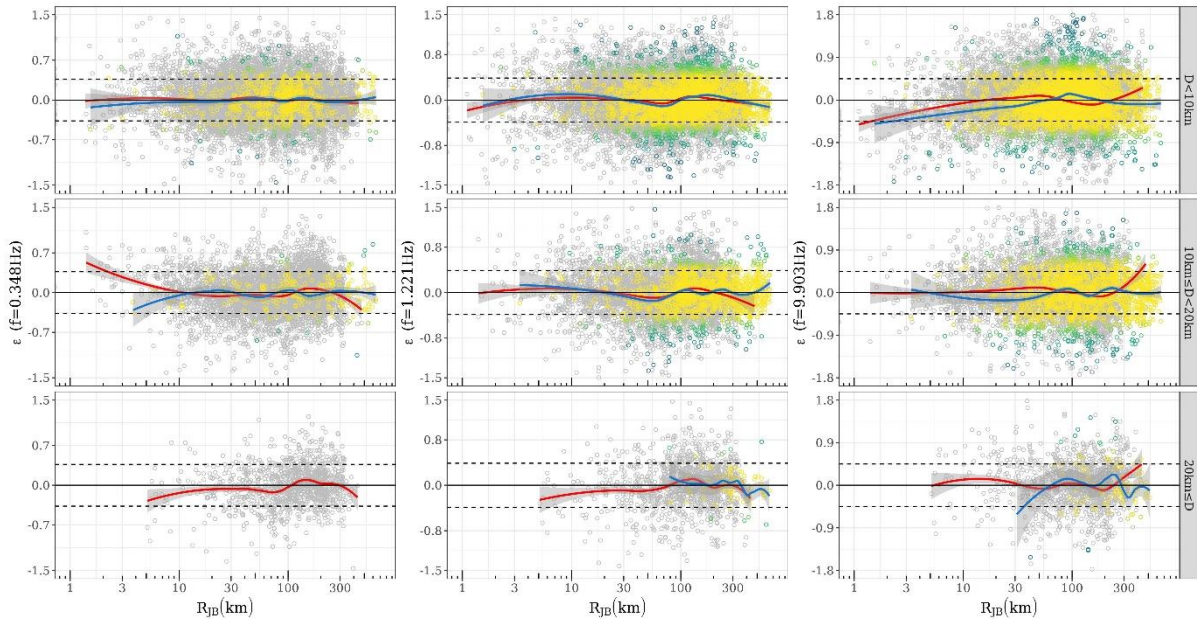

Figure 3-10: Aleatoric residual trends with distance for different event depths $(D < 10km, 10km \leq D < 20km, 20km \leq D)$ for $f = 0.3, 1, 10Hz$. The grey markers and red loess fits correspond to ESM data, while the colored markers and blue loess fits are of RESIF data.

Regarding our hypothesis on SmS reflections, the *undulated* loess fit around $R = 60 - 120km$ is possibly from the concurrent arrival of direct S-waves and Moho reflected phases at the station. The residual patterns shown here are frequency dependent, and so are the SmS reflections. Therefore, it is not straightforward modelling such complex, regionally varying phenomenon without revising the distance metric used in our GMMs. Nevertheless, if such patterns are proven indeed to be Moho reflections, a piece-wise distance scaling component (still using R_{JB} as the metric) in the GMM would be the easiest

implementation. Several studies have attributed very strong amplifications at far-source distances to Moho reflections. Therefore, it is worthwhile improving the distance scaling component of the GMMs.

Bibliography

ABRAHAMSON, N. & YOUNGS, R. 1992. A stable algorithm for regression analyses using the random effects model. *Bulletin of the Seismological Society of America,* 82**,** 505-510.

ABRAHAMSON, N. A., SILVA, W. J. & KAMAI, R. 2014. Summary of the ASK14 Ground Motion Relation for Active Crustal Regions. *Earthquake Spectra,* 30**,** 1025-1055.

AKI, K. & RICHARDS, P. G. 2002. *Quantitative seismology.*

AKKAR, S., SANDıKKAYA, M. & BOMMER, J. 2014a. Empirical ground-motion models for point-and extended-source crustal earthquake scenarios in Europe and the Middle East. *Bulletin of earthquake engineering,* 12**,** 359-387.

AKKAR, S., SANDıKKAYA, M., ŞENYURT, M., SISI, A. A., AY, B., TRAVERSA, P., DOUGLAS, J., COTTON, F., LUZI, L. & HERNANDEZ, B. 2014b. Reference database for seismic ground-motion in Europe (RESORCE). *Bulletin of earthquake engineering,* 12**,** 311-339.

AL ATIK, L., ABRAHAMSON, N., BOMMER, J. J., SCHERBAUM, F., COTTON, F. & KUEHN, N. 2010. The variability of ground-motion prediction models and its components. *Seismological Research Letters,* 81**,** 794-801.

ANCHETA, T. D., DARRAGH, R. B., STEWART, J. P., SEYHAN, E., SILVA, W. J., CHIOU, B. S.-J., WOODDELL, K. E., GRAVES, R. W., KOTTKE, A. R. & BOORE, D. M. 2014. NGA-West2 database. *Earthquake Spectra,* 30**,** 989-1005.

ANDERSON, J. G. & BRUNE, J. N. 1999. Probabilistic seismic hazard analysis without the ergodic assumption. *Seismological Research Letters,* 70, 19-28.

ATIK, L. A. & YOUNGS, R. R. 2014. Epistemic uncertainty for NGA-West2 models. *Earthquake Spectra,* 30**,** 1301-1318.

BARD, P.-Y., BORA, S. S., HOLLENDER, F., LAURENDEAU, A. & TRAVERSA, P. 2019. Are the Standard V S-Kappa Host-to-Target Adjustments the Only Way to Get Consistent Hard-Rock Ground Motion Prediction? *Pure and Applied Geophysics***,** 1-20.

BATES, D., MÄCHLER, M., BOLKER, B. & WALKER, S. 2014. Fitting linear mixed-effects models using lme4. *arXiv preprint arXiv:1406.5823.*

BINDI, D., COTTON, F., KOTHA, S. R., BOSSE, C., STROMEYER, D. & GRÜNTHAL, G. 2017. Application-driven ground motion prediction equation for seismic hazard assessments in non-cratonic moderate-seismicity areas. *Journal of Seismology,* 21**,** 1201-1218.

BINDI, D., COTTON, F., SPALLAROSSA, D., PICOZZI, M. & RIVALTA, E. 2018a. Temporal variability of ground shaking and stress drop in Central Italy: A hint for fault healing? *Bulletin of the Seismological Society of America,* 108**,** 1853-1863.

BINDI, D., KOTHA, S.-R., WEATHERILL, G., LANZANO, G., LUZI, L. & COTTON, F. 2018b. The pan-European engineering strong motion (ESM) flatfile: consistency check via residual analysis. *Bulletin of Earthquake Engineering***,** 1-20.

BINDI, D. & KOTHA, S. R. 2020. Spectral decomposition of the Engineering Strong Motion (ESM) flat file: regional attenuation, source scaling and Arias stress drop. *Bulletin of Earthquake Engineering,* in-review.

BINDI, D., MASSA, M., LUZI, L., AMERI, G., PACOR, F., PUGLIA, R. & AUGLIERA, P. 2014. Pan-European ground-motion prediction equations for the average horizontal component of PGA, PGV, and 5%-damped PSA at spectral periods up to 3.0 s using the RESORCE dataset. *Bulletin of earthquake engineering,* 12**,** 391-430.

BINDI, D., PAROLAI, S., GROSSER, H., MILKEREIT, C. & KARAKISA, S. 2006. Crustal attenuation characteristics in northwestern Turkey in the range from 1 to 10 Hz. *Bulletin of the Seismological Society of America,* 96**,** 200-214.

BINDI, D., PICOZZI, M., SPALLAROSSA, D., COTTON, F. & KOTHA, S. R. 2019. Impact of Magnitude Selection on Aleatory Variability Associated with Ground-Motion Prediction Equations: Part II— Analysis of the Between-Event Distribution in Central Italy. *Bulletin of the Seismological Society of America,* 109**,** 251-262.

BINDI, D., SPALLAROSSA, D., PICOZZI, M., SCAFIDI, D. & COTTON, F. 2018c. Impact of magnitude selection on aleatory variability associated with ground-motion prediction equations: Part I— Local, energy, and moment magnitude calibration and stress-drop variability in central Italy. *Bulletin of the Seismological Society of America,* 108**,** 1427-1442.

BOHNHOFF, M., MARTÍNEZ-GARZÓN, P., BULUT, F., STIERLE, E. & BEN-ZION, Y. 2016. Maximum earthquake magnitudes along different sections of the North Anatolian fault zone. *Tectonophysics,* 674**,** 147-165.

BOMMER, J. J., DOUGLAS, J., SCHERBAUM, F., COTTON, F., BUNGUM, H. & FÄH, D. 2010. On the selection of ground-motion prediction equations for seismic hazard analysis. *Seismological Research Letters,* 81**,** 783-793.

BOORE, D. M. 2010. Orientation-independent, nongeometric-mean measures of seismic intensity from two horizontal components of motion. *Bulletin of the Seismological Society of America,* 100**,** 1830-1835.

BOORE, D. M., STEWART, J. P., SEYHAN, E. & ATKINSON, G. M. 2014. NGA-West2 equations for predicting PGA, PGV, and 5% damped PSA for shallow crustal earthquakes. *Earthquake Spectra,* 30**,** 1057-1085.

BORA, S. S., COTTON, F., SCHERBAUM, F., EDWARDS, B. & TRAVERSA, P. 2017. Stochastic source, path and site attenuation parameters and associated variabilities for shallow crustal European earthquakes. *Bulletin of Earthquake Engineering,* 15**,** 4531-4561.

BOZTEPE-GÜNEY, A. & HORASAN, G. 2002. Enhanced ground motions due to large-amplitude critical Moho reflections (SmS) in the Sea of Marmara, Turkey. *Geophysical research letters,* 29.

BRUNE, J. N. 1970. Tectonic stress and the spectra of seismic shear waves from earthquakes. *Journal of geophysical research,* 75**,** 4997-5009.

CAMPBELL, K. W. 1981. Near-source attenuation of peak horizontal acceleration. *Bulletin of the Seismological Society of America,* 71**,** 2039-2070.

CAMPBELL, K. W. & BOZORGNIA, Y. 1994. Empirical-Analysis of Strong Ground Motion from the 1992 Landers, California, Earthquake. *Bulletin of the Seismological Society of America,* 84**,** 573-588.

CAMPBELL, K. W. & BOZORGNIA, Y. 2014. NGA-West2 Ground Motion Model for the Average Horizontal Components of PGA, PGV, and 5% Damped Linear Acceleration Response Spectra. *Earthquake Spectra,* 30**,** 1087-1115.

CATCHINGS, R. & KOHLER, W. 1996. Reflected seismic waves and their effect on strong shaking during the 1989 Loma Prieta, California, earthquake. *Bulletin of the Seismological Society of America,* 86**,** 1401-1416.

CHEN, Y.-S., WEATHERILL, G., PAGANI, M. & COTTON, F. 2018. A transparent and data-driven global tectonic regionalization model for seismic hazard assessment. *Geophysical Journal International,* 213**,** 1263-1280.

CHIOU, B. S.-J. & YOUNGS, R. R. 2014. Update of the Chiou and Youngs NGA model for the average horizontal component of peak ground motion and response spectra. *Earthquake Spectra,* 30**,** 1117-1153.

CONG, L. & MITCHELL, B. 1998. Lg coda Q and its relation to the geology and tectonics of the Middle East. *Q of the Earth: Global, Regional, and Laboratory Studies.* Springer.

CROWLEY, H., WEATHERILL, G., RIGA, E., PITILAKIS, K., ROULLÉ, A., TOURLIÈRE, B., LEMOINE, A. & HIDALGO, C. G. 2019 - in-preparation. Methods for Estimating Site Effects in Risk Assessments.

DAWOOD, H. M., RODRIGUEZ-MAREK, A., BAYLESS, J., GOULET, C. & THOMPSON, E. 2016. A Flatfile for the KiK-net Database Processed Using an Automated Protocol. *Earthquake Spectra,* 32**,** 1281-1302.

DAWOOD, H. M. & RODRIGUEZ-MAREK, A. 2013. A method for including path effects in ground-motion prediction equations: An example using the Mw 9.0 Tohoku earthquake aftershocks. *Bulletin of the Seismological Society of America,* 103**,** 1360-1372.

DERRAS, B., BARD, P. Y., COTTON, F. & BEKKOUCHE, A. 2012. Adapting the neural network approach to PGA prediction: an example based on the KiK-net data. *Bulletin of the Seismological Society of America,* 102**,** 1446-1461.

DOUGLAS, J. 2004. An investigation of analysis of variance as a tool for exploring regional differences in strong ground motions. *Journal of Seismology,* 8**,** 485-496.

DOUGLAS, J. Fifty years of ground-motion models. Second European Conference on Earthquake Engineering and Seismology (2ECEES): a joint event of the 15th European Conference on Earthquake engineering & 34th General Assembly of the European Seismological Commission, 2014.

34

DUJARDIN, A., CAUSSE, M., BERGE-THIERRY, C. & HOLLENDER, F. 2018. Radiation Patterns Control the Near-Source Ground-Motion Saturation Effect. *Bulletin of the Seismological Society of America*.

FACCIOLI, E., PAOLUCCI, R. & VANINI, M. 2015. Evaluation of probabilistic site-specific seismic-hazard methods and associated uncertainties, with applications in the Po Plain, northern Italy. *Bulletin of the Seismological Society of America,* 105**,** 2787-2807.

GARCIA, D., WALD, D. J. & HEARNE, M. 2012. A global earthquake discrimination scheme to optimize ground-motion prediction equation selection. *Bulletin of the Seismological Society of America,* 102**,** 185-203.

GIARDINI, D., DANCIU, L., ERDIK, M., ŞEŞETYAN, K., TÜMSA, M. B. D., AKKAR, S., GÜLEN, L. & ZARE, M. 2018. Seismic hazard map of the Middle East. *Bulletin of Earthquake Engineering,* 16**,** 3567-3570.

GORINI, A., NICOLETTI, M., MARSAN, P., BIANCONI, R., DE NARDIS, R., FILIPPI, L., MARCUCCI, S., PALMA, F. & ZAMBONELLI, E. 2010. The Italian strong motion network. *Bulletin of Earthquake Engineering,* 8**,** 1075-1090.

GRAD, M., TIIRA, T. & GROUP, E. W. 2009. The Moho depth map of the European Plate. *Geophysical Journal International,* 176**,** 279-292.

GRÜNTHAL, G., STROMEYER, D., BOSSE, C., COTTON, F. & BINDI, D. 2018. The probabilistic seismic hazard assessment of Germany—version 2016, considering the range of epistemic uncertainties and aleatory variability. *Bulletin of Earthquake Engineering,* 16**,** 4339-4395.

GRÜNTHAL, G. & WAHLSTRÖM, R. 2012. The European-Mediterranean earthquake catalogue (EMEC) for the last millennium. *Journal of seismology,* 16**,** 535-570.

HOLMGREN, J. M. & ATKINSON, G. M. 2018. Effect of Uncertainty in Source Parameters on Ground-Motion Variability for Potentially Induced Earthquakes in the Central United States. *Seismological Research Letters,* 89**,** 702-711.

JACOBY, W. G. 2000. Loess:: a nonparametric, graphical tool for depicting relationships between variables. *Electoral Studies,* 19**,** 577-613.

KALE, Ö., AKKAR, S., ANSARI, A. & HAMZEHLOO, H. 2015. A ground-motion predictive model for Iran and Turkey for horizontal PGA, PGV, and 5% damped response spectrum: Investigation of possible regional effects. *Bulletin of the Seismological Society of America,* 105**,** 963-980.

KOLLER, M. 2016. robustlmm: An R package for robust estimation of linear mixed-effects models. *Journal of statistical software,* 75**,** 1-24.

KOTHA, S. R., BINDI, D. & COTTON, F. 2016. Partially non-ergodic region specific GMPE for Europe and Middle-East. *Bulletin of Earthquake Engineering,* 14**,** 1245-1263.

KOTHA, S. R., BINDI, D. & COTTON, F. 2017. From ergodic to region- and site-specific probabilistic seismic hazard assessment: Method development and application at European and Middle Eastern sites. *Earthquake spectra,* 33**,** 1433-1453.

KOTHA, S. R., COTTON, F. & BINDI, D. 2018. A new approach to site classification: Mixed-effects Ground Motion Prediction Equation with spectral clustering of site amplification functions. *Soil Dynamics and Earthquake Engineering*.

KOTHA, S. R., COTTON, F. & BINDI, D. 2019a. Empirical Models of shear-Wave Radiation pattern Derived from Large Datasets of Ground-shaking observations. *Scientific reports,* 9.

KOTHA, S. R., WEATHERILL, G. & COTTON, F. 2019b. Topographic slope and geology based site-response model for regional risk assessements. *5th International Conference on Earthquake Engineering and Seismology.* Ankara, Turkey.

KUEHN, N. M. & ABRAHAMSON, N. A. 2017. The Effect of Uncertainty in Predictor Variables on the Estimation of Ground-Motion Prediction Equations. *Bulletin of the Seismological Society of America,* 108**,** 358-370.

KUEHN, N. M., ABRAHAMSON, N. A. & WALLING, M. A. 2019. Incorporating Nonergodic Path Effects into the NGA-West2 Ground-Motion Prediction Equations. *Bulletin of the Seismological Society of America,* 109**,** 575-585.

KUEHN, N. M. & SCHERBAUM, F. 2016. A partially non-ergodic ground-motion prediction equation for Europe and the Middle East. *Bulletin of Earthquake Engineering,* 14**,** 2629-2642.

LANDWEHR, N., KUEHN, N. M., SCHEFFER, T. & ABRAHAMSON, N. 2016. A Nonergodic Ground-Motion Model for California with Spatially Varying Coefficients. *Bulletin of the Seismological Society of America,* 106**,** 2574-2583.

LANZANO, G., LUZI, L., PACOR, F., FELICETTA, C., PUGLIA, R., SGOBBA, S. & D'AMICO, M. 2019. A Revised Ground-Motion Prediction Model for Shallow Crustal Earthquakes in Italy. *Bulletin of the Seismological Society of America,* 109**,** 525-540.

LANZANO, G., SGOBBA, S., LUZI, L., PUGLIA, R., PACOR, F., FELICETTA, C., D'AMICO, M., COTTON, F. & BINDI, D. 2018. The pan-European engineering strong motion (ESM) flatfile: compilation criteria and data statistics. *Bulletin of Earthquake Engineering***,** 1-22.

LU, Y., STEHLY, L., PAUL, A. & GROUP, A. W. 2018. High-resolution surface wave tomography of the European crust and uppermost mantle from ambient seismic noise. *Geophysical Journal International,* 214**,** 1136-1150.

MANIGHETTI, I., CAMPILLO, M., BOULEY, S. & COTTON, F. 2007. Earthquake scaling, fault segmentation, and structural maturity. *Earth and Planetary Science Letters,* 253**,** 429-438.

MAYOR, J., TRAVERSA, P., CALVET, M. & MARGERIN, L. 2018. Tomography of crustal seismic attenuation in Metropolitan France: implications for seismicity analysis. *Bulletin of Earthquake Engineering,* 16**,** 2195-2210.

MITCHELL, B. J., CONG, L. & EKSTRÖM, G. 2008. A continent-wide map of 1-Hz Lg coda Q variation across Eurasia and its relation to lithospheric evolution. *Journal of Geophysical Research: Solid Earth,* 113.

MORI, J. & HELMBERGER, D. 1996. Large-amplitude Moho reflections (SmS) from Landers aftershocks, southern California. *Bulletin of the Seismological Society of America,* 86**,** 1845-1852.

PACOR, F., FELICETTA, C., LANZANO, G., SGOBBA, S., PUGLIA, R., D'AMICO, M., RUSSO, E., BALTZOPOULOS, G. & IERVOLINO, I. 2018. NESS1: A worldwide collection of strong-motion data to investigate near-source effects. *Seismological Research Letters,* 89**,** 2299-2313.

PIÑA-VALDÉS, J., SOCQUET, A., COTTON, F. & SPECHT, S. 2018. Spatiotemporal Variations of Ground Motion in Northern Chile before and after the 2014 M w 8.1 Iquique Megathrust Event. *Bulletin of the Seismological Society of America,* 108**,** 801-814.

RADIGUET, M., COTTON, F., MANIGHETTI, I., CAMPILLO, M. & DOUGLAS, J. 2009. Dependency of near-field ground motions on the structural maturity of the ruptured faults. *Bulletin of the Seismological Society of America,* 99**,** 2572-2581.

RITSEMA, J., DEUSS, A. A., VAN HEIJST, H. & WOODHOUSE, J. 2011. S40RTS: a degree-40 shear-velocity model for the mantle from new Rayleigh wave dispersion, teleseismic traveltime and normal-mode splitting function measurements. *Geophysical Journal International,* 184**,** 1223-1236.

RODRIGUEZ-MAREK, A., COTTON, F., ABRAHAMSON, N. A., AKKAR, S., AL ATIK, L., EDWARDS, B., MONTALVA, G. A. & DAWOOD, H. M. 2013. A model for single-station standard deviation using data from various tectonic regions. *Bulletin of the seismological society of America,* 103**,** 3149-3163.

SAHAKIAN, V., BALTAY, A., HANKS, T., BUEHLER, J., VERNON, F., KILB, D. & ABRAHAMSON, N. 2018. Decomposing leftovers: Event, path, and site residuals for a small-magnitude Anza region GMPE. *Bulletin of the Seismological Society of America,* 108**,** 2478-2492.

SAHAKIAN, V., BALTAY, A., HANKS, T., BUEHLER, J., VERNON, F., KILB, D. & ABRAHAMSON, N. 2019. Ground-Motion Residuals, Path Effects, and Crustal Properties: A Pilot Study in Southern California. *Journal of Geophysical Research: Solid Earth*.

SCHMEDES, J. & ARCHULETA, R. J. 2008. Near-source ground motion along strike-slip faults: Insights into magnitude saturation of PGV and PGA. *Bulletin of the Seismological Society of America,* 98**,** 2278-2290.

SEDAGHATI, F. & PEZESHK, S. 2017. Partially Nonergodic Empirical Ground-Motion Models for Predicting Horizontal and Vertical PGV, PGA, and 5% Damped Linear Acceleration Response Spectra Using Data from the Iranian Plateau. *Bulletin of the Seismological Society of America,* 107**,** 934-948.

SOMERVILLE, P. & YOSHIMURA, J. 1990. The influence of critical Moho reflections on strong ground motions recorded in San Francisco and Oakland during the 1989 Loma Prieta earthquake. *Geophysical Research Letters,* 17**,** 1203-1206.

TAKEMURA, S., KOBAYASHI, M. & YOSHIMOTO, K. 2016. Prediction of maximum P-and S-wave amplitude distributions incorporating frequency-and distance-dependent characteristics of the observed apparent radiation patterns. *Earth, Planets and Space,* 68**,** 166.

THOMPSON, E., WALD, D. J. & WORDEN, C. 2014. A VS30 map for California with geologic and topographic constraints. *Bulletin of the Seismological Society of America,* 104**,** 2313-2321.

TRAVERSA, P., MAUFROY, E. H., F, PERRON, V., FOUNDOTOS, L., SHIBLE, H., BREMAUD, V., DROUET, S., DAUCHY, C., HERVÉ, F., GUÉGUEN, P., LANGLAIS, M., WOLYNIEC, D., PÉQUEGNAT, C. & DOUSTE-BACQUE, I. in-preparation. FAS for the RESIF (French) dataset.

VENABLES, W. & RIPLEY, B. 2002. Modern applied statistics (Fourth S., editor) New York. Springer.

VILANOVA, S. P., NARCISO, J., CARVALHO, J. P., LOPES, I., QUINTA-FERREIRA, M., PINTO, C. C., MOURA, R., BORGES, J. & NEMSER, E. S. 2018. Developing a Geologically Based VS30 Site-Condition Model for Portugal: Methodology and Assessment of the Performance of ProxiesDeveloping a Geologically Based VS30 Site-Condition Model for Portugal. *Bulletin of the Seismological Society of America,* 108**,** 322-337.

VILLANI, M. & ABRAHAMSON, N. A. 2015. Repeatable site and path effects on the ground-motion sigma based on empirical data from southern California and simulated waveforms from the CyberShake platform. *Bulletin of the Seismological Society of America*.

WALD, D. J. & ALLEN, T. I. 2007. Topographic slope as a proxy for seismic site conditions and amplification. *Bulletin of the Seismological Society of America,* 97**,** 1379-1395.

WEATHERILL, G., KOTHA, S. R. & COTTON, F. 2019. Re-thinking Site Amplification in Regional Seismic Risk Assessment. *Earthquake spectra*.

WEATHERILL, G., PAGANI, M. & GARCIA, J. 2016. Exploring earthquake databases for the creation of magnitude-homogeneous catalogues: tools for application on a regional and global scale. *Geophysical Journal International,* 206**,** 1652-1676.

WOESSNER, J., LAURENTIU, D., GIARDINI, D., CROWLEY, H., COTTON, F., GRÜNTHAL, G., VALENSISE, G., ARVIDSSON, R., BASILI, R., DEMIRCIOGLU, M. B., HIEMER, S., MELETTI, C., MUSSON, R. W., ROVIDA, A. N., SESETYAN, K. & STUCCHI, M. 2015. The 2013 European Seismic Hazard Model: key components and results. *Bulletin of Earthquake Engineering,* 13**,** 3553-3596.